# A New Approach to Computational Analysis of Mixed-Boundary-Value Stress Problems of Curved Bodies

A Dissertation
by

**Abhishek Kumar Ghosh**

Student No.: 0411102032

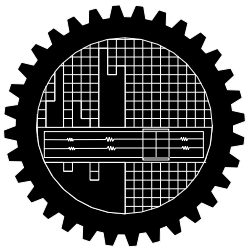

Department of Mechanical Engineering
Bangladesh University of Engineering and Technology
Dhaka- 1000, Bangladesh

March, 2014

# A New Approach to Computational Analysis of Mixed-Boundary-Value Stress Problems of Curved Bodies

A Dissertation
by

Abhishek Kumar Ghosh (Student No.: 0411102032)

Under the Supervision of

Dr. Shaikh Reaz Ahmed

Thesis submitted to the Department of Mechanical Engineering in
Partial Fulfilment of the Requirements for the Degree of

MASTER OF SCIENCE

in

Mechanical Engineering

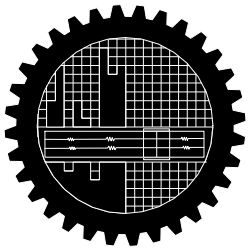

Department of Mechanical Engineering
Bangladesh University of Engineering and Technology
Dhaka- 1000, Bangladesh

March, 2014

# RECOMMENDATIONS OF THE BOARD OF EXAMINERS

The thesis titled, *A New Approach to Computational Analysis of Mixed-Boundary-Value Stress Problems of Curved Bodies*, submitted by Abhishek Kumar Ghosh, Roll no.: 0411102032, session: April, 20011 has been accepted as satisfactory in partial fulfilment of the requirement for the degree of Master of Science in Mechanical Engineering on March 22, 2014.

## BOARD OF EXAMINERS

| | |
|---|---|
| Dr. Shaikh Reaz Ahmed (Supervisor)<br>Professor<br>Department of Mechanical Engineering, BUET<br>Dhaka, Bangladesh | Chairman |
| Dr. Md. Zahurul Haq<br>Professor and Head<br>Department of Mechanical Engineering, BUET<br>Dhaka, Bangladesh | Member<br>Ex-officio |
| Dr. Md. Mahbubur Razzaque<br>Professor<br>Department of Mechanical Engineering, BUET<br>Dhaka, Bangladesh | Member |
| Dr. Md. Abdus Salam Akanda<br>Professor<br>Department of Mechanical Engineering, BUET<br>Dhaka, Bangladesh | Member |
| Dr. Khan Mahmud Amanat<br>Professor<br>Department of Civil Engineering, BUET<br>Dhaka, Bangladesh | External |

# DECLARATION

This thesis work does not contain any material extracted from elsewhere or from a work published by anybody else. The work of this thesis has not been published elsewhere by the author for any degree or any other University or Institute of learning.

_____

ABHISHEK KUMAR GHOSH
Roll No. 0411102032
Session: April 2011

# DEDICATION

To my parents

# ACKNOWLEDGEMENT

I would like to express my deepest gratitude to my supervisor Dr. Shaikh Reaz Ahmed, Professor, Department of Mechanical Engineering, Bangladesh University of Engineering and Technology, Dhaka for his support, guidance, inspiration, constructive suggestions and close supervision throughout the entire period of my graduate study.

The author acknowledges his gratefulness to Mechanical Engineering Department for providing required facilities. I would like to take the opportunity to thank all the members of examination committee for their constructive comments and criticism.

Finally, I want to express my deepest gratitude to my parents for their unparallel love, dedication, and encouragement throughout my whole life. Without their effort none of this would have been possible.

# CONTENTS

# LIST OF TABLES

# LIST OF FIGURES

# ABSTRACT

This research addresses a new method of analysis for the curved structural members under various types of loadings and supporting conditions at the boundary surfaces. In this work, theory of elasticity, a new potential function, constitutive relations for coordinate transformations and finite-difference computational algorithm are integrated to develop a new computational method for stress analysis of curved structural elements which include curved beams, deep arches, finite rings etc. Specific contributions are follows:

A new elasticity formulation is developed for stress analysis of mixed boundary-value stress problems of curved bodies. A new scheme of reduction of unknowns is used to develop the single scalar function formulation. More specifically, the scheme reduces the problem to finding a single field variable governed by a single partial differential equation of equilibrium. In the present formulation, a potential function is treated as the field variable which is defined in terms of radial and circumferential components of displacement, and the resulting formulation is called Displacement Potential Field Formulation. The formulation is superior to the standard stress function formulation in the sense that it is capable of satisfying all modes of physical conditions at the bounding surfaces appropriately, whether they are specified in terms of loadings or restraints or any combination of them.

A finite-difference computational algorithm is developed for obtaining numerical solutions of the elastic field of curved structural bodies in terms of the displacement potential. The displacement potential computation method finds a single unknown at each nodal point, whereas the existing methods find at least two variables at each node of the plane computational domain and hence a tremendous saving in computational effort is achieved through the proposed approach. The application of the method is demonstrated through the numerical solutions of a number of structural problems with curved boundaries. The soundness and accuracy of the single variable computational scheme is verified through the comparison of results with those obtained by conventional computational and analytical approaches where available.

# NOMENCLATURE

| | |
|---|---|
| $x, y, z$ | rectangular coordinates |
| $r, \theta, z$ | cylindrical coordinates |
| $E$ | elasticity modulus of the material |
| $v$ | Poisson's ratio |
| $u_r, u_\theta, u_z$ | normal components of displacement along $r$, $\theta$ and $z$-directions respectively |
| $\varepsilon_r, \varepsilon_\theta, \varepsilon_z$ | normal components of strain along $r$, $\theta$ and $z$-directions respectively |
| $\gamma_{r\theta}, \gamma_{\theta z}, \gamma_{zr}$ | shearing stress components of strain in $r\theta$, $\theta z$, $zr$ planes respectively |
| $\sigma_r, \sigma_\theta, \sigma_z$ | normal components of stress along $r$, $\theta$ and $z$-directions respectively |
| $\tau_{r\theta}, \tau_{\theta z}, \tau_{zr}$ | shearing stress components of stress in $r\theta$, $\theta z$, $zr$ planes respectively |
| $\psi$ | displacement potential function |
| $\phi$ | stress function |
| $u_n, u_t$ | normal and tangential components of displacement on the boundary |
| $\sigma_n, \sigma_t$ | normal and tangential components of stress on the boundary |
| $h, k$ | mesh lengths in $r$- and $\theta$-direction |
| $i, j$ | nodal coordinate system in $r$- and $\theta$-direction |
| $r_i, r_o$ | inner and outer radius |

Chapter 01

# INTRODUCTION

## 1.1 GENERAL

The subject matter of this thesis is the stress analysis of mixed-boundary-value elastic plane problems of curved geometries- a major branch in the field of applied mechanics. Applied mechanics has been developed as a branch of rational thoughts from very early times; it is the oldest of the physical sciences and its principles, formulated to describe mechanical behavior in nature, from the basis of engineering calculations for a vast range of devices and structures. In spite of the advanced stages to which Engineering Science has progressed, it is not yet capable of describing the behavior of real engineering systems in every aspect. In the design of a given product, one may need to refer to several branches of engineering science. The theory of elasticity developed into an important branch of mathematical physics which has found considerable applications in the solution of engineering problems.

The theory of elasticity deals with the systematic study of the stress, strain and displacement in an elastic body, under the influence of external forces. It differs with the field of 'strength of materials' in that the later is more elementary in theory with more emphasis on convenient formulas for practical applications. The elementary strength of material treats each problem separately – for example, a beam and a shaft are analyzed as separate problems. Although they are of practical importance, the formulas derived are applied under very restrictive conditions. The theory of elasticity deals with general equations which must be satisfied by an elastic body in equilibrium under any external force system. Simplifying assumptions are also used in elasticity, but with a better knowledge about the approximation involved.

The response of a solid body to external forces is influenced by the geometric configuration of the body as well as the mechanical properties of the material. Here the interest will be restricted to the elastic materials in which the deformation and stress disappears with the removal of external forces, provided that the external forces do not exceed a certain limit. In fact, almost all engineering materials possess to a certain extent the property of elasticity. It is assumed that the matter of an elastic body is homogenous and continuously distributed over

its volume so that the smallest element cut from the body posses the same specific physical properties as the body. It is also assumed that for the most part the body is isotropic, that's the elastic properties are the same in all directions.

Curved structural bodies like beams, bars, rings, disks, arches etc. have a numerous important applications in the field of mechanical, civil and aeronautical engineering. For example, curved beams are used as crane hooks, clampers, frames of presses, chains, links, rings etc. Many airplanes have fuselages of approximately circular cross section which are built around circular metal bulkhead rings connected by longitudinal metal stringers and covered with a thin sheet-metal skin. Circular rings are also used as load transducer and circular cylinders are used as pressure vessel for containing pressurized fluid. Arch construction is one of the oldest means of spanning rivers and forming the roofs of large buildings. They have been used to support bridge decks and roofs, aqueducts, gates etc. for centuries.

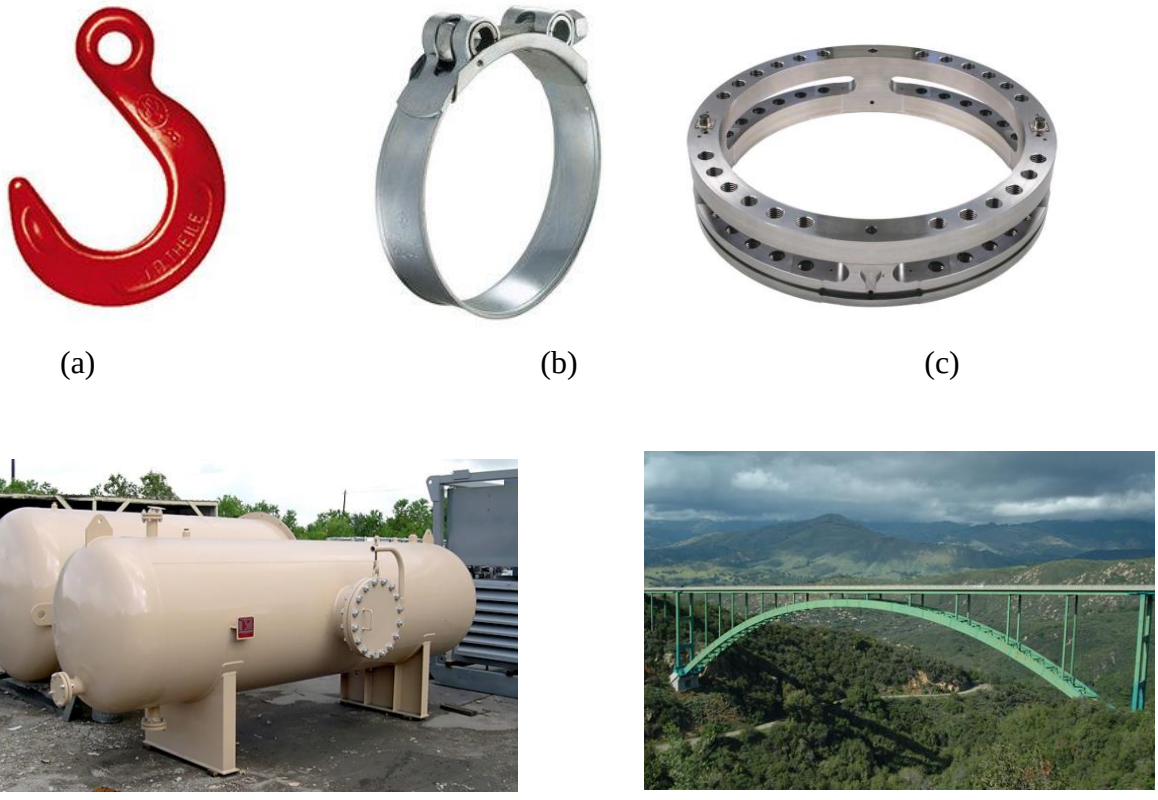

(a) (b) (c)

(d) (e)

Figure 1.1: Applications of curved structural bodies: (a) crane hook, (b) clamper, (c) load transducer, (d) pressure vessel and (e) arch.

In analyzing stresses in bodies like circular rings and disks, curved bars and beams/ arches, thick-walled cylindrical pressure vessel etc., it is advantageous to use a curvilinear mesh network for their discretization. The position of a point in the body is then defined by the distance of the point from the origin, angular position of the point with respect to some fixed axis and height of the point with respect to a fixed base plane. Analysis of stresses in a material body is basically a three-dimensional problem. However, in most practical cases, the problem can reasonably be approximated to either a two-dimensional or a one-dimensional one. One-dimensional problems of stress analysis are very straightforward and are included in undergraduate curricula. But the problems of two-dimensional stress analysis have a different story. In case of very simple structures like beam, column, circular disk, regular shaped plates and thin shells, having simple geometry and boundary conditions, analytical methods are used for their stress analysis. However, the application of analytical approaches is limited, because general closed form solution can only be obtained for very ideal cases.

Mixed-boundary-value problems are those in which the boundary conditions are specified as a mixture of boundary restraints and boundary loadings. The analytical results obtained for the practical problems of elasticity, usually with mixed boundary conditions, are invariably approximate as they include various idealizations. With the development of high speed computing machines, great attention has been paid to numerical methods in seeking the solution to a single, or a system of partial differential equations, which, even now, remain beyond the scope of analytical solution.

## 1.2 LITERATURE REVIEW

Stress-analysis of structural bodies is of great importance and has now become a classical subject in the field of engineering. But, somehow, this subject is still suffering from a lot of shortcomings and thus it is constantly coming up in the literature [1-4]. The theory of elasticity has found considerable application in the solution of modern engineering problems. The elementary formulas of strength of materials are often not accurate enough, and the use of the theory of elasticity in solving practical problems has rapidly become more common. Elementary methods of strength of materials were the primary tools of the practicing engineers for handling the problems of engineering structures. However, these methods are often found inadequate to furnish satisfactory information regarding local stresses near the

loads and near the supports of the structures. The elementary theory gives no means of investigating stresses in regions of sharp variation in cross section of beams or shafts.

New problems of machine design and theory of structures in the recent years have demanded greater accuracy of stress analysis than what was previously the case. Only in simple cases were rigorous mathematical solutions of elasticity problems available and the modern trend in the theory is toward the use of various approximate methods. In cases where even approximate methods could not be developed, solutions have been obtained by using experimental methods. Photoelastic methods, soap-film methods, application of strain gages, moiré fringes [5] are some of these experimental methods applied in the study of stress concentration at points of sharp variation of cross-sectional dimensions and at sharp fillets of reentrant corners. These experimental results have considerably influenced the modern design of machine parts and helped in many cases to improve the construction by eliminating weak spot from which crack may start.

Among the existing mathematical models for two-dimensional elastic problems, the stress function approach introduced by G. B. Airy and the displacement parameter approach [5] are noticeable. The Airy stress function is governed by a fourth order partial differential equation and the stress components are related to it through various second order derivatives. Solutions were initially sought through various polynomial expressions of stress function, but the success of this polynomial approach was very limited. Successful application of stress function formulation in conjunction with the finite-difference technique has been reported for the solution of plane elastic problems where the conditions on the boundary are prescribed in terms of stresses only [6-8]. Boundary restraints specified in terms of displacement components cannot be satisfactorily imposed on the stress function. The difficulties involved in trying to solve practical stress problems using the stress function approach are pointed out in our previous researches [9-10], and also by Durelli [3]. Again, the two displacement parameter approach involves finding two functions simultaneously from two second order partial differential equations. But the simultaneous evaluation of two functions, satisfying two differential equations is extremely difficult especially when the boundary conditions are specified as a mixture of restraints and stresses. As a result, serious attempts had hardly been made in the field of stress analysis using this formulation.

Prior to the widespread use of computer, the available methods for stress analysis of curved beams and bar were Strength of materials based methods and Timoshenko’s elasticity

formulation [5]. Two forms of strength of materials solutions are used to determine stress distributions in curved beams and they are introduced in Machine Design, Strength of Materials, and Elasticity textbooks. One is the 'Simplified Method' as seen in Chapter 13.2 of [11], Chapters 2.20 of [12, 13]. The second is identified as the 'Winkler's Theory' as seen in Chapter 5.12 of [14]. Winkler's theory mainly gives the analytical expression for the circumferential stress and the results from Winkler's formula, however, are not valid when the curved beams are thick, because this theory neglects the effects of transverse shear deformation. Winkler's theory is redeveloped in [15] using linear shape function for tangential strain. The normal force equilibrium condition at the cross-section of the curved beam in both of these strength of materials based theories, considers no normal force as if pure bending occurs. This equilibrium condition also defines the neutral axis location incorrectly when forcing occurs. The more refined Timoshenko's theory relaxes the normality assumption of the plane sections which are to remain plane and normal to the deformed centerline of the curved beam. By allowing a further rotation of the normal, the theory admits a nonzero shearing strain. Timoshenko's elasticity approach has served as the standard of comparison for attempted modifications of Winkler's theory [16]. However, Winkler's theory is applicable to cross-sections of any shape, whereas the traditional elasticity approach is only applicable to rectangular sections. The literature chronicles several unique methods of applying and attempts at improving Winkler's theory [17-21]. A general solution involving infinite series to the distribution of stresses in circular ring compressed by two forces acting along a diameter was given by Chianese and Erdlac [22]. Bagci [23] presented a unified strength of materials solution for stresses in curved beams and rings, which consider the curvature effect on both moment and force loadings. It yields more precision results than the conventional 'Simplified' and 'Winkler's' strength of materials solutions as shown in their paper. The elasticity solution for curved beams and rings with exponential and 'T' cross section was presented by Bagci [24], which is however identified to be an approximation because the state of stress is arbitrarily assumed to be plane (see Ref. [16]). A plane stress analysis based on stress function formulation [5] was presented by Tutuncu [25] for the stress and displacement distributions in polar orthotropic curved beams possessing narrow constant cross sections. Recently, Sloboda and Honarmandi [26] have developed an elasticity based method for the analysis of curved beam of non-rectangular cross section. This method has the similar characteristic of the stress function approach, that is, it accepts boundary conditions only in terms of boundary loadings (stresses).

Stress analysis of circular arches is a classical problem of applied mechanics. People are investigating different types of arches for decades as these are very important structural elements. Makowski and Gogate analyzed the stresses of three-pinned arch-ribbed domes in their paper [27].The Paper discusses the principles of the stress analysis of three-pinned ribbed domes consisting of any number of three-hinged semi-circular arches, interconnected together at the apex. General formulae of reaction components are developed, facilitating the determination of influence lines of these functions. Inter-laminar stress of laminated composite and sandwich circular arches subjected to thermal/mechanical loading is reported by Hiroyuki Matsunaga [28]. In his work, stresses and displacements in cross-ply laminated composite and sandwich circular arches subjected to thermal and mechanical loadings have been analyzed by a global higher-order arch theory which can take into account the effects of both transverse shear and normal stresses. By using the method of power series expansion of displacement components, a set of fundamental equilibrium equations of a one-dimensional higher-order theory for laminated composite circular arches is derived through the principle of virtual work. He has applied several sets of truncated approximate theories to solve the boundary value problems of simply supported laminated composite and sandwich circular arches. Elmalich and Rabinovitch have analyzed stresses in Monolithic Circular Arches Strengthened with Composite Materials [29]. They have presented an analytical approach for the elastic stress analysis of monolithic circular arches strengthened with externally bonded fiber-reinforced polymer (FRP) strips. In their work they have emphasized on the interfacial stresses between the existing structure and the supplemental reinforcement layers. Two analytical models have been presented: The first model formulates the governing equations in terms of the displacements in the arch and the FRP strip and the tangential distribution of the shear stresses in the adhesive layer as unknowns without involving any assumptions on the stress and displacement fields in the adhesive layer. The second model uses the functional form of the displacement field derived in the first model yielding a formulation in terms of displacement unknowns only. Free vibration and stability of laminated composite circular arches subjected to initial axial stress are reported to be analyzed by Hiroyuki Matsunaga [30] where natural frequencies and buckling stresses of laminated composite circular arches subjected to initial axial stress have been analyzed by taking into account the complete effects of transverse shear and normal stresses and rotatory inertia.

A circular ring is often used in engineering applications. There are many applications in the tunnels, subways, and down hole. Leon Beskin summarized formulas which are required for

the analysis of circular rings, under forces in the plane of the ring or out of the plane in his paper [31]. Usually, rings which are redundant structures are calculated by considering strain due to bending only. In this research it is shown that for the stress distribution in a circular ring under given load, the solution introducing strains due to shearing and axial loads is the same as the solution conventionally used. The plane elastic problem corresponding to a radial crack emanating from the internal boundary of a circular ring is reported by Bowie and Freese [32]. For this problem the stress intensity factors at the crack tip has been found by using the 'modified mapping collocation' technique. Accurate data has been found for varying crack depths over a representative range of wall ratios for fracture mechanics applications to pressurized hollow circular cylinders. Using a moiré, large-strain analysis method, a complete solution is of the fields of strain and stress for a circular ring subjected to diametral compression between two flat platens has been reported by Durelli et al [33]. The results were verified with the isochromatics obtained from a large-deformation photoelasticity analysis. The ring was made of a polyurethane rubber which exhibits a linear relationship between natural strain and a concept of "natural stress". Deflection of the circular ring under a concentrated force has been studied by Xiao Zeng Wang [34]. Adopting the method of numerical analysis and Castigliano's theory, the max deflection and the 4th equivalent stress of ring have been developed. The results of the research indicate that the deflection of ring is the linear function of the concentrated force which is in accord with the elasticity body assumptions, that is Hook's law. Since the theoretical solution of the deflection of ring is found to be almost the same as the numerical one of the ring, it is feasible that the numerical model of the ring is used to analyze the deflection of the eccentric ring.

Analytical methods of solution could not gain that much popularity in the field of stress analysis of structural components, mainly because of the inability of dealing with the mixed and variable nature of physical conditions as well as complex boundary shapes, which are, however, very common in case of actual structures. Stress analysis of structural problems is mainly handled by numerical methods. The major numerical methods in use are (a) the finite-difference method (FDM) and (b) the finite-element method (FEM). The FEM has received widespread applications in various aspects of structural analysis, especially for curved shaped structures, a few of which are cited in reference [34-36]. However, the uncertainties associated with the accurate and reliable prediction of surface stresses by the conventional computational approaches have been pointed out by several researches [37-38]. The errors arising in the curved finite elements which under goes both flexure and membrane

deformations were pointed out by Gangan [39]. It was there reported that an error of special nature would involve if the membrane strain fields are not consistently interpolated with terms from the two independent field functions, and the associated physical phenomenon was termed as membrane locking.

The finite-difference method, on the other hand, is an ideal numerical technique for obtaining direct numerical solutions of differential equations. Introducing a new boundary modeling approach for finite difference (FD) applications of the displacement formulation of solid mechanics, Dow *et al*. [4] reported that the accuracy of finite difference method (FDM) in reproducing the state of stresses along the bounding surfaces was much higher than the corresponding accuracy of finite element (FE) analysis. Comparing the performances of available modeling approaches for the analysis of composite beams with partial shear interactions, the FDM was determined to be an adequate numerical tool for describing the composite behavior of beams, and the corresponding FD solutions were shown to be more accurate when compared with the usual eight degree-of-freedom finite element method (FEM) solutions [40]. Recent research and developments have generated renewed interests in using FDM for stress analysis of both two- and three-dimensional structural elements of isotropic as well as composite materials [41-42]. Analyzing the results of orthotropic composite panels, the superiority of the potential-function based FDM has been verified over conventional computational method in predicting stresses, especially at the regions of transition of boundary conditions [30]. FDM was also found successful in modeling irregular boundary shapes through the displacement-potential based interpolation scheme applied in a rectangular mesh network [46-47].

## 1.3 OBJECTIVES

The prime objective of this research work is to develop a new elasticity formulation for the analysis of mixed-boundary-value plane problems in cylindrical coordinate system and to develop an efficient computational scheme for the numerical solution of the elastic field using finite difference technique. The present study is an attempt to extend the capability of the displacement potential approach in order to address stress analysis of curved bodies with mixed-boundary conditions. The specific objectives of the present research work can be summarized as follows:

1. Development of a new mathematical formulation suitable for mixed boundary-value elastic problems of curved bodies.

2. Development of a scheme for the management of all possible modes of boundary conditions associated with the practical stress problems in curvilinear coordinate system.

3. Development of a finite-difference computational scheme based on the new formulation to obtain the corresponding numerical solution of the elastic field.

4. Application of the new computational method to a number of practical problems of structural mechanics with curved geometries.

5. Validation of the computational approach by comparing the results with available analytical solution and finite element solution.

The new formulation as well as the computational method is expected to be a valuable addition to the present literature and will provide a reliable design guide for the curved structural elements.

## 1.4. OUTLINE OF METHODOLOGY

In the proposed research work, a new mathematical formulation is developed for the stress analysis of plane elastic problems with curved geometries. A new scheme of reduction of unknowns is used to develop the formulation. More specifically, the scheme reduces the problem to finding a single potential function, defined in terms of two displacement components of plane elasticity in polar coordinate system, whereas the existing finite-element and finite-difference methods find at least two variables at each nodal point of the computational domain, and hence a tremendous saving in computational effort is achieved through the proposed formulation. Finite-difference technique is used for the discretization of the governing fourth-order partial differential equation as well as the second and third order partial differential equations associated with the boundary conditions. Ultimately the problem is solved by finding the solution for the single discretized variable from a system of linear algebraic equations resulting from the discretization of the domain in terms of a curvilinear mesh-network.

## 1.5 THE REASON FOR NUMERICAL SOLUTION

In this thesis, a computational scheme for general two-dimensional stress problems curved bodies is developed and numerical solution for several practical problems is obtained through a computer code developed in MATLAB.

With the development of high speed computing machine in the recent years, the practicing engineers are now capable of facing new problems of machine design and theory of structures demanding greater accuracy of stress analysis and complete design in a very short time. However, the reason for resorting to the numerical solution for the stresses in a plane region is that it is not possible to solve the problem analytically under all circumstances created by the boundary conditions and shapes. It is extremely difficult to find an analytical solution for this problem when the boundary conditions are mixed, no matter in what manner they are mixed. Again the geometry and the variation of material property also create difficulty in finding analytical solution and leave us no other way than to go for numerical solution.

## 1.6 SCOPE OF APPLICATION

The mathematical formulation developed in this thesis can be used for plane problems of elasticity in cylindrical coordinate system by applying a numerical or analytical technique. The numerical scheme developed in this thesis can be applied for the problems subjected to all the possible modes of boundary conditions associated with the practical stress problems. Stress analysis of curved beams and bars, circular arches, finite rings, stiffened beam/rings are considered as examples of application of the present computational method.

Therefore it may be concluded that a large number of problems of practical importance may be considered to be within the scope of the present method.

Chapter 02

# MATHEMATICAL FORMULATION

## 2.1 GENERAL RELATIONS

The elastic analysis of a body deals with the determination of stress components and displacement components at various points within the body due to given body forces and given conditions at the boundary surfaces of the body. To achieve this objective, a number of functions of space variables are defined in such a manner that the knowledge of these functions is sufficient to predict the state of the stress at any point in the body. Of course, these functions must satisfy the conditions of equilibrium and the conditions of the compatibility of stresses throughout the body.

If an infinitesimal volume element is cut off from a homogeneous isotropic elastic body, the result would be six forces acting on the six different faces of the element. The forces acting on a face may be resolved into two components- one perpendicular to the plane of the face and the other parallel to the face. The stress component acting perpendicular to the plane of the face is called the normal stress and usually denoted by "$\sigma$" with a subscript to indicate its direction of action. According to the general convention, the normal stresses are taken positive when producing tension and negative when producing compression. In the same way, the two stress components acting parallel to the face are known as shearing stresses and indicated by "$\tau$" with double subscript- the first indicating the direction of the normal to the face and the second indicating the direction of the component of the stress. On any side, the direction of the positive shearing stress coincides with the positive direction of the axis if the outward normal on this side has the positive direction of the corresponding axis. If the outward normal has a direction opposite to positive axis, the positive shearing stress will also have the opposite direction of the corresponding axis.

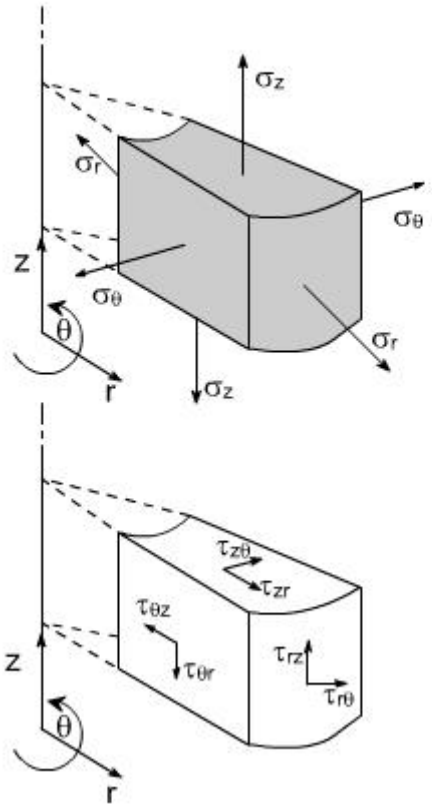


**Figure 2.1:** Conventions of stress components of the elementary volume in cylindrical coordinate system.

Though, the volume element has six different faces, basically, it has three mutually perpendicular faces and the rest of the faces are parallel to these mutually perpendicular faces respectively as shown in Fig. 2.1. Thus, considering a volume element with edges parallel to the three axes of a cylindrical coordinate system, the state of stress of six sides of the element are described by three symbols $\sigma_r$, $\sigma_\theta$, $\sigma_z$ for normal stress and six symbols $\tau_{r\theta}$, $\tau_{\theta r}$, $\tau_{zr}$, $\tau_{rz}$, $\tau_{\theta z}$, $\tau_{z\theta}$ for shearing stress. A consideration of the equilibrium of the volume element shows that, for two perpendicular sides of the element, the components of shearing stress perpendicular to the line of intersection of these sides are equal. Mathematically stated, from consideration of equilibrium of moments about three mutually perpendicular axes, it can be shown that

$$\tau_{r\theta} = \tau_{\theta r}$$
$$\tau_{rz} = \tau_{zr} \quad \text{and}$$
$$\tau_{\theta z} = \tau_{z\theta}$$

Thus the nine components of stress are reduced to six. These six quantities $\sigma_r$, $\sigma_\theta$, $\sigma_z$, $\tau_{r\theta}$, $\tau_{\theta z}$, $\tau_{zr}$ are therefore sufficient to describe the stresses acting on the coordinate planes through a point and these will be called the components of stresses at the point.

When a body is subjected to external forces, not only are internal stresses generated, but also the body itself is deformed. These deformations of the body can be uniquely specified by assigning three elongations in three perpendicular directions and three shear strains related to the same direction. These directions are taken as the directions of coordinate axes and the symbol "$\varepsilon$" is used to denote the normal strain components with the same subscripts to this symbol as for the normal stress components. Shear strain components are denoted by the symbol "$\gamma$" with the same double subscript used for shear stress. If the components of displacement of a particle in the body are specified by $u_r$, $u_\theta$ and $u_z$ parallel to the coordinate axes $r$, $\theta$ and $z$ respectively, then the relations between the components of strain and the components of displacement are given by

$$\varepsilon_r = \frac{\partial u_r}{\partial r} \qquad 2.1(a)$$

$$\varepsilon_\theta = \frac{u_r}{r} + \frac{\partial u_\theta}{r\partial\theta} \qquad 2.1(b)$$

$$\varepsilon_z = \frac{\partial u_z}{\partial z} \qquad 2.1(c)$$

$$\gamma_{r\theta} = \frac{\partial u_r}{r\partial\theta} + \frac{\partial u_\theta}{\partial r} - \frac{u_\theta}{r} \qquad 2.1(d)$$

$$\gamma_{\theta z} = \frac{\partial u_\theta}{\partial z} + \frac{\partial u_z}{r\partial\theta} \qquad 2.1(e)$$

$$\gamma_{zr} = \frac{\partial u_r}{\partial z} + \frac{\partial u_z}{\partial r} \qquad 2.1(f)$$

By the application of Hooke's, that is the linear relation between the stress and strain components and the principle of superposition, which are both based on experimental

observation, the relation between the components of stress and components of strain is given by

$$\varepsilon_r = \frac{1}{E}[\sigma_r - \nu(\sigma_\theta + \sigma_z)] \quad 2.2(a)$$

$$\varepsilon_\theta = \frac{1}{E}[\sigma_\theta - \nu(\sigma_r + \sigma_z)] \quad 2.2(b)$$

$$\varepsilon_z = \frac{1}{E}[\sigma_z - \nu(\sigma_r + \sigma_\theta)] \quad 2.2(c)$$

$$\gamma_{r\theta} = \frac{1}{G}\tau_{r\theta} = \frac{2(1+\nu)}{E}\tau_{r\theta} \quad 2.2(d)$$

$$\gamma_{\theta z} = \frac{1}{G}\tau_{\theta z} = \frac{2(1+\nu)}{E}\tau_{\theta z} \quad 2.2(e)$$

$$\gamma_{zr} = \frac{1}{G}\tau_{zr} = \frac{2(1+\nu)}{E}\tau_{zr} \quad 2.2(f)$$

Now considering the static equilibrium of the volume element and assuming that there are no body forces, the following differential equations of equilibrium can be derived [5]:

$$\frac{\partial \sigma_r}{\partial r} + \frac{1}{r}\frac{\partial \tau_{r\theta}}{\partial \theta} + \frac{\partial \tau_{rz}}{\partial z} + \frac{\sigma_r - \sigma_\theta}{r} = 0 \quad 2.3(a)$$

$$\frac{\partial \tau_{rz}}{\partial r} + \frac{1}{r}\frac{\partial \tau_{\theta z}}{\partial \theta} + \frac{\partial \sigma_z}{\partial z} + \frac{1}{r}\tau_{rz} = 0 \quad 2.3(b)$$

$$\frac{\partial \tau_{r\theta}}{\partial r} + \frac{1}{r}\frac{\partial \sigma_\theta}{\partial \theta} + \frac{\partial \tau_{\theta z}}{\partial z} + \frac{2}{r}\tau_{r\theta} = 0 \quad 2.3(c)$$

## 2.2 ANALYSIS OF PLANE PROBLEMS OF ELASTICITY

Most of the practical problems of stress analysis can reasonably be resolved into two-dimensional ones following one of the two simplifying assumptions, namely, plane stress and plane strain conditions. With reference to the cylindrical coordinate system, in absence of body forces, the three governing equations for general isotropic materials, in terms of stress variables $\sigma_r$, $\sigma_\theta$ and $\tau_{r\theta}$ for plane stress and plane strain problems are as follows [5]:

$$\frac{\partial \sigma_r}{\partial r} + \frac{1}{r}\frac{\partial \tau_{r\theta}}{\partial \theta} + \frac{\sigma_r - \sigma_\theta}{r} = 0 \quad (2.4a)$$

$$\frac{1}{r}\frac{\partial \sigma_\theta}{\partial \theta}+\frac{\partial \tau_{r\theta}}{\partial r}+\frac{2}{r}\tau_{r\theta}=0 \tag{2.4b}$$

$$\left(\frac{\partial^2}{\partial r^2}+\frac{1}{r}\frac{\partial}{\partial r}+\frac{1}{r^2}\frac{\partial^2}{\partial \theta^2}\right)\left(\sigma_r+\sigma_\theta\right)=0 \tag{2.4c}$$

The strain components of plane elasticity are defined in terms of displacement components by the following relations:

$$\varepsilon_r=\frac{\partial u_r}{\partial r} \tag{2.5a}$$

$$\varepsilon_\theta=\frac{u_r}{r}+\frac{\partial u_\theta}{r\partial \theta} \tag{2.5b}$$

$$\gamma_{r\theta}=\frac{\partial u_r}{r\partial \theta}+\frac{\partial u_\theta}{\partial r}-\frac{u_\theta}{r} \tag{2.5c}$$

Now according to the Hooke's law, the relationship between stress and strain components, under plane stress condition, can be expressed as follows:

$$\varepsilon_r=\frac{1}{E}[\sigma_r-v\sigma_\theta] \tag{2.6a}$$

$$\varepsilon_\theta=\frac{1}{E}[\sigma_\theta-v\sigma_r] \tag{2.6b}$$

$$\gamma_{r\theta}=\frac{1}{G}\tau_{r\theta}=\frac{2(1+v)}{E}\tau_{r\theta} \tag{2.6c}$$

Now by replacing the strain components in Eq. (2.6) by displacement components in Eq. (2.5), we can find the relationship between stress components and displacement components for plane stress problems, as follows:

$$\sigma_r=\frac{E}{1-v^2}\left(\frac{\partial u_r}{\partial r}+\frac{v}{r}\frac{\partial u_\theta}{\partial \theta}+\frac{v}{r}u_r\right) \tag{2.7a}$$

$$\sigma_\theta=\frac{E}{1-v^2}\left(v\frac{\partial u_r}{\partial r}+\frac{1}{r}\frac{\partial u_\theta}{\partial \theta}+\frac{1}{r}u_r\right) \tag{2.7b}$$

$$\tau_{r\theta} = \frac{E}{2(1+\nu)}\left(\frac{1}{r}\frac{\partial u_r}{\partial \theta} + \frac{\partial u_\theta}{\partial r} - \frac{u_\theta}{r}\right) \tag{2.7c}$$

The similar relations under plane strain conditions can be obtained by replacing $E$ and $\nu$ by $E_{\text{strain}}$ and $\nu_{\text{strain}}$ respectively which are defined by the following relations:

$$\mathrm{E}_{strain} = \frac{E}{1-\nu^2} \tag{2.8a}$$

$$\nu_{strain} = \frac{\nu}{1-\nu} \tag{2.8b}$$

If we replace the stress components in Eq. (2.4) by displacement components $u_r$ ($r$, $\theta$) and $u_\theta$ ($r$, $\theta$), which are related to stress components through Eqs. (2.7), then Eq. (2.4c) is redundant and Eqs. (2.4a) and (2.4b) transform respectively to,

$$\begin{aligned}
&\frac{\partial}{\partial r}\left\{\frac{E}{1-\nu^2}\left(\frac{\partial u_r}{\partial r} + \frac{\nu}{r}\frac{\partial u_\theta}{\partial \theta} + \frac{\nu}{r}u_r\right)\right\} + \frac{1}{r}\frac{\partial}{\partial \theta}\left\{\frac{E}{2(1+\nu)}\left(\frac{1}{r}\frac{\partial u_r}{\partial \theta} + \frac{\partial u_\theta}{\partial r} - \frac{u_\theta}{r}\right)\right\} \\
&+\frac{1}{r}\left\{\frac{E}{1-\nu^2}\left(\frac{\partial u_r}{\partial r} + \frac{\nu}{r}\frac{\partial u_\theta}{\partial \theta} + \frac{\nu}{r}u_r - \nu\frac{\partial u_r}{\partial r} - \frac{1}{r}\frac{\partial u_\theta}{\partial \theta} - \frac{u_r}{r}\right)\right\} = 0 \\
&\Rightarrow \frac{\partial^2 u_r}{\partial r^2} + \frac{(1+\nu)}{2r}\frac{\partial^2 u_\theta}{\partial r \partial \theta} + \frac{(1-\nu)}{2r^2}\frac{\partial^2 u_r}{\partial \theta^2} + \frac{1}{r}\frac{\partial u_r}{\partial r} - \frac{(3-\nu)}{2r^2}\frac{\partial u_\theta}{\partial \theta} - \frac{u_r}{r^2} = 0
\end{aligned} \tag{2.9a}$$

$$\begin{aligned}
&\frac{1}{r}\frac{\partial}{\partial \theta}\left\{\frac{E}{1-\nu^2}\left(\nu\frac{\partial u_r}{\partial r} + \frac{1}{r}\frac{\partial u_\theta}{\partial \theta} + \frac{u_r}{r}\right)\right\} + \frac{\partial}{\partial r}\left\{\frac{E}{2(1+\nu)}\left(\frac{1}{r}\frac{\partial u_r}{\partial \theta} + \frac{\partial u_\theta}{\partial r} - \frac{u_\theta}{r}\right)\right\} \\
&+\frac{2}{r}\left\{\frac{E}{2(1+\nu)}\left(\frac{1}{r}\frac{\partial u_r}{\partial \theta} + \frac{\partial u_\theta}{\partial r} - \frac{u_\theta}{r}\right)\right\} = 0 \\
&\Rightarrow \frac{(1-\nu)}{2}\frac{\partial^2 u_\theta}{\partial r^2} + \frac{(1+\nu)}{2r}\frac{\partial^2 u_r}{\partial r \partial \theta} + \frac{1}{r^2}\frac{\partial^2 u_\theta}{\partial \theta^2} + \frac{(1-\nu)}{2r}\frac{\partial u_\theta}{\partial r} + \frac{(3-\nu)}{2r^2}\frac{\partial u_r}{\partial \theta} - \frac{(1-\nu)}{2r^2}u_\theta = 0
\end{aligned} \tag{2.9b}$$

Eq. (2.9) gives the two equilibrium equations in terms of displacement components for the plane stress problems in polar coordinate system. Reliable and accurate solution of the displacement components satisfying the two simultaneous elliptic partial differential equations with variable coefficients, especially with various mixed-modes of boundary conditions is not an easy task. A new mathematical model is thus introduced by which the

problem can be solved in terms of a single variable with all possible modes of boundary conditions.

## 2.3 STRESS FUNCTION FORMULATION

To solve the two dimensional governing equations (Eq. 2.4) G. B. Airy introduced a new function $\phi(r, \theta)$ which is known as stress function [5]. In this stress function formulation, the stress components are defined in terms of $\phi(r, \theta)$ as follows:

$$\sigma_r = \frac{1}{r}\frac{\partial \phi}{\partial r} + \frac{1}{r^2}\frac{\partial^2 \phi}{\partial \theta^2} \tag{2.10a}$$

$$\sigma_\theta = \frac{\partial^2 \phi}{\partial r^2} \tag{2.10b}$$

$$\begin{aligned} \tau_{r\theta} &= \frac{1}{r^2}\frac{\partial \phi}{\partial \theta} - \frac{1}{r}\frac{\partial^2 \phi}{\partial r \partial \theta} \\ &= -\frac{\partial}{\partial r}\left(\frac{1}{r}\frac{\partial \phi}{\partial \theta}\right) \end{aligned} \tag{2.10c}$$

This definition of stress components satisfies the two equilibrium equations [Eqs. 2.1(a) and 2.4(b)] automatically. The only equation remains to be satisfied is the compatibility equation [Eq. 2.1(c)]. Now by replacing the expressions of stress components in the Eq. 2.4(c) by the expressions in Eqs. 2.10, the compatibility equation in terms of stress function $\phi(r, \theta)$ is obtained as follows:

$$\left(\frac{\partial^2}{\partial r^2} + \frac{1}{r}\frac{\partial}{\partial r} + \frac{1}{r^2}\frac{\partial^2}{\partial \theta^2}\right)\left(\frac{\partial^2 \phi}{\partial r^2} + \frac{1}{r}\frac{\partial \phi}{\partial r} + \frac{1}{r^2}\frac{\partial^2 \phi}{\partial \theta^2}\right) = 0 \tag{2.11}$$

Thus, the solution of a two-dimensional problem reduces to finding the solution of Ep. (2.11) that satisfies the boundary conditions of the problem. But this formulation can only satisfy boundary conditions expressed in terms of boundary loadings not in terms of boundary restraints as the displacement components cannot be expressed in terms of stress function.

Thus, this stress function formulation fails to handle mixed-boundary-value problems of elasticity.

## 2.4 REDUCTION OF UNKNOWNS

In this section, the plane problem of elasticity in polar coordinate system in terms of two displacement functions is reduced to the determination of a single function by introducing a new scheme of reduction of unknowns. In order to attain that, the displacement components are first expressed in terms of a potential function $\psi$ of space variables as follows:

$$u_r = \alpha_1 \frac{\partial^2 \psi}{\partial r^2} + \alpha_2 \frac{1}{r} \frac{\partial^2 \psi}{\partial r \partial \theta} + \alpha_3 \frac{1}{r^2} \frac{\partial^2 \psi}{\partial \theta^2} + \alpha_4 \frac{1}{r} \frac{\partial \psi}{\partial r} + \alpha_5 \frac{1}{r^2} \frac{\partial \psi}{\partial \theta} + \alpha_6 \frac{1}{r^2} \psi \tag{2.12a}$$

$$u_\theta = \alpha_7 \frac{\partial^2 \psi}{\partial r^2} + \alpha_8 \frac{1}{r} \frac{\partial^2 \psi}{\partial r \partial \theta} + \alpha_9 \frac{1}{r^2} \frac{\partial^2 \psi}{\partial \theta^2} + \alpha_{10} \frac{1}{r} \frac{\partial \psi}{\partial r} + \alpha_{11} \frac{1}{r^2} \frac{\partial \psi}{\partial \theta} + \alpha_{12} \frac{1}{r^2} \psi \tag{2.12b}$$

where, $\alpha$'s are unknown material constants. Here, the displacement components are expressed as a summation of different derivatives of the function multiplied by unknown constants. It has been found that the derivatives present in the assumed expression of displacement components [Eq. 2.12] are governed by the derivatives present in the equilibrium equations in terms of displacement components Eq. (2.9) [21, 22].

Substituting the above expressions of $u_r$ and $u_\theta$ in Eq. (2.9), we obtain the equilibrium equations in terms of the function $\psi$, which are

$$\left\{\alpha_3+\frac{1+\nu}{2}\alpha_8+\frac{1-\nu}{2}\alpha_1\right\}\frac{1}{r^2}\frac{\partial^4\psi}{\partial r^2\partial\theta^2}+\frac{1}{r^3}\frac{\partial^4\psi}{\partial r\partial\theta^3}\left\{\frac{1+\nu}{2}\alpha_9+\frac{1-\nu}{2}\alpha_2\right\}+\frac{1}{r^3}\frac{\partial^3\psi}{\partial r\partial\theta^2}\left\{-4\alpha_3+\frac{1+\nu}{2}(-\alpha_8\right.$$
$$\left.+\alpha_{11})+\frac{1-\nu}{2}\alpha_4+\alpha_3-\frac{3-\nu}{2}\alpha_8\right\}+\frac{1}{r^4}\frac{\partial^3\psi}{\partial\theta^3}\left\{-2\alpha_9\frac{1+\nu}{2}+\frac{1-\nu}{2}\alpha_5-\frac{3-\nu}{2}\alpha_9\right\}+\left\{6\alpha_3-\frac{1+\nu}{2}2\alpha_{11}\right.$$
$$\left.+\frac{1-\nu}{2}\alpha_6-2\alpha_3-\frac{3-\nu}{2}\alpha_{11}-\alpha_3\right\}\frac{1}{r^4}\frac{\partial^2\psi}{\partial\theta^2}+\alpha_3\frac{1-\nu}{2}\frac{1}{r^4}\frac{\partial^4\psi}{\partial\theta^4}+\frac{1}{r}\frac{\partial^4\psi}{\partial r^3\partial\theta}\left\{\alpha_2+\frac{1+\nu}{2}\alpha_7\right\}+\frac{1}{r^2}\frac{\partial^3\psi}{\partial r^2\partial\theta}$$
$$\left\{-2\alpha_2+\alpha_5+\frac{1+\nu}{2}\alpha_{10}+\alpha_2-\frac{3-\nu}{2}\alpha_7\right\}+\left\{\alpha_4+\alpha_1\right\}\frac{1}{r}\frac{\partial^3\psi}{\partial r^3}+\alpha_1\frac{\partial^4\psi}{\partial r^4}+\frac{1}{r^2}\frac{\partial^2\psi}{\partial r^2}\left\{-2\alpha_4+\alpha_6+\alpha_4-\alpha_1\right\}$$
$$+\left\{2\alpha_2-4\alpha_5+\frac{1+\nu}{2}(-\alpha_{10}+\alpha_{12})-\alpha_2+\alpha_5-\frac{3-\nu}{2}\alpha_{10}-\alpha_2\right\}\frac{1}{r^3}\frac{\partial^2\psi}{\partial r\partial\theta}+\frac{1}{r^3}\frac{\partial\psi}{\partial r}\left\{2\alpha_4-4\alpha_6+(-\alpha_4\right.$$
$$\left.+\alpha_6)-\alpha_4\right\}+\left\{6\alpha_5-2\frac{1+\nu}{2}\alpha_{12}+-2\alpha_5-\frac{3-\nu}{2}\alpha_{12}-\alpha_5\right\}\frac{1}{r^4}\frac{\partial\psi}{\partial\theta}+\frac{1}{r^4}\psi\left\{6\alpha_6-2\alpha_6-\alpha_6\right\}=0$$

$$\Rightarrow\alpha_1\frac{\partial^4\psi}{\partial r^4}+\frac{1}{r}\left\{\alpha_2+\frac{1+\nu}{2}\alpha_7\right\}\frac{\partial^4\psi}{\partial r^3\partial\theta}+\frac{1}{r^2}\left\{\alpha_3+\frac{1+\nu}{2}\alpha_8+\frac{1-\nu}{2}\alpha_1\right\}\frac{\partial^4\psi}{\partial r^2\partial\theta^2}+\frac{1}{r^3}\left\{\frac{1+\nu}{2}\alpha_9+\frac{1-\nu}{2}\alpha_2\right\}$$
$$\times\frac{\partial^4\psi}{\partial r\partial\theta^3}+\frac{1-\nu}{2r^4}\alpha_3\frac{\partial^4\psi}{\partial\theta^4}+\frac{1}{r}\left\{\alpha_4+\alpha_1\right\}\frac{\partial^3\psi}{\partial r^3}+\frac{1}{r^2}\left\{-\alpha_2+\alpha_5+\frac{1+\nu}{2}\alpha_{10}-\frac{3-\nu}{2}\alpha_7\right\}\frac{\partial^3\psi}{\partial r^2\partial\theta}+\frac{1}{r^3}\left\{-3\alpha_3\right.$$
$$\left.-2\alpha_8+\frac{1+\nu}{2}\alpha_{11}+\frac{1-\nu}{2}\alpha_4\right\}\frac{\partial^3\psi}{\partial r\partial\theta^2}+\frac{1}{r^4}\left\{\frac{-5-\nu}{2}\alpha_9+\frac{1-\nu}{2}\alpha_5\right\}\frac{\partial^3\psi}{\partial\theta^3}+\frac{1}{r^2}\left\{-\alpha_4+\alpha_6-\alpha_1\right\}\frac{\partial^2\psi}{\partial r^2}$$
$$+\frac{1}{r^3}\left\{-3\alpha_5-2\alpha_{10}+\frac{1+\nu}{2}\alpha_{12}\right\}\frac{\partial^2\psi}{\partial r\partial\theta}+\frac{1}{r^4}\left\{3\alpha_3-\frac{5+\nu}{2}\alpha_{11}+\frac{1-\nu}{2}\alpha_6\right\}\frac{\partial^2\psi}{\partial\theta^2}-\frac{3}{r^3}\alpha_6\frac{\partial\psi}{\partial r}$$
$$+\frac{1}{r^4}\left\{3\alpha_5-\frac{5+\nu}{2}\alpha_{12}\right\}\frac{\partial\psi}{\partial\theta}+\frac{3}{r^4}\alpha_6\psi=0 \qquad \text{(2.13 a)}$$

$$\frac{1}{r^2}\frac{\partial^4\psi}{\partial r^2\partial\theta^2}\left\{\alpha_7+\frac{1-\nu}{2}\alpha_9+\frac{1+\nu}{2}\alpha_2\right\}+\frac{1}{r^3}\frac{\partial^4\psi}{\partial r\partial\theta^3}\left\{\alpha_8+\frac{1+\nu}{2}\alpha_3\right\}+\frac{1}{r^3}\frac{\partial^3\psi}{\partial r\partial\theta^2}\left\{\alpha_{10}-\frac{1-\nu}{2}4\alpha_9+\frac{1-\nu}{2}\alpha_9\right.$$
$$\left.+\frac{1+\nu}{2}(-\alpha_2+\alpha_5)+\frac{3-\nu}{2}\alpha_2\right\}+\frac{1}{r^4}\frac{\partial^3\psi}{\partial\theta^3}\left\{\alpha_{11}-\frac{1+\nu}{2}2\alpha_3+\frac{3-\nu}{2}\alpha_3\right\}+\frac{1}{r^4}\frac{\partial^2\psi}{\partial\theta^2}\left\{\alpha_{12}+\frac{1-\nu}{2}6\alpha_9-\frac{1-\nu}{2}2\alpha_9\right.$$
$$\left.-\frac{1-\nu}{2}\alpha_9-\frac{1+\nu}{2}2\alpha_5+\frac{3-\nu}{2}\alpha_5\right\}+\frac{1}{r^4}\alpha_9\frac{\partial^4\psi}{\partial\theta^4}+\frac{1}{r}\frac{\partial^4\psi}{\partial r^3\partial\theta}\left\{\frac{1-\nu}{2}\alpha_8+\frac{1+\nu}{2}\alpha_1\right\}+\frac{1}{r^2}\frac{\partial^3\psi}{\partial r^2\partial\theta}\left\{\frac{1-\nu}{2}(-2\alpha_8+\alpha\right.$$
$$\left.+\alpha_{11})+\frac{1-\nu}{2}\alpha_8+\frac{1+\nu}{2}\alpha_4+\frac{3-\nu}{2}\alpha_1\right\}+\frac{1}{r}\frac{\partial^3\psi}{\partial r^3}\left(\frac{1-\nu}{2}\alpha_{10}+\frac{1-\nu}{2}\alpha_7\right)+\frac{1-\nu}{2}\alpha_7\frac{\partial^4\psi}{\partial r^4}+\frac{1}{r^2}\frac{\partial^2\psi}{\partial r^2}\left\{\frac{1-\nu}{2}(-2\alpha_{10}\right.$$
$$\left.+\alpha_{12})+\frac{1-\nu}{2}\alpha_{10}+\frac{\nu-1}{2}\alpha_7)\right\}+\frac{1}{r^3}\frac{\partial^2\psi}{\partial r\partial\theta}\left\{\frac{1-\nu}{2}(2\alpha_8-4\alpha_{11})+\frac{1-\nu}{2}(-\alpha_8+\alpha_{11})+\frac{\nu-1}{2}\alpha_8+\frac{1+\nu}{2}(-\alpha_4+\alpha_6)\right.$$
$$\left.+\frac{3-\nu}{2}\alpha_4\right\}+\frac{1}{r^3}\frac{\partial\psi}{\partial r}\left\{\frac{1-\nu}{2}(2\alpha_{10}-4\alpha_{12})+\frac{1-\nu}{2}(-\alpha_{10}+\alpha_{12})+\frac{\nu-1}{2}\alpha_{10}\right\}+\frac{1}{r^4}\frac{\partial\psi}{\partial\theta}\left\{\frac{1-\nu}{2}6\alpha_{11}-\frac{1-\nu}{2}2\alpha_{11}\right.$$
$$\left.+\frac{\nu-1}{2}\alpha_{11}-\frac{1+\nu}{2}2\alpha_6+\frac{3-\nu}{2}\alpha_6\right\}+\frac{1}{r^4}\psi\left\{\frac{1-\nu}{2}6\alpha_{12}-\frac{1-\nu}{2}2\alpha_{12}+\frac{\nu-1}{2}\alpha_{12}\right\}=0$$

$$\Rightarrow\frac{1-\nu}{2}\alpha_7\frac{\partial^4\psi}{\partial r^4}+\frac{1}{r}\left\{\frac{1-\nu}{2}\alpha_8+\frac{1+\nu}{2}\alpha_1\right\}\frac{\partial^4\psi}{\partial r^3\partial\theta}+\frac{1}{r^2}\left\{\alpha_7+\frac{1-\nu}{2}\alpha_9+\frac{1+\nu}{2}\alpha_2\right\}\frac{\partial^4\psi}{\partial r^2\partial\theta^2}+\frac{1}{r^3}\left\{\alpha_8+\frac{1+\nu}{2}\alpha_3\right\}$$
$$\times\frac{\partial^4\psi}{\partial r\partial\theta^3}+\frac{1}{r^4}\alpha_9\frac{\partial^4\psi}{\partial\theta^4}+\frac{1}{r}\left\{\frac{1-\nu}{2}\alpha_{10}+\frac{1-\nu}{2}\alpha_7\right\}\frac{\partial^3\psi}{\partial r^3}+\frac{1}{r^2}\left\{-\frac{1-\nu}{2}\alpha_8+\frac{1-\nu}{2}\alpha_{11}+\frac{1+\nu}{2}\alpha_4+\frac{3-\nu}{2}\alpha_1\right\}\frac{\partial^3\psi}{\partial r^2\partial\theta}$$
$$+\frac{1}{r^3}\left\{\alpha_{10}-\frac{3(1-\nu)}{2}\alpha_9+(1-\nu)\alpha_2+\frac{1+\nu}{2}\alpha_5\right\}\frac{\partial^3\psi}{\partial r\partial\theta^2}+\frac{1}{r^4}\left\{\alpha_{11}+\frac{1-3\nu}{2}\alpha_3\right\}\frac{\partial^3\psi}{\partial\theta^3}+\frac{1}{r^2}\left\{-\frac{1-\nu}{2}\alpha_{10}+\frac{1-\nu}{2}\alpha_{12}\right.$$
$$\left.-\frac{1-\nu}{2}\alpha_7)\right\}\frac{\partial^2\psi}{\partial r^2}+\frac{1}{r^3}\left\{-\frac{3(1-\nu)}{2}\alpha_{11}+(1-\nu)\alpha_4+\frac{1+\nu}{2}\alpha_6\right\}\frac{\partial^2\psi}{\partial r\partial\theta}+\frac{1}{r^4}\left\{\alpha_{12}+\frac{3(1-\nu)}{2}\alpha_9+\frac{1-3\nu}{2}\alpha_5\right\}\frac{\partial^2\psi}{\partial\theta^2}$$
$$-\frac{3(1-\nu)}{2r^3}\alpha_{12}\frac{\partial\psi}{\partial r}+\frac{1}{r^4}\left\{\frac{3(1-\nu)}{2}\alpha_{11}+\frac{1-3\nu}{2}\alpha_6\right\}\frac{\partial\psi}{\partial\theta}+\frac{3(1-\nu)}{2r^4}\alpha_{12}\psi=0 \qquad (2.13\text{ b})$$

The unknown α's are now chosen in such a way that one out of two conditions of equilibrium [Eqs. 2.13] is automatically satisfied under all possible circumstances. This will happen only when the coefficients of $\psi$ and all its derivatives present in either of the two equations (2.13a) and (2.13b) are individually zero. The two equilibrium equations [Eq. 2.13] are treated here separately and the resulting formulations are named as Formulation-I and Formulation-II, respectively.

### 2.4.1 Formulation-I

In this formulation, attempt is made to automatically satisfy the first equilibrium equation [Eq. 2.13(a)]. Equating all the coefficients of $\psi$ and all its derivatives present in Eq. (2.13a) to zero, the resulting conditions are obtained as follows:

$$\alpha_i = 0 \quad (i = 1,\ 3,\ 4,\ 6,\ 8,\ 11) \tag{2.14a}$$

$$\alpha_2 + \frac{1+v}{2}\alpha_7 = 0 \tag{2.14b}$$

$$\frac{1+v}{2}\alpha_9 + \frac{1-v}{2}\alpha_2 = 0 \tag{2.14c}$$

$$-\alpha_2 + \alpha_5 - \frac{3-v}{2}\alpha_7 + \frac{1+v}{2}\alpha_{10} = 0 \tag{2.14d}$$

$$\frac{1-v}{2}\alpha_5 - \frac{5+v}{2}\alpha_9 = 0 \tag{2.14e}$$

$$-3\alpha_5 - 2\alpha_{10} + \frac{1+v}{2}\alpha_{12} = 0 \tag{2.14f}$$

$$3\alpha_5 - \frac{5+v}{2}\alpha_{12} = 0 \tag{2.14g}$$

Further manipulating the Eqs. 2.14(b)-2.14(g), one can find the following conditions:

$$\alpha_2 = -\frac{1+v}{2}\alpha_7 \tag{2.15a}$$

$$\alpha_5 = \frac{5+v}{2}\alpha_7 \tag{2.15b}$$

$$\alpha_9 = \frac{1-v}{2}\alpha_7 \tag{2.15c}$$

$$\alpha_{10} = -3\alpha_7 \tag{2.15d}$$

$$\alpha_{12} = 3\alpha_7 \tag{2.15e}$$

One can see from Eq. (2.15) that, there are five equations for obtaining six unknowns. One can thus assign an arbitrary value to any one of these six unknowns and solve for the remaining five $\alpha$'s from Eq. (2.15). Let us assign an arbitrary value, for example, unity, to the unknown $\alpha_7$. That is, let $\alpha_7 = 1$. Then, solving Eq. (2.15), the values of all unknown $\alpha$'s can be expressed as follows:

$$\alpha_2 = -\frac{1+v}{2} \tag{2.16a}$$

$$\alpha_5 = \frac{5+v}{2} \tag{2.16b}$$

$$\alpha_9 = \frac{1-v}{2} \tag{2.16c}$$

$$\alpha_{10} = -3 \tag{2.16d}$$

$$\alpha_{12} = 3 \tag{2.16e}$$

$$\alpha_7 = 1 \tag{2.16f}$$

$$\alpha_i = 0 \qquad (i = 1,\ 3,\ 4,\ 6,\ 8,\ 11) \tag{2.16g}$$

It would be worth mentioning here that, any other value of $\alpha_7$ could have been chosen leaving aside the homogeneous solution. Different values of $\alpha_7$ will make the coefficients of the unknown $\psi$ different. The values of $\alpha_7$ which will lead to the diagonal dominance of the algebraic equations of unknown $\psi$ at the nodal points are desirable in terms of increasing accuracy and shorter computational time. $\alpha_7$ = 1 leads to the most simplified differential equations and hence well-conditioned algebraic equations.

The problem has now been reduced to the solution of a single function $\psi$ from a single fourth-order partial differential equation (2.13b). As the conditions of Eq. (2.16) identically satisfy Eq. (2.13a), substitution of the conditions of Eqs. (2.16) in Eq. (2.13b) gives,

$$\frac{\partial^4\psi}{\partial r^4} + \frac{1}{r^4}\frac{\partial^4\psi}{\partial\theta^4} + \frac{2}{r^2}\frac{\partial^4\psi}{\partial r^2\partial\theta^2} - \frac{2}{r}\frac{\partial^3\psi}{\partial r^3} - \frac{6}{r^3}\frac{\partial^3\psi}{\partial r\partial\theta^2} + \frac{5}{r^2}\frac{\partial^2\psi}{\partial r^2} + \frac{10}{r^4}\frac{\partial^2\psi}{\partial\theta^2} - \frac{9}{r^3}\frac{\partial\psi}{\partial r} + \frac{9}{r^4}\psi = 0 \tag{2.17}$$

Eq. (2.17) gives the explicit expression of the single governing differential equation of equilibrium for the solution of plane elastic problems in polar coordinate system in terms of the potential function $\psi$.

### 2.4.2 Formulation-II

In Formulation- II, equilibrium Eq. (2.13b) is considered so that it can be automatically satisfied. Likewise the case of Formulation- I, equating all the coefficients of $\psi$ and its derivatives to zero, the following conditions are obtained:

$$\alpha_i = 0 \qquad (i = 2,\ 5,\ 7,\ 9,\ 10,\ 12) \tag{2.18a}$$

$$\alpha_3 = -\frac{2}{1-3\nu}\alpha_{11} \tag{2.18b}$$

$$\alpha_8 = \frac{1+\nu}{1-3\nu}\alpha_{11} \tag{2.18c}$$

$$\alpha_1 = -\frac{1-\nu}{1-3\nu}\alpha_{11} \tag{2.18d}$$

$$\alpha_6 = -\frac{3-3\nu}{1-3\nu}\alpha_{11} \tag{2.18e}$$

$$\alpha_4 = \frac{3(1-\nu)}{1-3\nu}\alpha_{11} \tag{2.18f}$$

One can see from Eq. (2.18b)-(2.18f) that, again there are five equations for obtaining six unknowns. One can thus assign an arbitrary value to any one of these six unknowns and solve for the remaining five $\alpha$'s from Eq. (2.18). Taking $\alpha_{11}$=1, all the values of unknown $\alpha$'s can be determined from Eq. (2.18) which are as follows:

$$\alpha_1 = -\frac{1-\nu}{1-3\nu} \tag{2.19a}$$

$$\alpha_3 = -\frac{2}{1-3\nu} \tag{2.19b}$$

$$\alpha_4 = \frac{3(1-\nu)}{1-3\nu} \tag{2.19c}$$

$$\alpha_6 = -\frac{3-3\nu}{1-3\nu} \tag{2.19d}$$

$$\alpha_8 = \frac{1+\nu}{1-3\nu} \tag{2.19e}$$

$$\alpha_{11} = 1 \tag{2.19f}$$

$$\alpha_i = 0 \quad (i = 2,\ 5,\ 7,\ 9,\ 10,\ 12) \tag{2.19g}$$

Substitution of the conditions of Eq. (2.19) into Eq. (2.13a) gives the resulting differential equation for Formulation-II, which is,

$$\frac{\partial^4\psi}{\partial r^4} + \frac{1}{r^4}\frac{\partial^4\psi}{\partial\theta^4} + \frac{2}{r^2}\frac{\partial^4\psi}{\partial r^2\partial\theta^2} - \frac{2}{r}\frac{\partial^3\psi}{\partial r^3} - \frac{6}{r^3}\frac{\partial^3\psi}{\partial r\partial\theta^2} + \frac{5}{r^2}\frac{\partial^2\psi}{\partial r^2} + \frac{10}{r^4}\frac{\partial^2\psi}{\partial\theta^2} - \frac{9}{r^3}\frac{\partial\psi}{\partial r} + \frac{9}{r^4}\psi = 0 \tag{2.20}$$

It can be seen that Eq. (2.20) gives the same partial differential equation in terms of the potential function $\psi$ as given by Eq. (2.17) of Formulation-I. It is thus verified that both the formulations give the same governing differential equation for the function $\psi$, which, in turn, establishes the fact that the present potential function formulation is funded on sound philosophy.

## 2.5 BOUNDARY CONDITIONS

The physical conditions specified along the edges or boundaries of a body are visualized in terms of either known restraints or forces or a combination of the two. Mixed-boundary-value problems are those in which the boundary conditions are specified as a mixture of boundary restraints and boundary loading, where the combination of boundary conditions may also change from point to point. Both the restraints, that is, known displacements, and the tractions, that is known forces are defined by their respective components, namely,

(a) Normal displacement ($u_n$)

(b) Tangential displacement ($u_t$)

(c) Normal stress ($\sigma_n$)

(d) Tangential stress ($\sigma_t$)

Now the solution of the governing equation requires two boundary conditions to be known at any point on the boundary. Therefore, the possible boundary conditions created out of the four components are,

(1) ($\sigma_n$, $\sigma_t$),

(2) ($\sigma_n, u_n$),

(3) ($\sigma_n, u_t$),

(4) ($\sigma_t, u_t$),

(5) ($u_n, \sigma_t$) and

(6) ($u_n, u_t$).

However, the combination ($\sigma_n, u_n$) and ($\sigma_t, u_t$) do not usually occur in practice. The remaining four possible boundary conditions with reference to a polar coordinate system ($r, \theta$) are as follows:

For surfaces along radial direction:

(i) $\sigma_\theta\ (r, \theta)$ and $\tau_{r\theta}\ (r, \theta)$

(ii) $\sigma_\theta\ (r, \theta)$ and $u_r\ (r, \theta)$

(iii) $u_\theta\ (r, \theta)$ and $\tau_{r\theta}\ (r, \theta)$

(iv) $u_r\ (r, \theta)$ and $u_\theta\ (r, \theta)$

For surfaces along circumferential directions:

(i) $\sigma_r\ (r, \theta)$ and $\tau_{r\theta}\ (r, \theta)$

(ii) $\sigma_r\ (r, \theta)$ and $u_\theta\ (r, \theta)$

(iii) $u_r\ (r, \theta)$ and $\tau_{r\theta}\ (r, \theta)$

(iv) $u_r\ (r, \theta)$ and $u_\theta\ (r, \theta)$

Therefore, all the possible boundary conditions on different bounding edges of a 2-D curved body are basically different combinations of two displacement components ($u_r, u_\theta$) and three stress components ($\sigma_r, \sigma_\theta, \tau_{r\theta}$). Since our objective is to solve the problem in terms of the potential function $\psi$, all the boundary conditions of interest are required to be expressed in terms of the function $\psi$.

The components of displacement in terms of $\psi$ are given by Eqs. (2.12a) and (2.12b). General expressions for the components of stress in terms of the function $\psi$ are obtained when the

displacement components in the stress-displacement relations Eq. (2.7) is replaced by those of Eq. (2.12). They are,

$$\sigma_r = \frac{E}{1-\nu^2}\left[\begin{array}{l} \alpha_1 \frac{\partial^3\psi}{\partial r^3} + \frac{1}{r}(\alpha_2 + \nu\alpha_7)\frac{\partial^3\psi}{\partial r^2\partial\theta} + \frac{1}{r^2}(\alpha_3 + \nu\alpha_8)\frac{\partial^3\psi}{\partial r\partial\theta^2} + \frac{1}{r^3}\nu\alpha_9\frac{\partial^3\psi}{\partial\theta^3} + \frac{1}{r}(\alpha_4 + \nu\alpha_1) \\ \times \frac{\partial^2\psi}{\partial r^2} + \frac{1}{r^2}\{(\nu-1)\alpha_2 + \alpha_5 + \nu\alpha_{10}\}\frac{\partial^2\psi}{\partial r\partial\theta} + \frac{1}{r^3}\{(\nu-2)\alpha_3 + \nu\alpha_{11}\}\frac{\partial^2\psi}{\partial\theta^2} \\ + \frac{1}{r^2}\{(\nu-1)\alpha_4 + \alpha_6\}\frac{\partial\psi}{\partial r} + \frac{1}{r^3}\{(\nu-2)\alpha_5 + \alpha_{12}\}\frac{\partial\psi}{\partial\theta} + \frac{1}{r^3}(\nu-2)\alpha_6\psi \end{array}\right] \tag{2.21a}$$

$$\sigma_\theta = \frac{E}{1-\nu^2}\left[\begin{array}{l} \nu\alpha_1 \frac{\partial^3\psi}{\partial r^3} + \frac{1}{r}(\nu\alpha_2 + \alpha_7)\frac{\partial^3\psi}{\partial r^2\partial\theta} + \frac{1}{r^2}(\nu\alpha_3 + \alpha_8)\frac{\partial^3\psi}{\partial r\partial\theta^2} + \frac{1}{r^3}\alpha_9\frac{\partial^3\psi}{\partial\theta^3} + \frac{1}{r}(\nu\alpha_4 + \alpha_1) \\ \times \frac{\partial^2\psi}{\partial r^2} + \frac{1}{r^2}\{(1-\nu)\alpha_2 + \nu\alpha_5 + \alpha_{10}\}\frac{\partial^2\psi}{\partial r\partial\theta} + \frac{1}{r^3}\{(1-2\nu)\alpha_3 + \alpha_{11}\}\frac{\partial^2\psi}{\partial\theta^2} \\ + \frac{1}{r^2}\{(1-\nu)\alpha_4 + \nu\alpha_6\}\frac{\partial\psi}{\partial r} + \frac{1}{r^3}\{(1-2\nu)\alpha_5 + \alpha_5 + \nu\alpha_{12}\}\frac{\partial\psi}{\partial\theta} + \frac{1}{r^3}(1-2\nu)\alpha_6\psi \end{array}\right] \tag{2.21b}$$

$$\tau_{r\theta} = \frac{E}{1-\nu^2}\left[\begin{array}{l} \alpha_7 \frac{\partial^3\psi}{\partial r^3} + \frac{1}{r}(\alpha_1 + \alpha_8)\frac{\partial^3\psi}{\partial r^2\partial\theta} + \frac{1}{r^2}(\alpha_2 + \alpha_9)\frac{\partial^3\psi}{\partial r\partial\theta^2} + \frac{1}{r^3}\alpha_3\frac{\partial^3\psi}{\partial\theta^3} + \frac{1}{r}(\alpha_{10} - \alpha_7)\frac{\partial^2\psi}{\partial r^2} \\ + \frac{1}{r^2}(\alpha_4 - 2\alpha_8 + \alpha_{11})\frac{\partial^2\psi}{\partial r\partial\theta} + \frac{1}{r^3}(\alpha_5 - 3\alpha_9)\frac{\partial^2\psi}{\partial\theta^2} + \frac{1}{r^2}(\alpha_{12} - 2\alpha_{10})\frac{\partial\psi}{\partial r} \\ + \frac{1}{r^3}(\alpha_6 - 3\alpha_{11})\frac{\partial\psi}{\partial\theta} - \frac{1}{r^3}3\alpha_{12}\psi \end{array}\right] \tag{2.21c}$$

### 2.5.1 Displacement and stress components in terms of $\psi$ for Formulation-I

Substitution of the values of α's from Eq. (2.16) to Eqs. (2.12) and (2.21) gives the explicit expressions of the components of displacement and stress in terms of $\psi$ as follows:

$$u_r(r,\theta) = -\frac{1+\nu}{2r}\frac{\partial^2\psi}{\partial r\partial\theta} + \frac{5+\nu}{2r^2}\frac{\partial\psi}{\partial\theta} \tag{2.22}$$

$$u_\theta(r,\theta) = \frac{\partial^2\psi}{\partial r^2} + \frac{1-\nu}{2r^2}\frac{\partial^2\psi}{\partial\theta^2} - \frac{3}{r}\frac{\partial\psi}{\partial r} + \frac{3}{r^2}\psi \tag{2.23}$$

$$\sigma_r(r,\theta) = \frac{E}{2(1+\nu)}\left[-\frac{1}{r}\frac{\partial^3\psi}{\partial r^2\partial\theta} + \frac{\nu}{r^3}\frac{\partial^3\psi}{\partial\theta^3} + \frac{(6+\nu)}{r^2}\frac{\partial^2\psi}{\partial r\partial\theta} - \frac{\partial\psi}{\partial\theta}\frac{(10+\nu)}{r^3}\right] \tag{2.24}$$

$$\sigma_\theta(r,\theta)=\frac{E}{2(1+\nu)}\left[\frac{(2+\nu)}{r}\frac{\partial^3\psi}{\partial r^2\partial\theta}+\frac{1}{r^3}\frac{\partial^3\psi}{\partial\theta^3}-\frac{(7+2\nu)}{r^2}\frac{\partial^2\psi}{\partial r\partial\theta}+\frac{(11+2\nu)}{r^3}\frac{\partial\psi}{\partial\theta}\right] \tag{2.25}$$

$$\tau_{r\theta}(r,\theta)=\frac{E}{2(1+\nu)}\left[\frac{\partial^3\psi}{\partial r^3}-\frac{\nu}{r^2}\frac{\partial^3\psi}{\partial r\partial\theta^2}-\frac{4}{r}\frac{\partial^2\psi}{\partial r^2}+\frac{(1+2\nu)}{r^3}\frac{\partial^2\psi}{\partial\theta^2}+\frac{9}{r^2}\frac{\partial\psi}{\partial r}-\frac{9}{r^3}\psi\right] \tag{2.26}$$

### 2.5.2 Displacement and stress components in terms of $\psi$ for Formulation-II

In this case the values of α's are taken from Eq. (2.19) and are substituted in Eqs. (2.12) and (2.21) to get the expressions of displacement and stress components as follows:

$$u_r(r,\theta)=\frac{1}{(1-3\nu)}\left[-(1-\nu)\frac{\partial^2\psi}{\partial r^2}-\frac{2}{r^2}\frac{\partial^2\psi}{\partial\theta^2}+\frac{3(1-\nu)}{r}\frac{\partial\psi}{\partial r}-\frac{3(1-\nu)}{r^2}\psi\right] \tag{2.27}$$

$$u_\theta(r,\theta)=\frac{1}{(1-3\nu)}\left[\frac{1+\nu}{r}\frac{\partial^2\psi}{\partial r\partial\theta}+\frac{1-3\nu}{r^2}\frac{\partial\psi}{\partial\theta}\right] \tag{2.28}$$

$$\sigma_r(r,\theta)=\frac{E}{(1+\nu)(1-3\nu)}\left[\begin{array}{l}-\frac{\partial^3\psi}{\partial r^3}-\frac{(2+\nu)}{r^2}\frac{\partial^3\psi}{\partial r\partial\theta^2}+\frac{(3-\nu)}{r}\frac{\partial^2\psi}{\partial r^2}+\frac{(4+3\nu)}{r^3}\frac{\partial^2\psi}{\partial\theta^2}-\frac{3(2-\nu)}{r^2}\frac{\partial\psi}{\partial r}\\+\frac{3(2-\nu)}{r^3}\psi\end{array}\right] \tag{2.29}$$

$$\sigma_\theta(r,\theta)=\frac{E}{(1+\nu)(1-3\nu)}\left[\begin{array}{l}-\nu\frac{\partial^3\psi}{\partial r^3}+\frac{1}{r^2}\frac{\partial^3\psi}{\partial r\partial\theta^2}-\frac{(1-3\nu)}{r}\frac{\partial^2\psi}{\partial r^2}-\frac{1}{r^3}\frac{\partial^2\psi}{\partial\theta^2}+\frac{3(1-2\nu)}{r^2}\frac{\partial\psi}{\partial r}\\-\frac{3(1-2\nu)}{r^3}\psi\end{array}\right] \tag{2.30}$$

$$\tau_{r\theta}(r,\theta)=\frac{E}{(1+\nu)(1-3\nu)}\left[\frac{\nu}{r}\frac{\partial^3\psi}{\partial r^2\partial\theta}-\frac{1}{r^3}\frac{\partial^3\psi}{\partial\theta^3}+\frac{1-4\nu}{r^2}\frac{\partial^2\psi}{\partial r\partial\theta}-\frac{3(1-2\nu)}{r^3}\frac{\partial\psi}{\partial\theta}\right] \tag{2.31}$$

It can be noted here that the corresponding components of strain can readily be obtained by differentiating the displacement components expressed in terms of the function $\psi$.

Chapter 03

# NUMERICAL FORMULATION

## 3.1 INTRODUCTION TO FINITE DIFFERENCE METHOD

The method of finite difference is an approximate technique which yields a direct simplified solution form, in which the differential equations of equilibrium and the boundary conditions are replaced by a set of algebraic equations. The general approach of finite difference solution assumes that the function can be represented in a prescribed range with a sufficient degree of accuracy either by Taylor's series with origin at the successive pivotal points of the range or the polynomial which passes through a certain number of selected pivotal points. The values of the functions at the nodal points are required to satisfy difference equations obtained by replacing the partial derivatives by their difference formulae. All finite difference formulae are approximations to infinite series of differences. Therefore, it is necessary that the series should converge, or that the error, caused by truncation after a certain number of terms should be sufficiently small. In this problem the pivotal points are taken as the regular net points of the domain of dependence of the functions obtained y dividing the domain by lines parallel to the co-ordinate axes.

## 3.2 DIFFERENCE FORMULAE OF DERIVATIVES

It will be appropriate to derive the finite difference formulae of the different derivatives to show the underlying principle as well as to obtain the truncation error of these expressions. To illustrate the derivation of the difference equations, a general pivotal point of co-ordinates $(r,\theta)$ is taken and its neighboring points are designed as shown in Fig. (3.1). The neighboring points are at distances $h\ (=\Delta r)$ and $k\ (=\Delta\theta)$ in the $r$ and $\theta$ directions, respectively.

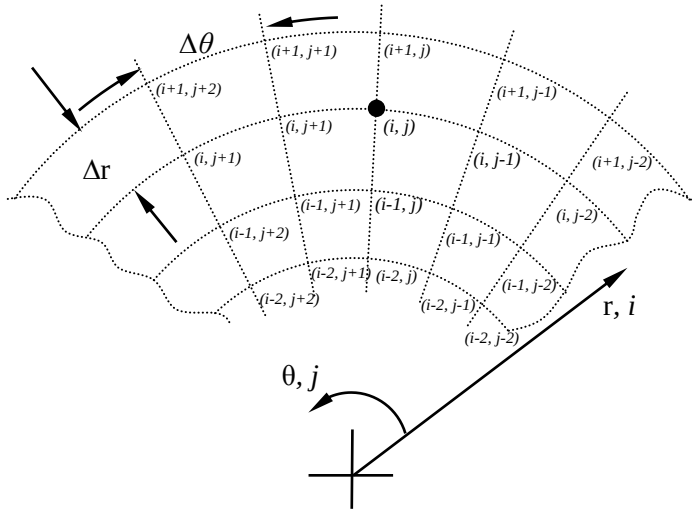


**Figure 3.1:** Finite difference discretization of the physical domain.

Assuming that a certain function *f(r,θ)* has continuous partial derivative of considerable higher order at (*r,θ*), the value of the function at point (*r+h, θ*) can be written by Taylor series expansion in terms of the values of the function and its derivatives at (*r, θ*) as,

$$f\left(r+h,\theta\right)=f\left(r,\theta\right)+hf_r\left(r,\theta\right)+\frac{h^2}{2!}f_{rr}\left(r,\theta\right)+\frac{h^3}{3!}f_{rrr}\left(r,\theta\right)+\ldots \tag{3.1}$$

The function at (*r-h,θ*) can be similarly written as

$$f\left(r-h,\theta\right)=f\left(r,\theta\right)-hf_r\left(r,\theta\right)+\frac{h^2}{2!}f_{rr}\left(r,\theta\right)-\frac{h^3}{3!}f_{rrr}\left(r,\theta\right)+\ldots \tag{3.2}$$

Subtracting these two Eqs. (3.1) and (3.2) we get,

$$f_r(r,\theta)=\left(\frac{\partial f}{\partial r}\right)_{r,\theta}=\frac{f\left(r+h,\theta\right)-f\left(r-h,\theta\right)}{2h}+O\left(h^2\right)$$

$$\Rightarrow\left(\frac{\partial f}{\partial r}\right)_{i,j}=\frac{f\left(i+1,j\right)-f\left(i-1,j\right)}{2h}+O\left(h^2\right) \tag{3.3}$$

Adding the same equations we get,

$$f_{rr}(r,\theta)=\left(\frac{\partial^2 f}{\partial r^2}\right)_{r,\theta}=\frac{f\left(r+h,\theta\right)-2f(r,\theta)+f(r-h,\theta)}{h^2}+O\left(h^2\right)$$

$$\Rightarrow\left(\frac{\partial^2 f}{\partial r^2}\right)_{i,j}=\frac{f\left(i+1,j\right)-2f(i,j)+f(i-1,j)}{h^2}+O\left(h^2\right) \tag{3.4}$$

Where, $h = \Delta r$ and $i, j$ stands for $r$ and $\theta$- directions respectively, in such a way that $i+1=r+h$ and $i-1 = r-h$ and so on. The term '$O(h^2)$' indicates that an error of order $h^2$.

Eqs. (3.3) and (3.4) give the central difference expressions for 1st and 2nd derivatives respectively. The two point forward and backward difference equations for 1st derivative can be obtained from the Eqs. (3.1) and (3.2) respectively as follows:

From Eq. (3.1) we get,

$$f_r(r,\theta)=\left(\frac{\partial f}{\partial r}\right)_{r,\theta}=\frac{f\left(r+h,\theta\right)-f(r,\theta)}{h}-\frac{h^2}{2!}f_{rr}\left(r,\theta\right)-\frac{h^3}{3!}f_{rrr}\left(r,\theta\right)+\ldots$$

$$\Rightarrow\left(\frac{\partial f}{\partial r}\right)_{r,\theta}=\frac{f\left(r+h,\theta\right)-f(r,\theta)}{h}+O(h)$$

$$\Rightarrow\left(\frac{\partial f}{\partial r}\right)_{i,j}=\frac{f\left(i+1,j\right)-f(i,j)}{h}+O\left(h\right) \tag{3.5}$$

From Eq. (4.2) we get,

$$f_r(r,\theta)=\left(\frac{\partial f}{\partial r}\right)_{r,\theta}=\frac{f\left(r,\theta\right)-f(r-h,\theta)}{h}+\frac{h^2}{2!}f_{rr}\left(r,\theta\right)-\frac{h^3}{3!}f_{rrr}\left(r,\theta\right)+\ldots$$

$$\Rightarrow\left(\frac{\partial f}{\partial r}\right)_{r,\theta}=\frac{f\left(r,\theta\right)-f(r-h,\theta)}{h}+O(h)$$

$$\Rightarrow\left(\frac{\partial f}{\partial r}\right)_{i,j}=\frac{f\left(i+1,j\right)-f(i,j)}{h}+O\left(h\right) \tag{3.6}$$

Similarly using the tailor series expansion the three point forward and backward difference equations can be obtained. Three point forward and backward difference equations for first and second order derivatives are given below.

$$\left(\frac{\partial f}{\partial r}\right)_{i,j}=\frac{-f\left(i+2,j\right)+4f\left(i+1,j\right)-3f\left(i,j\right)}{2h}+O\left(h^2\right) \tag{3.7}$$

$$\left(\frac{\partial^2 f}{\partial r^2}\right)_{i,j} = \frac{f(i+2,j) - 2f(i+1,j) + f(i,j)}{h^2} + O(h) \tag{3.8}$$

$$\left(\frac{\partial f}{\partial r}\right)_{i,j} = \frac{3f(i,j) - 4f(i-1,j) + f(i-2,j)}{2h} + O(h^2) \tag{3.9}$$

$$\left(\frac{\partial^2 f}{\partial r^2}\right)_{i,j} = \frac{f(i,j) - 2f(i-1,j) + f(i-2,j)}{h^2} + O(h) \tag{3.10}$$

The above two second order derivatives are of accuracy of *O(h)*. For higher order accuracy four point expressions are used which are given below.

$$\left(\frac{\partial^2 f}{\partial r^2}\right)_{i,j} = \frac{-f(i+3,j) + 4f(i+2,j) - 5f(i+1,j) + 2f(i,j)}{h^2} + O(h^2) \tag{3.11}$$

$$\left(\frac{\partial^2 f}{\partial r^2}\right)_{i,j} = \frac{2f(i,j) - 5f(i-1,j) + 4f(i-2,j) - f(i-3,j)}{h^2} + O(h^2) \tag{3.12}$$

Finite difference expression for higher order derivatives can be obtained by using the above expressions. Different combinations of central difference, forward difference and backward difference formulae can be used for this purpose. Some of the expressions of higher order derivatives and cross derivatives used in this thesis are obtained as shown below.

$$\left(\frac{\partial^3 f}{\partial r^3}\right)_{i,j} = \frac{\partial}{\partial r}\left(\frac{\partial^2 f}{\partial r^2}\right)_{i,j}$$

$$\Rightarrow \left(\frac{\partial^3 f}{\partial r^3}\right)_{i,j} = \left(\frac{\partial z}{\partial r}\right)_{i,j}$$

$$\Rightarrow \left(\frac{\partial^3 f}{\partial r^3}\right)_{i,j} = \frac{z(i+1,j) - z(i-1,j)}{2h}$$

$$\Rightarrow \left(\frac{\partial^3 f}{\partial r^3}\right)_{i,j} = \frac{f(i+2,j) - 2f(i+1,j) + 2f(i-1,j) - f(i-2,j)}{2h^3} + O(h^2) \tag{3.13}$$

where, $z = \left(\frac{\partial^2 f}{\partial r^2}\right)$

This expression is formed by combining two central difference expressions. Similarly, expression for the same derivative using a central difference and a forward difference and a central difference and a backward difference are respectively,

$$\left(\frac{\partial^3 f}{\partial r^3}\right)_{i,j} = \frac{f(i+2,j) - 3f(i+1,j) + 3f(i,j) - f(i-1,j)}{h^3} + O(h) \tag{3.14}$$

$$\left(\frac{\partial^3 f}{\partial r^3}\right)_{i,j} = \frac{f(i+1,j) - 3f(i,j) + 3f(i-1,j) - f(i-2,j)}{h^3} + O(h) \tag{3.15}$$

The above two expressions are of lower error order *(O(h))*. To get the equation with error order $O(h^2)$, higher order $(O(h^2))$ forward and backward expression is needed to be used.

Using three point $(O(h^2))$ forward and backward Eqs. (3.7) and (3.9) we get,

$$\left(\frac{\partial^3 f}{\partial r^3}\right)_{i,j} = \frac{-f(i+3,j) + 6f(i+2,j) - 12f(i+1,j) + 10f(i,j) - 3f(i-1,j)}{2h^3} + O(h^2) \tag{3.16}$$

$$\left(\frac{\partial^3 f}{\partial r^3}\right)_{i,j} = \frac{3f(i+1,j) - 10f(i,j) + 12f(i-1,j) - 6f(i-2,j) + f(i-3,j)}{2h^3} + O(h^2) \tag{3.17}$$

For the case of forth order derivative, the finite difference expression using two central difference expressions can be obtained as,

$$\left(\frac{\partial^4 f}{\partial r^4}\right)_{i,j} = \frac{\partial^2}{\partial r^2}\left(\frac{\partial^2 f}{\partial r^2}\right)_{i,j}$$

$$\Rightarrow \left(\frac{\partial^4 f}{\partial r^4}\right)_{i,j} == \left(\frac{\partial^2 z}{\partial r^2}\right)_{i,j}$$

$$\Rightarrow \left(\frac{\partial^4 f}{\partial r^4}\right)_{i,j} = \frac{z(i+1,j) - 2z(i,j) + z(i-1,j)}{h^2}$$

$$\Rightarrow \left(\frac{\partial^4 f}{\partial r^4}\right)_{i,j} = \frac{f(i+2,j) - 4f(i+1,j) + 6f(i,j) - 4f(i-1,j) + f(i-2,j)}{h^4} + O(h^2) \tag{3.18}$$

where, $z = \left(\frac{\partial^2 f}{\partial r^2}\right)$

Fourth order derivative with a combination of center difference and four point forward expressions of the second order derivative can be obtained as follows:

$$\left(\frac{\partial^4 f}{\partial r^4}\right)_{i,j} = \frac{\partial^2}{\partial r^2}\left(\frac{\partial^2 f}{\partial r^2}\right)_{i,j}$$

$$\Rightarrow \left(\frac{\partial^4 f}{\partial r^4}\right)_{i,j} == \left(\frac{\partial^2 z}{\partial r^2}\right)_{i,j}$$

$$\Rightarrow \left(\frac{\partial^4 f}{\partial r^4}\right)_{i,j} = \frac{z(i+1,j) - 2z(i,j) + z(i-1,j)}{h^2}$$

$$\Rightarrow \left(\frac{\partial^4 f}{\partial r^4}\right)_{i,j} = \frac{1}{h^4}\begin{bmatrix} \{-f(i+4,j) + 4f(i+3,j) - 5f(i+2,j) + 2f(i+1,j)\} \\ -2\{-f(i+3,j) + 4f(i+2,j) - 5f(i+1,j) + 2f(i,j)\} \\ +\{-f(i+2,j) + 4f(i+1,j) - 5f(i,j) + 2f(i-1,j)\} \end{bmatrix}$$

$$\Rightarrow \left(\frac{\partial^4 f}{\partial r^4}\right)_{i,j} = \frac{1}{h^4}\begin{bmatrix} -f(i+4,j) + 6f(i+3,j) - 14f(i+2,j) - 16f(i+1,j) \\ -9f(i,j) + 2f(i-1,j) \end{bmatrix} + O\left(h^2\right) \qquad (3.19)$$

where, $z = \left(\frac{\partial^2 f}{\partial r^2}\right)$

Similarly using center difference and four point backward expressions, the following expression for forth order derivative is found.

$$\left(\frac{\partial^4 f}{\partial r^4}\right)_{i,j} = \frac{1}{h^4}\begin{bmatrix} 2f(i+1,j) - 9f(i,j) + 16f(i-1,j) - 14f(i-2,j) + 6f(i-3,j) \\ -f(i-4,j) \end{bmatrix} + O\left(h^2\right) \qquad (3.20)$$

The finite difference expressions for cross derivatives can also be obtained in the similar manner. Formulas for some of the cross derivatives used in this thesis using forward and center differencing are as follows.

$$\frac{\partial^2 f}{\partial r \partial \theta} = \frac{1}{4hk}[-f(i+1,j+2) + 4f(i+1,j+1) - 3f(i+1,j) + f(i-1,j+2) - 4f(i-1,j+1) + 3f(i-1,j)] + O\left(h^2\right) \qquad (3.21)$$

$$\frac{\partial^3 f}{\partial r^2 \partial \theta} = \frac{1}{2h^2 k}[f(i+2,j+1) - f(i+2,j-1) - 2f(i+1,j+1) + 2f(i+1,j-1) + f(i,j+1) - f(i,j-1)] + O\left(h^2\right) \qquad (3.22)$$

$$\frac{\partial^3 f}{\partial r \partial \theta^2} = \frac{1}{2hk^2}[-f(i+2,j+1) + 2f(i+2,j) - f(i+2,j-1) + 4f(i+1,j+1) - 8f(i+1,j) + 4f(i+1,j-1) - 3f(i,j+1) + 6f(i,j) - 3f(i,j-1)] + O\left(h^2\right) \qquad (3.23)$$

With these finite difference formulae, the differential equation and the boundary conditions can be expressed into their respective analogs of finite difference equations.

## 3.3 SCHEME OF FINITE DIFFERENCE MODELING

According to the usual practice, the region in which the dependent function is to be evaluated is divided into a desirable number of mesh points and the values of the function are sought only at these mesh points. The division into mesh points can be done in any regular or irregular manner, but considering the fact of solving the problem by a computer, regularity is highly desirable. Even the regularity will have different patterns and, therefore, the question is to choose a particular pattern which will serve the purpose in the best possible way. Unquestionably, for simplicity, especially where curve boundaries are concerned, the choice is that of regular curvilinear mesh points. Having decided upon the pattern and the total number of mesh points a sufficient number of equations must be provided to solve for all the "discretized variables" (the values of the function at the mesh points) resulting from the division of the domain into mesh points.

It is realized that the governing partial differential equation [Eq. 2.17] in terms of $\psi$ when applied to a nodal point will give rise to a single algebraic equation and therefore, the single unknown concerning this point has been provided with a single equation for its evaluation. Further, this algebraic equation will contain the discretized variable of the thirteen neighboring mesh points including 0 marked from 1 to 12 in Fig. (3.2), provided all the derivatives present in the governing equation are replaced by their respective central difference formulae. This implies that, when 0 becomes an immediate neighbor to the boundary mesh points, this equation will contain mesh points exterior to the physical boundary as well as on the boundary itself. Thus, it is seen that if the discretization of the domain concerned is performed in a fashion as shown in Fig (3.2), the application of the finite difference formulae of the governing differential equation imposes limitation to the points in the immediate neighborhood of the boundary mesh points. Again, as far as the boundary conditions are concerned, the boundary conditions in terms of stress and displacement components contain $2^{nd}$ and $3^{rd}$ order derivatives of $\psi$ and the application of the boundary conditions to an arbitrary nodal point on the boundary would be very difficult without the involvement of mesh points exterior to the physical boundary. There are always

two conditions to be satisfied at an arbitrary point on the boundary and these two conditions are theoretically sufficient to obtain the two equations at this point. In this respect, if the boundary conditions are given either in terms of displacement or stress components, that is, in the form of differential equations of unknown function, these differential equations have to be expressed into difference equations.

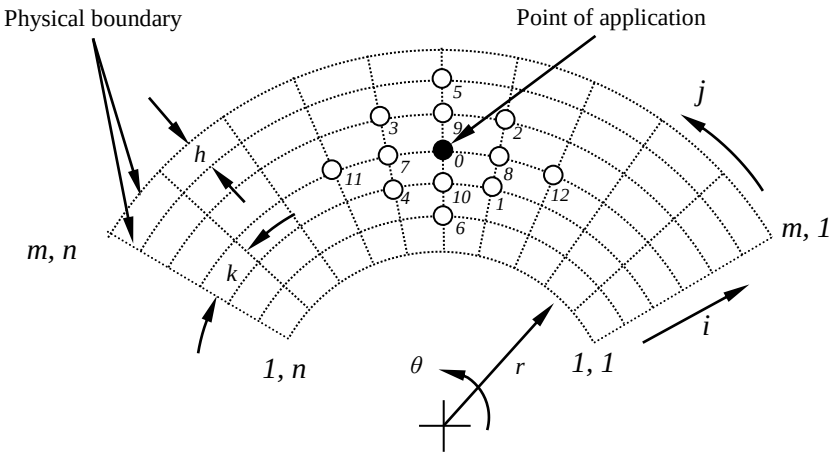


**Figure 3.2:** Finite difference discretization of the governing differential equation.

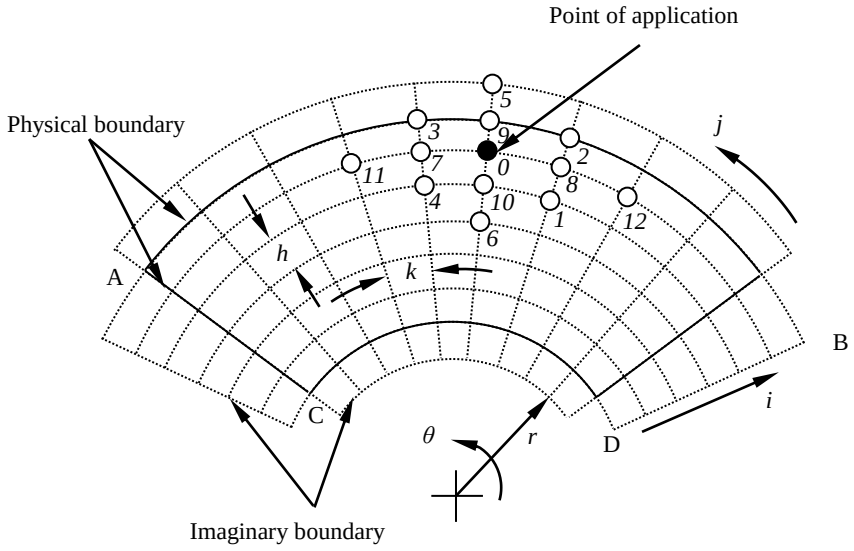


**Figure 3.3:** Involvement of imaginary nodal points while applying governing equation to a point immediate neighborhood of the physical boundary mesh point.

One way of avoiding these difficulties is to consider an imaginary boundary exterior to the physical boundary of the domain concerned. With this imaginary boundary, the application of the central difference expressions of the governing equation to the points in the immediate neighborhood to the physical boundary will cause no problem to the discretization of the domain as it will involve no points exterior to the imaginary boundary. The new discretization of the domain with the imaginary boundary mesh points is illustrated in Fig. (3.3) which illustrate the application of the central difference stencil of the governing equation to an arbitrary point in the immediate neighborhood of the physical boundary.

The same sort of problem can be raised when the finite difference expressions the boundary conditions are applied to the boundary mesh points. As the differential equations associated with the boundary conditions contain second and third order derivatives of function $\psi$, the application of the central difference expression will not be practical as, most of the time, it may lead to the inclusion of points exterior to the imaginary boundary. One of the ways to manage the situation is to replace all the first order derivatives of the function present in the boundary conditions by their two-point forward or backward difference formulae. The use of forward or backward difference formulae is dictated by the position of the mesh point on the boundary in order to avoid the occurrence of involving the mesh points external to the imaginary boundary. But the local truncation error of this approach would be of order h. A second way is to replace the above mentioned derivatives in the boundary conditions by three point forward or backward difference formulae. Local truncation error of this approach is of order $h^2$. Theoretically, there is no difficulty in using either one of the two methods in obtaining the finite difference expressions on the boundary. In this thesis, both of these approaches have been investigated and compared to obtain the effect of local truncation error on the solution.

Since there are always two conditions to be satisfied at an arbitrary point on the physical boundary of the domain, the finite difference expressions of the differential equations associated with the two boundary conditions will be applied to the same point on the boundary. It will lead to the fact that two linear algebraic equations will be assigned for a single point on the boundary. The computer program is organized in such a fashion that out of these two equations, one will be used to evaluate the point on the physical boundary and the remaining one for the corresponding point on the imaginary boundary and so on. Thus, every mesh point of the domain will have a single algebraic equation and this system of equations is solved by either direct or indirect methods of solution. One limitation of this

approach over that of having no imaginary boundary is that this approach has to handle relatively a large number of algebraic equations than the other one. This is because, this approach takes into consideration a large number of extra mesh points associated with the imaginary boundary and the number of algebraic equation increases with the increase of mesh points.

Another problem is faced during the numerical modeling of the corner mesh points, which are in general the points of singularity. Considering D as a corner mesh point in Fig. (3.3), it is seen that D is a common point to both the edges BD and DC, and it will have four boundary conditions; two conditions coming from each edge. As there are four boundary conditions for a single corner mesh point, there must have four unknowns to be determined from these conditions. This will demand the inclusion of mesh points exterior to each of the corner points of the physical boundary. This problem can also be handled by adapting different schemes of discretization. The discretization scheme applied to the corner points with exterior mesh points are illustrated in Fig. (3.4) and indicated as A, B, C and D.

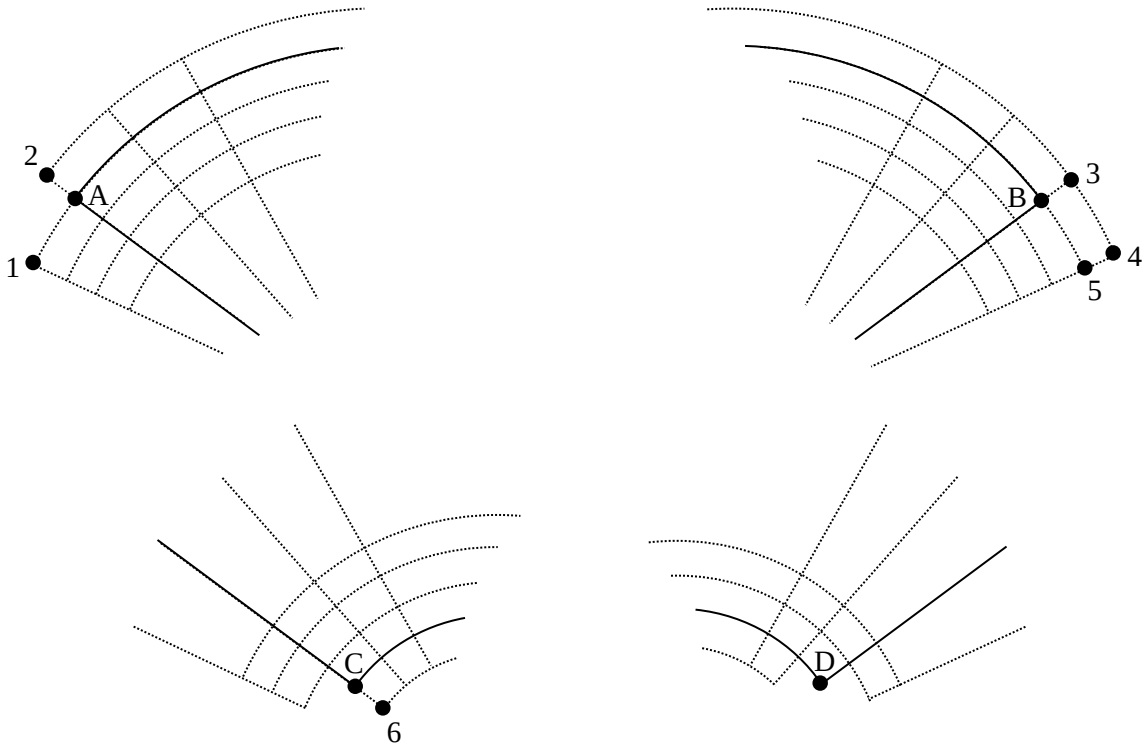


**Figure 3.4:** Corner mesh point modeling.

For the case B, in Fig. (3.4), it is seen that the unknowns at the four mesh points (3, 4, 5 and B) have to be determined from the four conditions available at point B. But in case of A, it is seen that the unknowns at three mesh points, 1, A and 2 have to be evaluated from the four conditions available at point A. Here the number of unknown is less than the number of condition to be satisfied which is theoretically impractical. One way to handle this problem is to take one of the four conditions as redundant and thus, three unknowns are determined from the remaining three boundary conditions imposed at point A. Again, for the case D, it is seen that a single unknown at mesh point D has to be evaluated from the four conditions available at D. According to the method mentioned above, this can be handled by taking a single boundary condition out of four and the remaining three conditions are left out. Lastly, for the case C, the same problem can be avoided by taking only two boundary conditions out of the four and thus the problem is reduced to the evaluation of two unknowns at mesh points (C and 6) from two conditions available at point C. All of these four approaches were investigated by Ahmed [48] over a rectangular mesh network in Cartesian coordinate system. But all the approaches were found to fail to produce any satisfactory results for various combinations of boundary conditions except that proposed in the case A in Fig. (3.4). Thus, in this thesis, the author used the approach illustrated at A for the corner mesh points as it is capable to produce promising results.

From algebra it is known that two common methods of solving simultaneous equations are: the direct method of elimination and the method of iteration. In iterative solution, one assumes an arbitrary initial approximation to the solution and then improves this approximation according to a iterative algorithm. When the system of equations to be solved is quite large, where a number of equations of the system have identical coefficients, and where the number of unknowns present in individual equation is quite small, the choice of iterative method is imperative. But the problem of solving the difference equations by this method presents serious difficulty. Though the iterative method of solving the resulting algebraic equations produced promising results for certain boundary conditions, it fails completely to produce any solution for other boundary conditions. In certain cases the rate of convergence of iteration was extremely slow which made it impractical. Since this iterative method has the limitation of not always converging to a solution and sometimes converging but very slowly, the author thus finally decided to use the direct method of solution. The direct method of elimination used here is known as “LU decomposition” method. In this method the matrix of coefficients is transformed into product of two matrices L and U, where

L is a lower-triangular matrix and U is an upper-triangular matrix with ones on its diagonal. This method requires fewer arithmetic operations on computer than either Gaussian or Gauss-Jordan methods or matrix inversion method, and hence higher accuracy can be achieved. This method may also be made economical in terms of storage in computer by overlaying the U and L matrices on the coefficient matrix A (in the same storage location). This may be done since there is no need to store the zeroes and ones of the U and L matrices.

## 3.4 FINITE DIFFERENCE EQUATIONS

Fig. (3.5) shows a general stencil at an internal mesh point, where the locations of the mesh points are designated by double subscripts. The distances between pivotal points are *h* and *k* in *r*- and $\theta$- direction respectively and they are assumed to be constants all over the computational domain.

Referring to Fig. (3.5), the difference approximation corresponding to the governing equation (2.17), namely,

$$\frac{\partial^4\psi}{\partial r^4}+\frac{1}{r^4}\frac{\partial^4\psi}{\partial\theta^4}+\frac{2}{r^2}\frac{\partial^4\psi}{\partial r^2\partial\theta^2}-\frac{2}{r}\frac{\partial^3\psi}{\partial r^3}-\frac{6}{r^3}\frac{\partial^3\psi}{\partial r\partial\theta^2}+\frac{5}{r^2}\frac{\partial^2\psi}{\partial r^2}+\frac{10}{r^4}\frac{\partial^2\psi}{\partial\theta^2}-\frac{9}{r^3}\frac{\partial\psi}{\partial r}+\frac{9}{r^4}\psi=0$$

at a general mesh point (i, j) can be obtained by replacing the derivatives with their center difference formulae. Assuming $\psi$ to be the continuous function at different mesh points, the equation in its difference form becomes,

$$\begin{aligned}&\xi_1\psi(i+2,j)+\xi_2\psi(i+1,j+1)+\xi_3\psi(i+1,j)+\xi_2\psi(i+1,j-1)+\xi_4\psi(i,j+2)+\xi_5\psi(i,j+1)\\&+\xi_6\psi(i,j)+\xi_5\psi(i,j-1)+\xi_4\psi(i,j-2)+\xi_7\psi(i-1,j+1)+\xi_8\psi(i-1,j)+\xi_7\psi(i-1,j-1)\\&+\xi_9\psi(i-2,j)=0\end{aligned}\qquad(3.21)$$

where, the coefficients $\xi_i$ are as follows:

$$\xi_1 = r_i^3 k^4 (r_i - h)$$
$$\xi_2 = r_i h^2 k^2 (2r_i - 3h)$$
$$\xi_3 = r_i k^2 (-4r_i^3 k^2 - 4r_i h^2 + 2r_i^2 hk^2 + 6h^3 + 5r_i h^2 k^2 - \frac{9}{2} h^3 k^2)$$
$$\xi_4 = h^4$$
$$\xi_5 = 2h^2 (-2r_i^2 k^2 - 2h^2 + 5h^2 k^2)$$
$$\xi_6 = 6r_i^4 k^4 + 8r_i^2 h^2 k^2 + 6h^4 - 10r_i^2 h^2 k^4 - 20h^4 k^2 + 9h^4 k^4$$
$$\xi_7 = r_i h^2 k^2 (2r_i + 3h)$$
$$\xi_8 = r_i k^2 (-4r_i^3 k^2 - 4r_i h^2 - 2r_i^2 hk^2 - 6h^3 + 5r_i h^2 k^2 + \frac{9}{2} h^3 k^2)$$
$$\xi_9 = r_i^3 k^4 (r_i + h)$$

$h, k$ = mesh lengths in $r$ – and $\theta$ – directions, respectively ($h = \Delta r, k = \Delta\theta$)

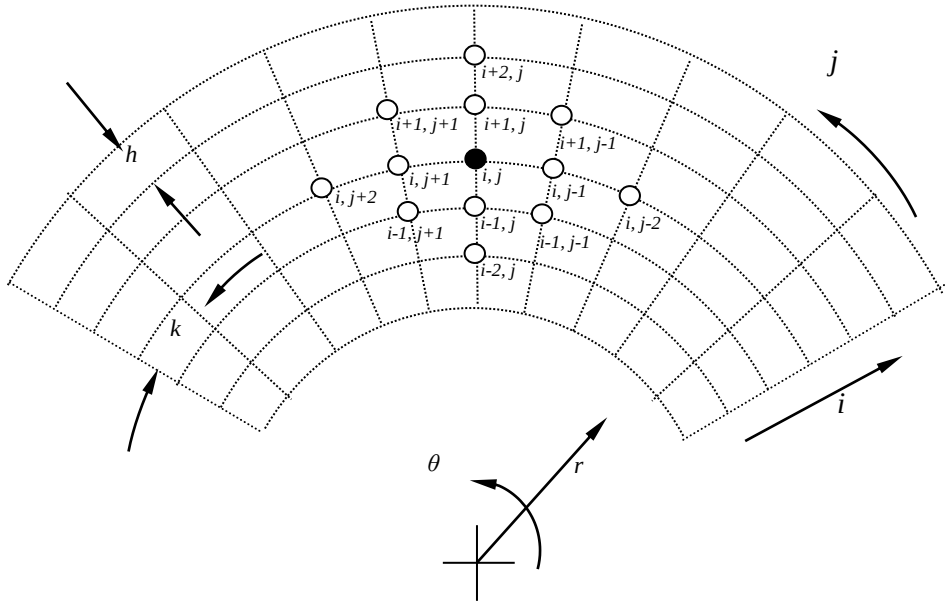


**Figure 3.5:** Finite-difference stencils of an arbitrary differential equation in curvilinear mesh-network.

Therefore Eqn. (3.21) is the difference approximation to the governing partial differential equation (2.11) and valid for all the internal mesh points except for that on boundaries.

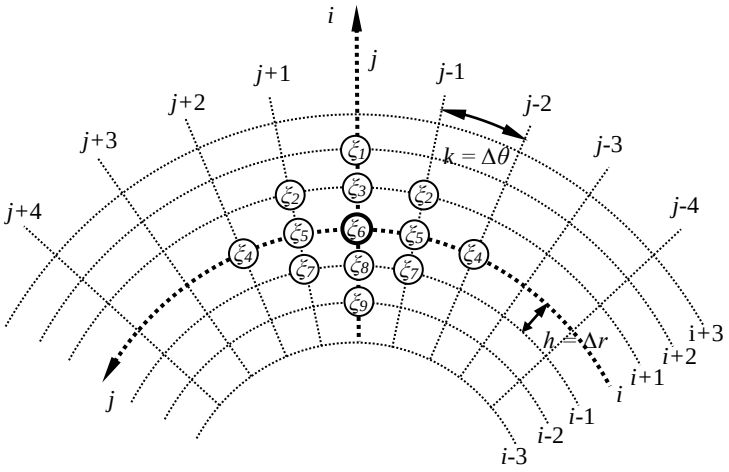


(a)

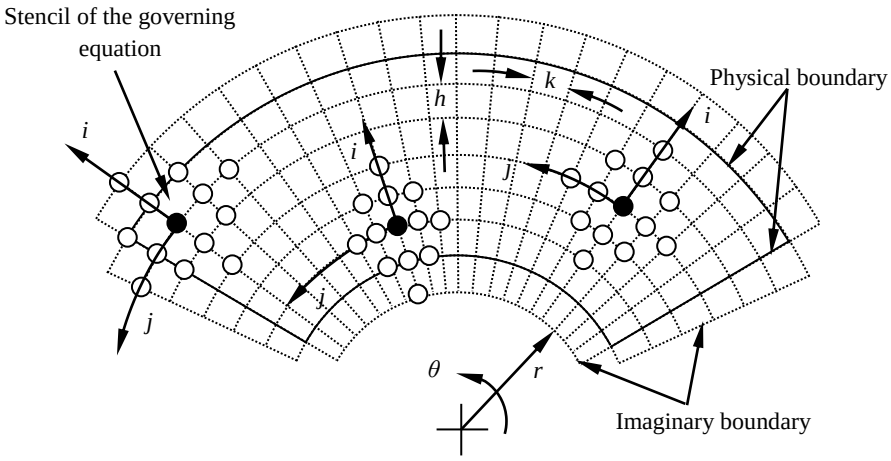


(b)

**Figure 3.6:** Finite-difference stencil of governing equation and its application at different locations of the discretized body.

Fig. 3.6(a) shows the finite difference stencil of the governing equation [Eq. 2.17]. Fig. 3.6 (b) shows the application of the governing differential equation at different regions of the discretized body. It can be seen that for any interior mesh point stencil never include any point beyond the imaginary boundary.

### 3.4.1 Finite difference expressions for different displacement and stress components according to the Formulation-I

As the differential equations associated with the boundary conditions contain second- and third-order partial derivatives of the function $\psi$, the use of central difference expressions eventually leads to the inclusion of points exterior to the imaginary boundary. In order to avoid the occurrence, different versions of the finite-difference expressions like forward, backward and central difference have been adopted in a combined form to generate the difference equations for the boundary conditions. It is noted here that the order of local truncation error has been kept the same for all the expressions developed, that is, O($h^2$). As previously mentioned, though the expressions of the governing equation obtained from both the formulations (Formulation-I and Formulation-II) are same, the expressions of stress and displacement components obtained from different formulations are different. As a result, the numerical modeling for the two formulations will be different. Finite-difference expressions for different displacement and stress components corresponding to Formulation-I and Formulation- II are discussed below.

**(a) Formulation-I**

For the radial component of displacement Eq. (2.16), four different versions of finite-difference expression have been developed for different regions of the boundary. These versions of finite difference expressions are obtained by adapting different combinations of forward and backward differencing scheme in both $r$ and $\theta$- directions . The finite-difference expressions so obtained are as follows:

a) $i$- forward, $j$- forward

$$\begin{aligned} u_r = {} & a_1\psi(i+2,j+2) - 4a_1\psi(i+2,j+1) + 3a_1\psi(i+2,j) - 4a_1\psi(i+1,j+2) \\ & + 16a_1\psi(i+1,j+1) - 12a_1\psi(i+1,j) + (3a_1 - b_1)\psi(i,j+2) - (12a_1 - 4b_1)\psi(i,j+1) \\ & + (9a_1 - 3b_1)\psi(i,j) \end{aligned} \tag{3.22}$$

b) $i$- forward, $j$- backward

$$\begin{aligned} u_r = {} & -3a_1\psi(i+2,j) + 4a_1\psi(i+2,j-1) - a_1\psi(i+2,j-2) + 12a_1\psi(i+1,j) \\ & - 16a_1\psi(i+1,j-1) + 4a_1\psi(i+1,j-2) - (9a_1 - 3b_1)\psi(i,j) + (12a_1 - 4b_1)\psi(i,j-1) \\ & - (3a_1 - b_1)\psi(i,j-2) \end{aligned} \tag{3.23}$$

c) $i$- backward, $j$- forward

$$
\begin{aligned}
u_r = &-(3a_1 + b_1)\psi(i, j+2) + (12a_1 + 4b_1)\psi(i, j+1) - (9a_1 + 3b_1)\psi(i, j) \\
&+ 4a_1\psi(i-1, j+2) - 16a_1\psi(i-1, j+1) + 12a_1\psi(i-1, j) - a_1\psi(i-2, j+2) \\
&+ 4a_1\psi(i-2, j+1) - 3a_1\psi(i-2, j)
\end{aligned} \tag{3.24}
$$

d) *i*- backward, *j*- backward

$$
\begin{aligned}
u_r = &(9a_1 + 3b_1)\psi(i, j) - (12a_1 + 4b_1)\psi(i, j-1) + (3a_1 + b_1)\psi(i, j-2) - 12a_1\psi(i-1, j) \\
&+ 16a_1\psi(i-1, j-1) - 4a_1\psi(i-1, j-2) + 3a_1\psi(i-2, j) - 4a_1\psi(i-2, j-1) \\
&+ a_1\psi(i-2, j-2)
\end{aligned} \tag{3.25}
$$

where,

$$a_1 = -\frac{1+\nu}{8r_i hk},\ b_1 = \frac{5+\nu}{4r_i^2 k}$$

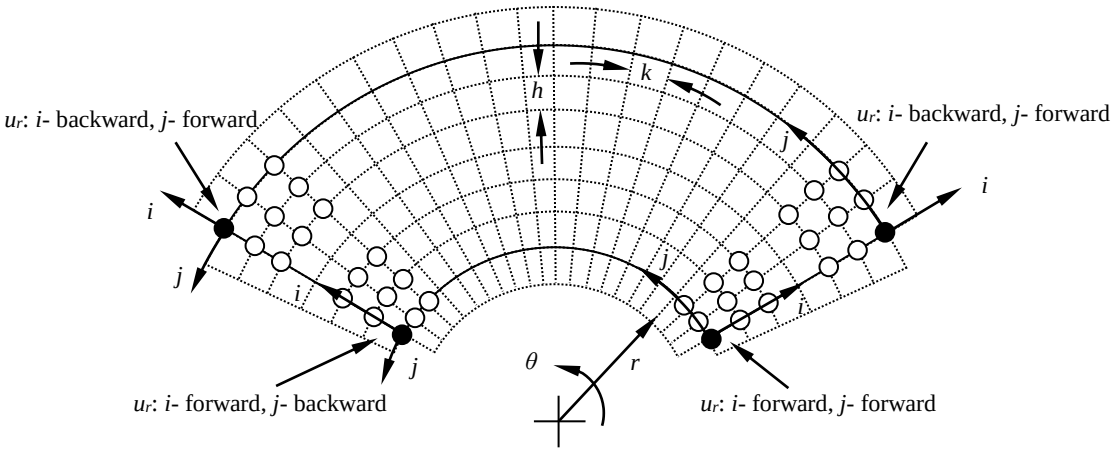


**Figure 3.7:** Finite difference stencils for radial component of displacement ($u_r$) (Formulation-I).

Figure 3.7 illustrates the above mentioned four stencils for normal component of displacement ($u_r$). It can be seen that each stencil consists of nine nodal points and when applied to the boundary mesh points as shown in the figure includes no point exterior to the physical boundary.

For tangential component of displacement, $u_\theta$ given by Eq. (2.23), a single finite-difference expression has been developed using central differencing scheme. Due to the symmetry of the

expression, it can be applied to any region of the boundary without the inclusion of points exterior to the imaginary boundary as shown in Fig. 3.8. The expression is written as follows:

$$u_\theta = (a_2 + c_2)\psi(i+1, j) + b_2\psi(i, j+1) + (-2a_2 - 2b_2 + d_2)\psi(i, j) + b_2\psi(i, j-1) + (a_2 - c_2)\psi(i-1, j) \tag{3.26}$$

where,

$$a_2 = \frac{1}{h^2},\ b_2 = \frac{1-v}{2r_i^2k^2},\ c_2 = \frac{-3}{2r_ih},\ d_2 = \frac{3}{r_i^2}$$

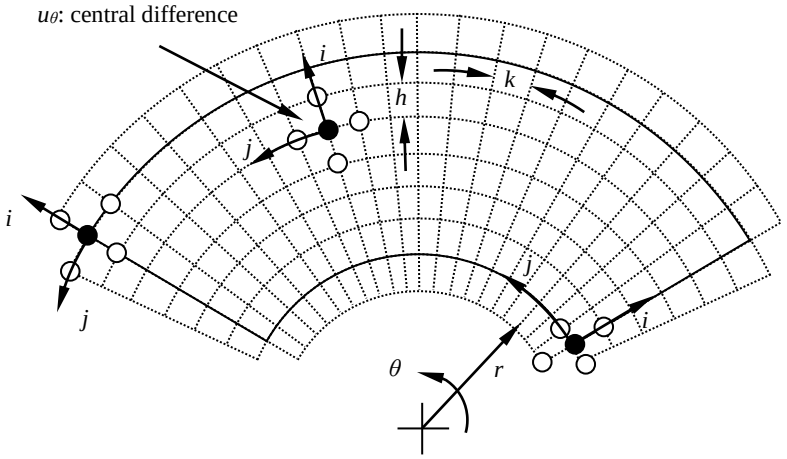


**Figure 3.8:** Finite difference stencils for tangential components of displacement ($u_\theta$) (Formulation-I).

Now, for the radial component of stress which is given by Eq. (2.14), two different finite-difference expressions has been developed using the combination of central, forward and backward differencing scheme which are illustrated in Fig. 3.9. Since the stencils have the symmetry about *j*- axis, two versions are sufficient to deal with all the body points involved. The expressions developed are:

a) *i*- central, *j*- forward

$$\begin{aligned}\sigma_r = {} & (-A_1 - C_1)\psi(i+1, j+2) + (4A_1 + 4C_1)\psi(i+1, j+1) + (-3A_1 - 3C_1)\psi(i+1, j) \\ & - B_1\psi(i, j+3) + (2A_1 + 6B_1)\psi(i, j+2) + (-8A_1 - 12B_1 + D_1)\psi(i, j+1) \\ & + (6A_1 + 10B_1)\psi(i, j) + (-3B_1 - D_1)\psi(i, j-1) + (-A_1 + C_1)\psi(i-1, j+2) \\ & + (4A_1 - 4C_1)\psi(i-1, j+1) + (-3A_1 + 3C_1)\psi(i-1, j)\end{aligned} \tag{3.27}$$

b) *i*- central, *j*- backward

$$\begin{aligned}\sigma_r = {} & (3A_1 + 3C_1)\psi(i+1, j) + (-4A_1 - 4C_1)\psi(i+1, j-1) + (A_1 + C_1)\psi(i+1, j-2) \\ & + (3B_1 + D_1)\psi(i, j+1) + (-6A_1 - 10B_1)\psi(i, j) + (8A_1 + 12B_1 - D_1)\psi(i, j-1) \\ & + (-2A_1 - 6B_1)\psi(i, j-2) + B_1\psi(i, j-3) + (3A_1 - 3C_1)\psi(i-1, j) \\ & + (-4A_1 + 4C_1)\psi(i-1, j-1) + (A_1 - C_1)\psi(i-1, j-2)\end{aligned} \tag{3.28}$$

where,

$$A_1 = -\frac{G}{2r_i h^2 k},\ B_1 = \frac{vG}{2r_i^3 k^3},\ C_1 = \frac{(6+v)G}{4r_i^2 hk},\ D_1 = -\frac{(10+v)G}{2r_i^3 k}$$

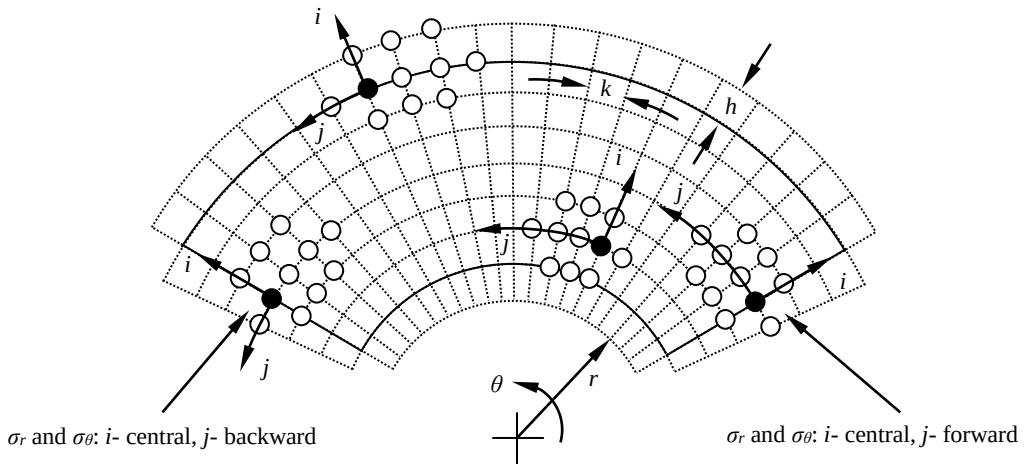


**Figure 3.9:** Finite difference stencils for radial and tangential components ($\sigma_r$, $\sigma_\theta$) of stress (Formulation-I)

The corresponding finite difference expressions for $\sigma_\theta$ which is given by Eq. (2.25) are developed following a procedure similar to that used for the case of $\sigma_r$, as the two differential equations are identical in terms of derivatives, but the differ only in terms of the coefficients. As a result, the finite difference stencils of $\sigma_r$ and $\sigma_\theta$ become identical in their appearance as shown in Fig. 3.9. The finite difference equations developed for $\sigma_\theta$ are as follows:

a) *i*-central, *j*- forward

$$\begin{aligned}\sigma_\theta = {} & (-A_2 - C_2)\psi(i+1, j+2) + (4A_2 + 4C_2)\psi(i+1, j+1) + (-3A_2 - 3C_2)\psi(i+1, j) \\ & - B_2\psi(i, j+3) + (2A_2 + 6B_2)\psi(i, j+2) + (-8A_2 - 12B_2 + D_2)\psi(i, j+1) \\ & + (6A_2 + 10B_2)\psi(i, j) + (-3B_2 - D_2)\psi(i, j-1) + (-A_2 + C_2)\psi(i-1, j+2) \\ & + (4A_2 - 4C_2)\psi(i-1, j+1) + (-3A_2 + 3C_2)\psi(i-1, j)\end{aligned} \tag{3.29}$$

b) *i*- central, *j*- backward

$$\begin{aligned}\sigma_\theta = {} & (3A_2 + 3C_2)\psi(i+1, j) + (-4A_2 - 4C_2)\psi(i+1, j-1) + (A_2 + C_2)\psi(i+1, j-2) \\ & + (3B_2 + D_2)\psi(i, j+1) + (-6A_2 - 10B_2)\psi(i, j) + (8A_2 + 12B_2 - D_2)\psi(i, j-1) \\ & + (-2A_2 - 6B_2)\psi(i, j-2) + B_2\psi(i, j-3) + (3A_2 - 3C_2)\psi(i-1, j) \\ & + (-4A_2 + 4C_2)\psi(i-1, j-1) + (A_2 - C_2)\psi(i-1, j-2)\end{aligned} \tag{3.30}$$

where,

$$A_2 = \frac{G(2+\nu)}{2r_i h^2 k},\ B_2 = \frac{G}{2r_i^3 k^3},\ C_2 = -\frac{(7+2\nu)G}{4r_i^2 hk},\ D_2 = \frac{(11+2\nu)G}{2r_i^3 k}$$

Again, for the shear stress component which is given by Eq. (2.26), two different finite-difference expressions have been developed using the combination of central, forward and backward differencing scheme. Since the stencils have the symmetry about *i*- axis, two versions are sufficient to deal with all the body points involved and are illustrated in Fig. 3.10. The expressions developed are:

a) *i*-forward, *j*-central

$$\begin{aligned}\tau_{r\theta} = {} & -A_3\psi(i+3, j) - B_3\psi(i+2, j+1) + (6A_3 + 2B_3)\psi(i+2, j) - B_3\psi(i+2, j-1) \\ & + 4B_3\psi(i+1, j+1) + (-12A_3 - 8B_3 + C_3 + E_3)\psi(i+1, j) + 4B_3\psi(i+1, j-1) \\ & + (-3B_3 + D_3)\psi(i, j+1) + (10A_3 + 6B_3 - 2C_3 - 2D_3 + F_3)\psi(i, j) \\ & + (-3B_3 + D_3)\psi(i, j-1) + (-3A_3 + C_3 - E_3)\psi(i-1, j)\end{aligned} \tag{3.31}$$

b) *i*- backward, *j*- central

$$\begin{aligned}\tau_{r\theta} = {} & (3A_3 + C_3 + E_3)\psi(i+1, j) + (3B_3 + D_3)\psi(i, j+1) + (-10A_3 - 6B_3 - 2C_3 - 2D_3 + F_3) \\ & \psi(i, j) + (3B_3 + D_3)\psi(i, j-1) - 4B_3\psi(i-1, j+1) + (12A_3 + 8B_3 + C_3 - E_3)\psi(i-1, j) \\ & - 4B_3\psi(i-1, j-1) + B_3\psi(i-2, j+1) - (6A_3 + 2B_3)\psi(i-2, j) + B_3\psi(i-2, j-1) \\ & + A_3\psi(i-3, j)\end{aligned} \tag{3.32}$$

where,

$$A_3 = \frac{G}{2h^3},\ B_3 = \frac{-\nu G}{2r_i^2 hk^2},\ C_3 = -\frac{4G}{r_i h^2},\ D_3 = \frac{(1+2\nu)G}{r_i^3 k^2},\ E_3 = \frac{9G}{2r_i^2 h},\ F_3 = -\frac{9G}{r_i^3}$$

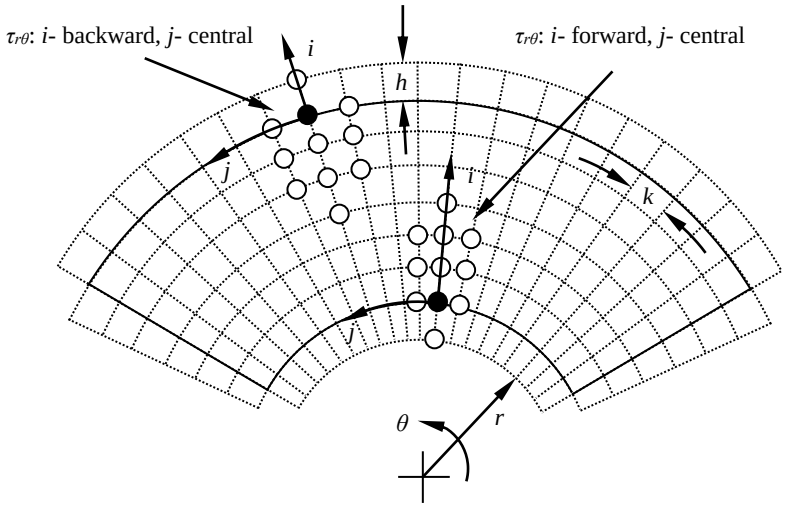


**Figure 3.10:** Finite difference stencils for shear stress component ($\tau_{r\theta}$) (Formulation-I)

**(b) Formulation-II**

For radial component of displacement, $u_r$ given by Eq. (2.27), a single finite-difference expression has been developed using central differencing scheme. Due to the symmetry of the expression, it can be applied to any region of the boundary without the inclusion of points exterior to the imaginary boundary as shown in figure 3.11. The expression is written as follows:

$$u_r = (a_1 + c_1)\psi(i+1, j) + b_1\psi(i, j+1) + (-2a_1 - 2b_1 + d_1)\psi(i, j) + b_1\psi(i, j-1) + (a_1 - c_1)\psi(i-1, j) \tag{3.33}$$

where,

$$a_1 = -\frac{1-v}{(1-3v)h^2},\ b_1 = \frac{-2}{(1-3v)r_i^2k^2},\ c_1 = \frac{3(1-v)}{2(1-3v)r_ih},\ d_1 = \frac{-3(1-v)}{(1-3v)r_i^2}$$

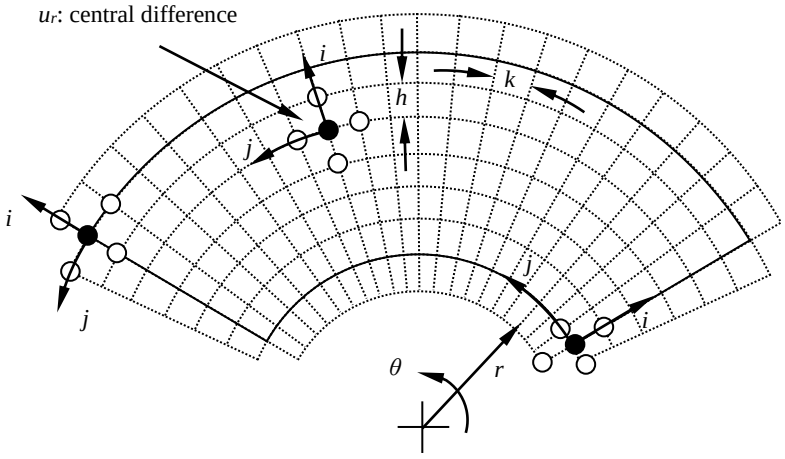


**Figure 3.11:** Finite difference stencils for radial component of displacement ($u_r$) (Formulation-II).

For the tangential component of displacement Eq. (2.28), four different versions of finite-difference expression have been developed for different regions of the boundary. These versions of finite difference expressions are obtained by adapting different combinations of forward and backward differencing scheme in both $r$ and $\theta$- directions and are illustrated in figure 3.12. The finite-difference expressions so obtained are as follows:

a) $i$- forward, $j$- forward

$$\begin{aligned} u_\theta = {} & a_2\psi(i+2,j+2) - 4a_2\psi(i+2,j+1) + 3a_2\psi(i+2,j) - 4a_2\psi(i+1,j+2) \\ & + 16a_2\psi(i+1,j+1) - 12a_2\psi(i+1,j) + (3a_2 - b_2)\psi(i,j+2) \\ & - (12a_2 - 4b_2)\psi(i,j+1) + (9a_2 - 3b_2)\psi(i,j) \end{aligned} \tag{3.34}$$

b) $i$- forward, $j$- backward

$$\begin{aligned} u_\theta = {} & -3a_2\psi(i+2,j) + 4a_2\psi(i+2,j-1) - a_2\psi(i+2,j-2) + 12a_2\psi(i+1,j) \\ & - 16a_2\psi(i+1,j-1) + 4a_2\psi(i+1,j-2) - (9a_2 - 3b_2)\psi(i,j) \\ & + (12a_2 - 4b_2)\psi(i,j-1) - (3a_2 - b_2)\psi(i,j-2) \end{aligned} \tag{3.35}$$

c) $i$- backward, $j$- forward

$$u_\theta = -(3a_2 + b_2)\psi(i, j+2) + (12a_2 + 4b_2)\psi(i, j+1) - (9a_2 + 3b_2)\psi(i, j) + 4a_2\psi(i-1, j+2) - 16a_2\psi(i-1, j+1) + 12a_2\psi(i-1, j) - a_2\psi(i-2, j+2) + 4a_2\psi(i-2, j+1) - 3a_2\psi(i-2, j) \quad (3.36)$$

d) *i*- backward, *j*- backward

$$u_\theta = (9a_2 + 3b_2)\psi(i, j) - (12a_2 + 4b_2)\psi(i, j-1) + (3a_2 + b_2)\psi(i, j-2) - 12a_2\psi(i-1, j) + 16a_2\psi(i-1, j-1) - 4a_2\psi(i-1, j-2) + 3a_2\psi(i-2, j) - 4a_2\psi(i-2, j-1) + a_2\psi(i-2, j-2) \quad (3.37)$$

where,

$$a_2 = \frac{1+v}{4(1-3v)r_i hk},\ b_2 = \frac{1}{2r_i^2 k}$$

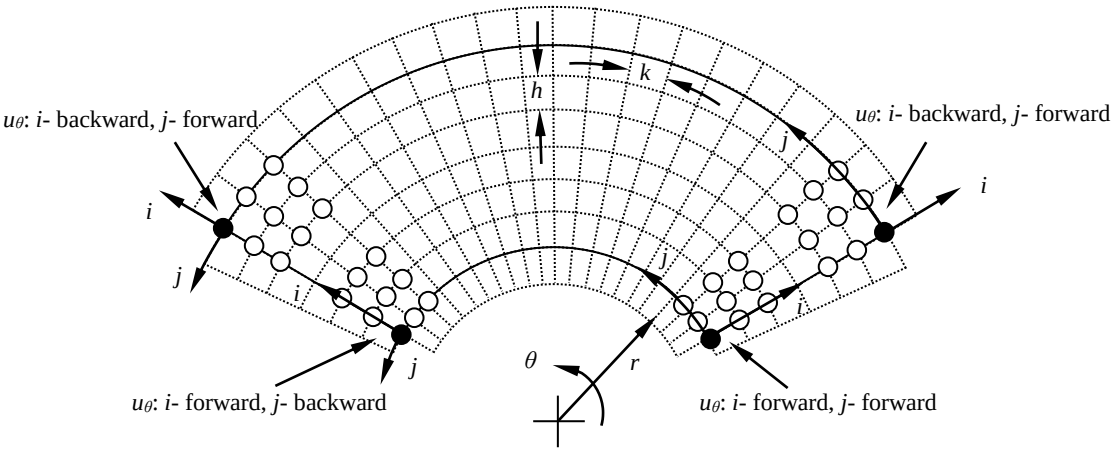


**Figure 3.12:** Finite difference stencils for tangential component of displacement ($u_\theta$) (Formulation-II).

For the radial stress component which is given by Eq. (2.29), two different finite-difference expressions have been developed using the combination of central, forward and backward differencing scheme. Since the stencils have the symmetry about *i*- axis, two versions are sufficient to deal with all the body points involved which are illustrated in figure 3.13. The expressions developed are:

a) *i*- forward, *j*- central

$$\sigma_r = -A_1\psi(i+3,j) - B_1\psi(i+2,j+1) + (6A_1 + 2B_1)\psi(i+2,j) - B_1\psi(i+2,j-1) + 4B_1 \psi(i+1,j+1) + (-12A_1 - 8B_1 + C_1 + E_1)\psi(i+1,j) + 4B_1\psi(i+1,j-1) + (-3B_1 + D_1) \psi(i,j+1) + (10A_1 + 6B_1 - 2C_1 - 2D_1 + F_1)\psi(i,j) + (-3B_1 + D_1)\psi(i,j-1) + (-3A_1 + C_1 - E_1)\psi(i-1,j) \quad (3.38)$$

b) *i*- backward, *j*- central

$$\sigma_r = (3A_1 + C_1 + E_1)\psi(i+1,j) + (3B_1 + D_1)\psi(i,j+1) + (-10A_1 - 6B_1 - 2C_1 - 2D_1 + F_1) \psi(i,j) + (3B_1 + D_1)\psi(i,j-1) - 4B_1\psi(i-1,j+1) + (12A_1 + 8B_1 + C_1 - E_1)\psi(i-1,j) - 4B_1\psi(i-1,j-1) + B_1\psi(i-2,j+1) - (6A_1 + 2B_1)\psi(i-2,j) + B_1\psi(i-2,j-1) + A_1\psi(i-3,j) \quad (3.39)$$

where,

$$A_1 = -\frac{G}{(1-3\nu)h^3},\ B_1 = -\frac{(2+\nu)G}{(1-3\nu)r_i^2hk^2},\ C_1 = \frac{2(3-\nu)G}{(1-3\nu)r_ih^2},\ D_1 = \frac{2(4+3\nu)G}{(1-3\nu)r_i^3k^2},\ E_1 = -\frac{3(2-\nu)G}{(1-3\nu)r_i^2h}$$

, $F_1 = \frac{6(2-\nu)G}{(1-3\nu)r_i^3}$

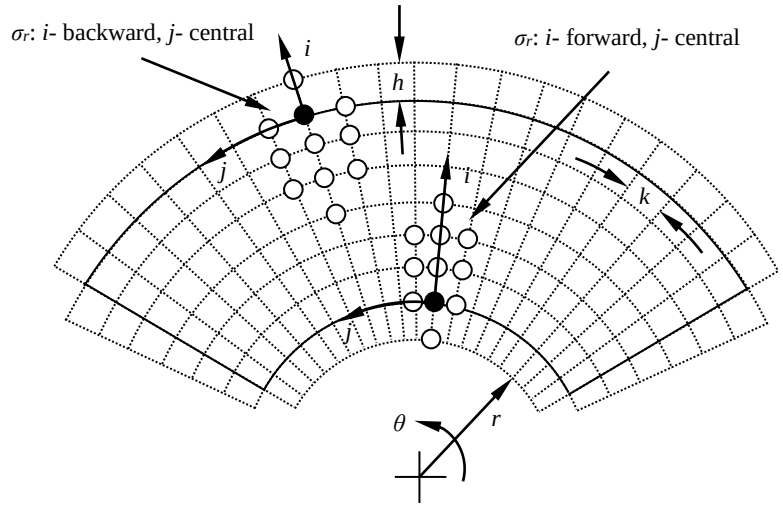


**Figure 3.13:** Finite difference stencils for radial and tangential components ($\sigma_r$, $\sigma_\theta$) of stress (Formulation-II)

The corresponding finite difference expressions for $\sigma_\theta$ which is given by Eq. (2.30) are developed following a procedure similar to that used for the case of $\sigma_r$, as the two differential equations are identical in terms of derivatives, but the differ only in terms of the coefficients. As a result, the finite difference stencils of $\sigma_r$ and $\sigma_\theta$ become identical in their appearances too. The finite difference equations developed for $\sigma_\theta$ are as follows:

a) *i*- forward, *j*- central

$$\begin{aligned}\sigma_\theta = &-A_2\psi(i+3,j) - B_2\psi(i+2,j+1) + (6A_2+2B_2)\psi(i+2,j) - B_2\psi(i+2,j-1)\\ &+4B_2\psi(i+1,j+1) + (-12A_2-8B_2+C_2+E_2)\psi(i+1,j) + 4B_2\psi(i+1,j-1)\\ &+(-3B_2+D_2)\psi(i,j+1) + (10A_2+6B_2-2C_2-2D_2+F_2)\psi(i,j)\\ &+(-3B_2+D_2)\psi(i,j-1) + (-3A_2+C_2-E_2)\psi(i-1,j)\end{aligned} \tag{3.40}$$

b) *i*- backward, *j*- central

$$\begin{aligned}\sigma_\theta = &(3A_2+C_2+E_2)\psi(i+1,j) + (3B_2+D_2)\psi(i,j+1)\\ &+(-10A_2-6B_2-2C_2-2D_2+F_2)\psi(i,j) + (3B_2+D_2)\psi(i,j-1) - 4B_2\psi(i-1,j+1)\\ &+(12A_2+8B_2+C_2-E_2)\psi(i-1,j) - 4B_2\psi(i-1,j-1) + B_2\psi(i-2,j+1)\\ &-(6A_2+2B_2)\psi(i-2,j) + B_2\psi(i-2,j-1) + A_2\psi(i-3,j)\end{aligned} \tag{3.41}$$

where,

$$A_2 = -\frac{Gv}{(1-3v)h^3}\ ,\quad B_2 = \frac{G}{(1-3v)r_i^2hk^2}\ ,\quad C_2 = \frac{2G}{r_ih^2}\ ,\quad D_2 = -\frac{2G}{(1-3v)r_i^3k^2}\ ,\quad E_2 = -\frac{3(1-2v)G}{(1-3v)r_i^2h}\ ,$$

$$F_2 = -\frac{6(1-2v)G}{(1-3v)r_i^3}$$

Now, for the shear stress component which is given by Eq. (2.31), two different finite-difference expressions has been developed using the combination of central, forward and backward differencing scheme which are illustrated in Fig. 3.14. Since the stencils have the symmetry about *j*- axis, two versions are sufficient to deal with all the body points involved. The expressions developed are:

a) *i*- central, *j*- forward

$$\begin{aligned}\tau_{r\theta} = &(-A_3-C_3)\psi(i+1,j+2) + (4A_3+4C_3)\psi(i+1,j+1) + (-3A_3-3C_3)\psi(i+1,j)\\ &-B_3\psi(i,j+3) + (2A_3+6B_3)\psi(i,j+2) + (-8A_3-12B_3+D_3)\psi(i,j+1)\\ &+(6A_3+10B_3)\psi(i,j) + (-3B_3-D_3)\psi(i,j-1) + (-A_3+C_3)\psi(i-1,j+2)\\ &+(4A_3-4C_3)\psi(i-1,j+1) + (-3A_3+3C_3)\psi(i-1,j)\end{aligned} \tag{3.42}$$

b) *i*- central, *j*- backward

$$\begin{aligned}\tau_{r\theta} = &(3A_3+3C_3)\psi(i+1,j) + (-4A_3-4C_3)\psi(i+1,j-1) + (A_3+C_3)\psi(i+1,j-2)\\ &+(3B_3+D_3)\psi(i,j+1) + (-6A_3-10B_3)\psi(i,j) + (8A_3+12B_3-D_3)\psi(i,j-1)\\ &+(-2A_3-6B_3)\psi(i,j-2) + B_3\psi(i,j-3) + (3A_3-3C_3)\psi(i-1,j)\\ &+(-4A_3+4C_3)\psi(i-1,j-1) + (A_3-C_3)\psi(i-1,j-2)\end{aligned} \tag{3.43}$$

where,

$$A_3 = \frac{Gv}{(1-3v)r_i h^2 k},\ B_3 = -\frac{G}{(1-3v)r_i^3 k^3},\ C_3 = \frac{(1-4v)G}{2(1-3v)r_i^2 hk},\ D_3 = -\frac{3(1-2v)G}{(1-3v)r_i^3 k}$$

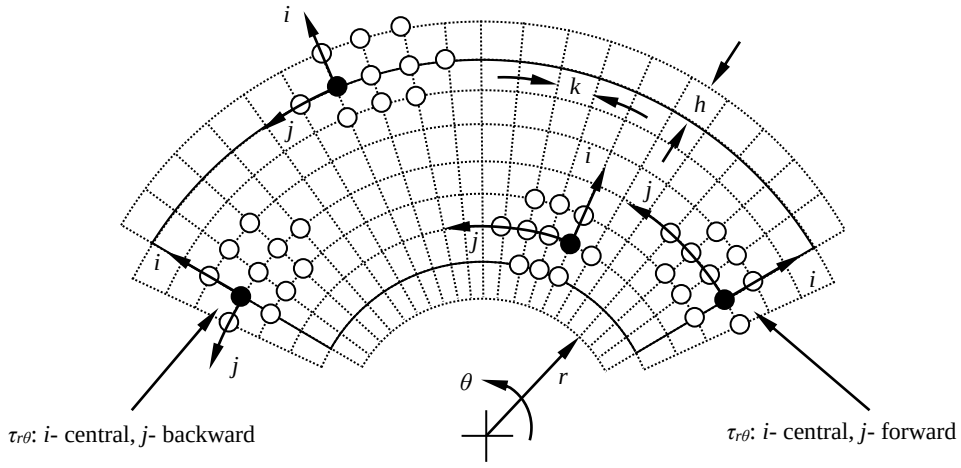


**Figure 3.14:** Finite difference stencils for shear stress component ($\tau_{r\theta}$) (Formulation-II).

Chapter 04

# VALIDATION OF DISPLACEMENT POTENTIAL METHOD

## 4.1 INTRODUCTION

This chapter is intended to verify the soundness and appropriateness of the displacement potential method developed in this study for the analysis of curved structural elements in polar coordinate system. To achieve this goal, two well known problems of stress analysis have been solved and the results are compared with the available analytical solution as well as the numerical solution. Problem-I is an example of classical stress problem, namely, thick-walled pressure vessel with outer to inner radius ratio, $r_o/ r_i = 2$, under the action of uniform internal and external pressure over its whole circumference. Problem-II is an example of curved circular beam under pure bending action. Analytical solution is available for both the problems from theory of elasticity. Finite element solution is provided for problem-I which has been obtained using commercial finite-element package ANSYS 11.0.

## 4.2 THICK-WALLED PRESSURE VESSEL

A thick-walled pressure vessel with outer to inner radius ratio, $r_o/ r_i = 2$, is considered here. The loading and geometry of the stressed body is illustrated in Fig. 4.1(a). The pressure vessel is subjected to uniform pressure at its inner and outer boundaries with the ratio of external to internal pressure, $P_o/P_i = 2$, as shown in the figure. In order to obtain results of the problem, values for Young's modulus and Poisson's ratio of 207 GPa and 0.29, respectively, are used.

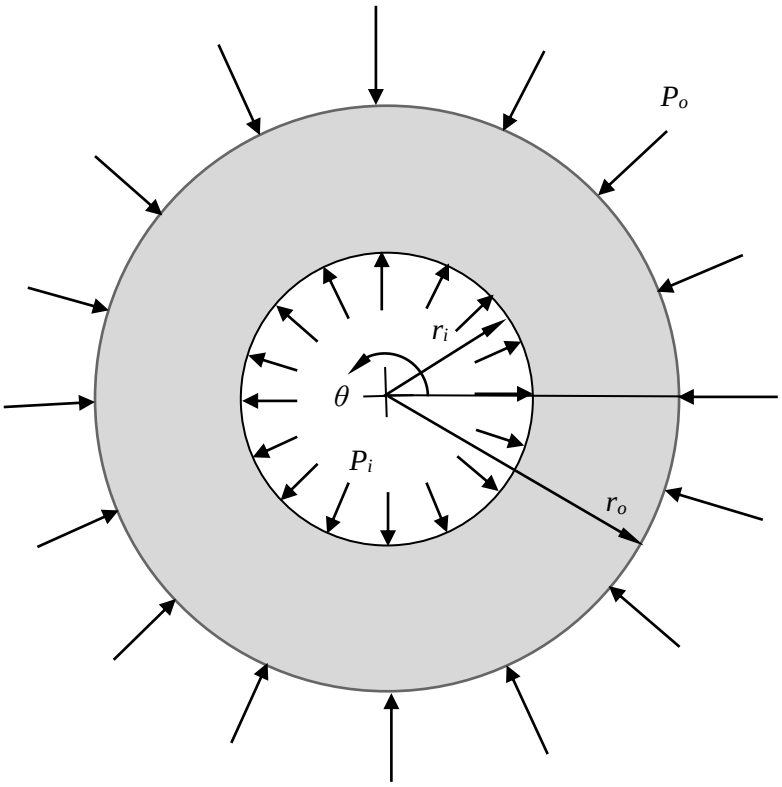


(a) Loading and geometry of pressure vessel

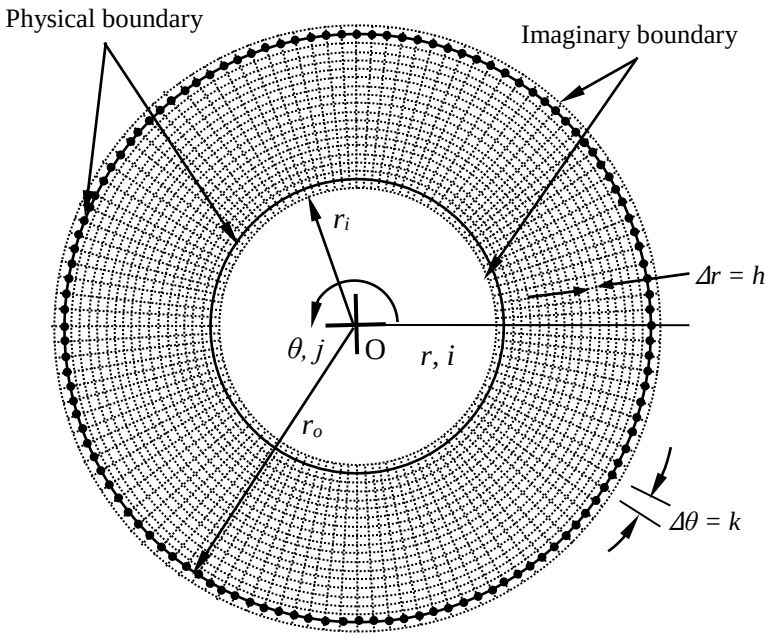


(b) Finite-difference discretization of thick-walled pressure vessel

**Figure 4.1:** Thick-walled pressure vessel under uniform radial pressure.

The finite difference mesh network used for the problem of pressure vessel is illustrated in Figure 4.1(b), in which two imaginary boundaries, interior to the inner physical boundary and

exterior to the outer physical boundary are included for the solution. The nodal points interior to the inner and exterior to the outer boundaries are, in fact, selected by the application of the governing equation to the internal nodal points at the immediate neighbor to the physical boundaries. Finite difference solution for the elastic field of the problem has been obtained using relatively small number of mesh points (31 × 43), mesh points along $r$- and $\theta$- axes, respectively. Here, the radial displacement is normalized with respect to the thickness of the vessel and stresses are normalized with respect to the intensity of the uniform external pressure, $P_o$.

The present displacement potential solutions are presented in a comparative fashion with those of the theory of elasticity as well as finite element method. The boundary conditions used to generate the displacement potential solution for the problem are listed in Table 4.1.

Table- 4.1

Modeling of boundary conditions for the thick-walled pressure vessel

| Problem | Boundary | Boundary conditions | |
|---|---|---|---|
| | | Normal component | Tangential component |
| Cylindrical Pressure vessel (Fig. 4.1) | Outer surface ($r=r_o$) | $\sigma_r(r_o, \theta)=-P_o$ | $\tau_{r\theta}(r_o, \theta)=0$ |
| | Inner surface ($r=r_i$) | $\sigma_r(r_i, \theta)=-P_i$ | $\tau_{r\theta}(r_i, \theta)=0$ |

Exact analytical solutions of displacement and stress distributions along the radial direction of the vessel are available in the literature. The stress function based elasticity solutions for the components of displacement and stress are included here as a ready reference for the interested readers [5].

$$u_r = \frac{(1-\nu)(P_i r_i^2 - P_o r_o^2) r^2 + (1+\nu) r_i^2 r_o^2 (P_i - P_o)}{Er(r_o^2 - r_i^2)} \tag{4.1}$$

$$\sigma_r = \frac{r_i^2 r_o^2 (P_o - P_i)}{r_o^2 - r_i^2} \frac{1}{r^2} + \frac{P_i r_i^2 - P_o r_o^2}{r_o^2 - r_i^2} \tag{4.2}$$

$$\sigma_\theta = -\frac{r_i^2 r_o^2 (P_o - P_i)}{r_o^2 - r_i^2}\frac{1}{r^2} + \frac{P_i r_i^2 - P_o r_o^2}{r_o^2 - r_i^2} \tag{4.3}$$

Finite element solutions of the thick-walled pressure vessel problem are also included to make the comparison more effective. The FEM solutions are obtained by using the standard facility of a commercial FEM software (ANSYS). In obtaining the FEM solutions, 8-noded quadratic plane stress elements (PLANE 183) were used to construct element mesh network for the cylindrical body in a rectangular coordinate system. The total number of nodal points used to construct the mesh network was 18362.

### 4.2.1 Comparison of solutions by different methods

Figure 4.2 shows the comparison of three solutions, namely, stress function, displacement potential method (DPM) and finite element method (FEM) solutions for the present stress problem of thick-walled pressure vessel. Figure 4.2(a) shows the distribution of radial displacement along the radial direction of the pressure vessel. The radial displacement is found to increase from inner surface to outer surface of the vessel. A comparative analysis reveals that the distribution of radial displacement obtained from three different approaches is in excellent agreement, as the results are found to be almost identical. Figure 4.2(b1) and (b2) show the comparison of corresponding solutions for the radial and tangential stress components, respectively. For both cases of stress distributions, solutions obtained from the three different approaches are also found to be almost identical. Moreover, the distribution of radial stress verifies the capability of the present displacement potential method in reproducing the boundary conditions accurately, as the normalized values of the radial stress assume values very close to -0.5 and -1.0, at the inner and outer surface of the vessel respectively. From the distributions of stress components, the circumferential (hoop) stress is identified to be the most critical stress in the pressure vessel, the value of which at the outer surface of the vessel is found to be as high as 1.83 times the applied pressure. The present comparison of the results of the cylindrical pressure vessel thus firmly establishes the soundness as well as appropriateness of the present displacement potential computational approach as the results are found to be in excellent agreement with the corresponding exact analytical as well as conventional computational results.

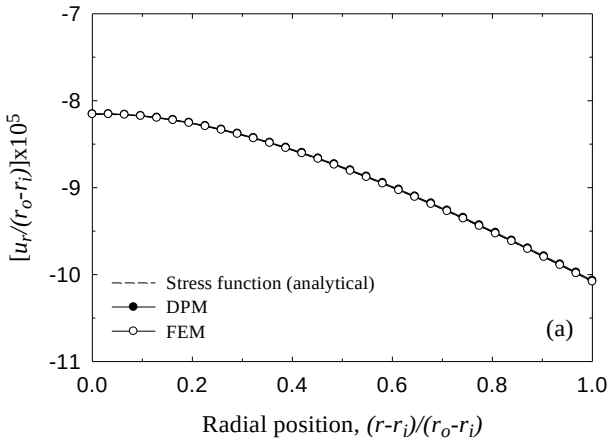


(a)

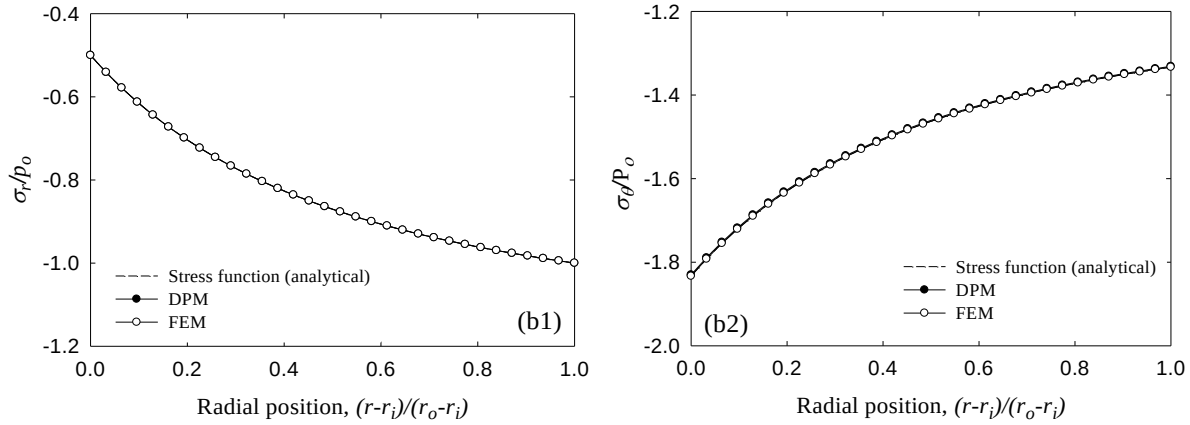


(b)

**Figure 4.2:** Comparison of solution for (a) displacement and (b) stresses in a thick-walled pressure vessel, $r_o/r_i = 2$.

## 4.3 CURVED BEAM UNDER PURE BENDING

A curved beam with a constant narrow rectangular cross section and a circular axis is considered here. The beam is bent in the plane of curvature by couple $M$ applied at the ends as shown in Fig. 4.3. The curved beam considered here has outer to inner radius ratio as, $r_o/r_i = 2.0$ and the width of the beam cross section is unity. The material properties of the beam are considered as, modulus of elasticity, $E = 207$ GPa and Poisson's ratio, $\nu = 0.29$.

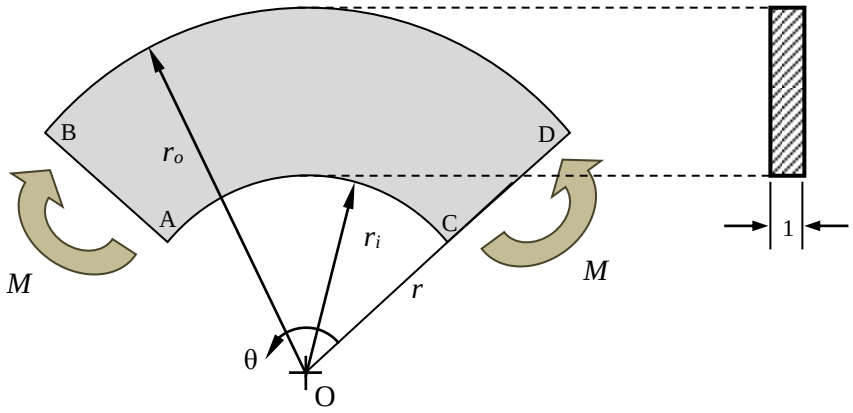


**Figure 4.3:** Curved beam under pure bending moment.

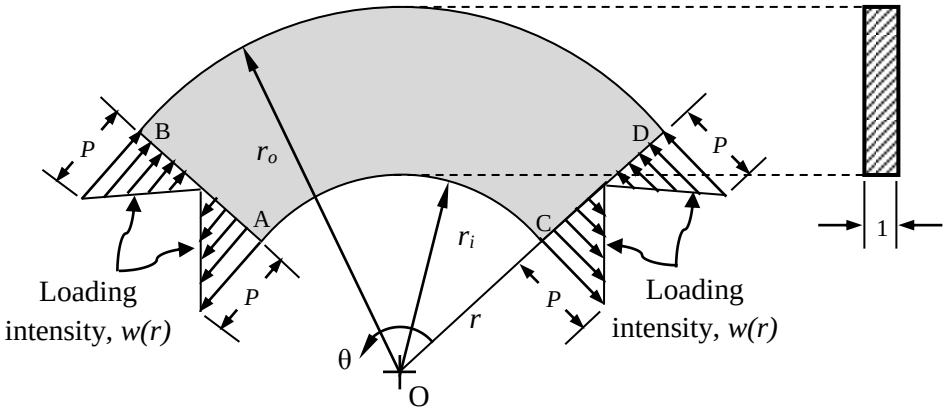


**Figure 4.4:** Modeling of end moment in terms of distributed circumferential stress.

A (35 × 45) uniform curvilinear finite-difference mesh network is used to discretize the curved beam. The bending moment applied at the beam ends is modeled in terms of a linearly varying circumferential stresses as shown in Fig. 4.4. The boundary conditions at different surfaces of the beam which are used to generate the present DPM solutions are listed in Table 4.2. Since the thickness of the beam is unity, the loading intensity *w(r)*, at any point at the left or right radial surface actually represents the value of circumferential stress at that point. No special care is necessary to model the four corner points of the curved beam as there are only

three conditions available at each point due to the common zero shear stress condition from each side of the corner points.

The exact analytical solution of this curved beam problem is available in the literature [5], where the bending moment is considered as constant along the length of the beam. As a result, the analytical solution considers the stress distribution same in all radial cross sections and thus gives the distribution of stress components along the axis of symmetry of the beam.

Table 4.2

Boundary conditions used for the curved beam under pure bending action

| Problem | Boundary | Boundary conditions | |
|---|---|---|---|
| | | Normal component | Tangential component |
| Curved beam under pure bending (Fig. 4.3) | Right radial surface, $\theta = 0^o$ | $\sigma_\theta(r, 0) = w(r)$ | $\tau_{r\theta}(r, 0) = 0$ |
| | Left radial surface, $\theta = \theta_{\max}$ | $\sigma_\theta(r, \theta_{max}) = w(r)$ | $\tau_{r\theta}(r, \theta_{max}) = 0$ |
| | Outer circumferential surface, $r = r_o$ | $\sigma_r(r_o, \theta) = 0$ | $\tau_{r\theta}(r_o, \theta) = 0$ |
| | Inner circumferential surface, $r = r_i$ | $\sigma_r(r_i, \theta) = 0$ | $\tau_{r\theta}(r_i, \theta) = 0$ |

where,

$$w = \begin{cases} \dfrac{p}{r_0 - r_i}\left(r_o + r_i - 2r\right) & \text{for,} \quad r_i \le r \le \dfrac{r_o + r_i}{2} \\ \dfrac{p}{r_0 - r_i}\left(-r_o + r_i - 2r + 2\right) & \text{for,} \quad \dfrac{r_o + r_i}{2} \le r \le r_o \end{cases}$$

The exact analytical solutions for different stress components obtained using stress function approach is given in the following equations:

$$\sigma_r = -\frac{4M}{N}\left(\frac{r_i^2 r_o^2}{r^2}\log\frac{r_o}{r_i} + r_o^2\log\frac{r}{r_o} + r_i^2\log\frac{r_i}{r}\right) \tag{4.4}$$

$$\sigma_\theta = -\frac{4M}{N}\left( -\frac{r_i^2 r_o^2}{r^2}\log\frac{r_o}{r_i} + r_o^2\log\frac{r}{r_o} + r_i^2\log\frac{r_i}{r} + r_o^2 - r_i^2 \right) \tag{4.5}$$

$$\tau_{r\theta} = 0 \tag{4.6}$$

where,

$$A = -\frac{4M}{N} r_i^2 r_o^2 \log\frac{r_o}{r_i},$$

$$B = -\frac{2M}{N}\left(r_o^2 - r_i^2\right),$$

$$C = \frac{M}{N}\left[ r_o^2 - r_i^2 + 2\left(r_o^2\log r_o - r_i^2\log r_i\right)\right] \quad \text{and}$$

$$N = \left(r_o^2 - r_i^2\right)^2 - 4r_i^2 r_o^2\left(\log\frac{r_o}{r_i}\right)^2$$

### 4.3.1 Comparison of Results

This section presents the solution of the curved beam under pure bending moment. The numerical solution obtained using the present DPM is presented along with the exact analytical solution for comparison. To make the results non-dimensional the stress components are expressed as the ratio of stresses to the maximum loading intensity, *P* (Fig. 4.4), used to model the end moments.

Figure 4.5(a) describes the distribution of radial stress along the radial position of the beam. The radial stress is found to be zero at the inner and outer surface of the beam. Maximum radial stress is found to be at a distance of 39% of the beam thickness from the inner surface of the beam. Figure 4.5(b) shows the distribution of tangential stress along the radial position of the beam. The maximum tangential stress is found to be at the inner surface of the beam which decreases along the beam thickness and takes negative value after the neutral axis which is found at about 45% of the beam thickness from the inner surface of the beam. Moreover the maximum tangential stress is found to be 7.25 times the maximum radial stress for the current curved beam ($r_o/r_i$ = 2). Finally, the excellent agreement between the solutions of the analytical and the numerical approaches for both radial and tangential stress components as observed from Fig. 4.5 validates the present finite-difference computational method based on displacement potential.

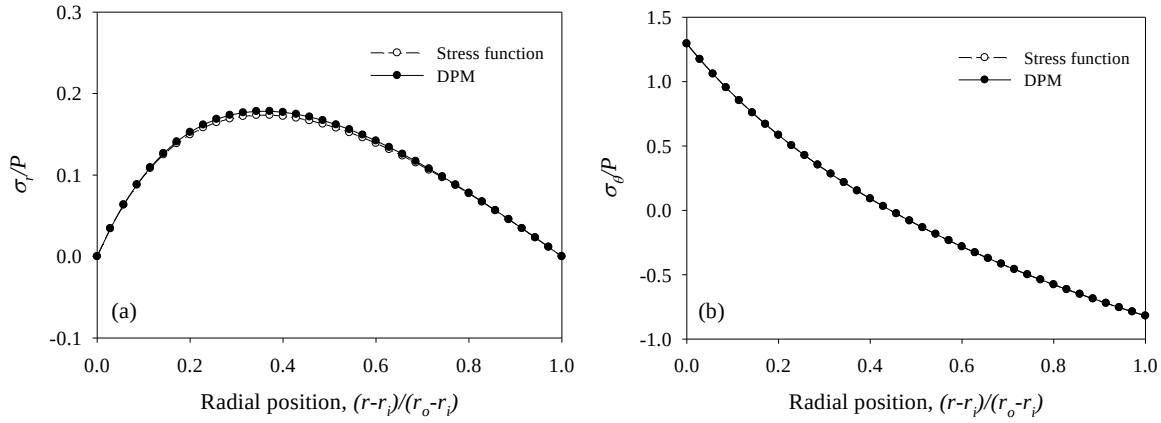


**Figure 4.5:** Comparison of solution for stresses in a curved beam under pure bending along the line of symmetry, $r_o/r_i = 2$.

## 4.4 VERIFICATION OF CORRESPONDENCE BETWEEN FORMULATION-I AND II

The development of the present displacement potential field formulation eventually leads to two different versions of the formulation as mentioned earlier in chapter 2. These formulations are denoted by Formulation-I and Formulation-II. The original two variable ($u_r$ and $u_\theta$) equilibrium problem has been reduced to a single variable (potential function $\psi$) problem through the application of a variable reduction scheme, the process of which however gives rise to an option to choose one of the equilibrium equations for necessary treatments. It has been observed that both the second order elliptic partial differential equations of equilibrium are transformed to the same fourth order partial differential equation of equilibrium when expressed in terms potential function $\psi$. As a result, the two formulations, namely Formulation-I and Formulation-II are based on the same governing differential equation of equilibrium, although the potential function itself is defined in two different ways in case of the two formulations. Finally, the relevant displacement and stress components become different in terms of both the derivatives and coefficients when expressed in terms of the potential function in the two formulations.

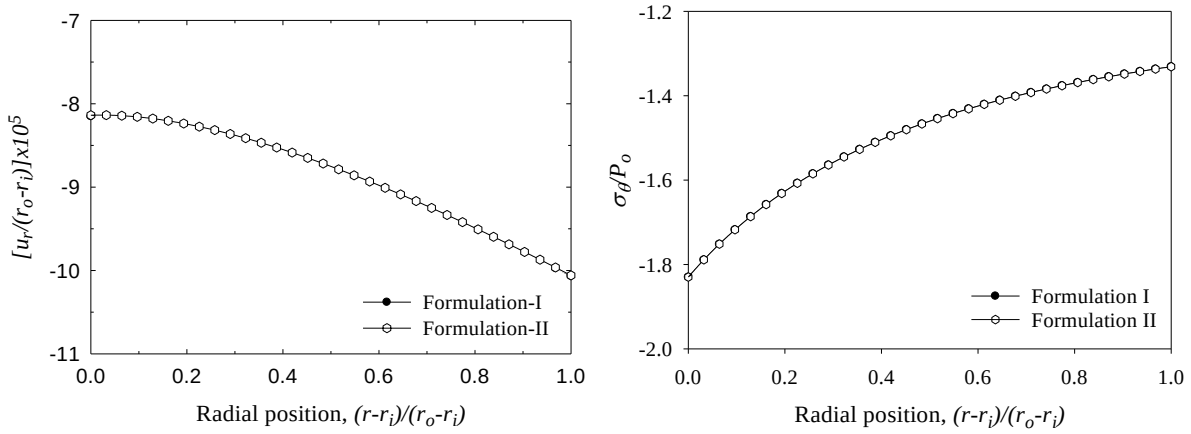


(a) (b)

**Figure 4.6:** Comparison of solutions of the thick-walled pressure vessel obtained by Formulation I and II: (a) radial displacement, (b) circumferential stress.

In this section an attempt is made to verify the correspondence between the two formulations derived. The capability of the original computer program is extended by incorporating the provision of solving a problem using either Formulation-I or Formulation-II. The classical stress problem of thick-walled pressure vessel is considered for verifying the correspondence of the two formulations and the results are compared. The same boundary conditions as well as the finite difference computational mesh network are used to solve the problem using the two formulations. All the results of displacement and stress components at different radial locations of the body are found to be in excellent agreement with each other. Fig. 4.6 demonstrated the correspondence between the two formulations through the comparison of solution for radial displacement and circumferential stress along the radial direction of the pressure vessel. The displacement potential computational method is thus once again verified to be founded on sound philosophy as the results obtained through the two formulations are in excellent agreement with each other. The accuracy of Formulation-I has already been checked by comparing the results with the corresponding results of FEM and stress function in Fig. 4.2. Both the computer programs based on Formulation-I and Formulation-II are thus verified to be reliable and free from errors.

Chapter 05

# ANALYSIS OF CURVED BEAMS

## 5.1 INTRODUCTION

Stress field of two different types of curved beams are analyzed under the influence of different loading conditions. An efficient algorithm is developed, in which the new displacement potential is used to model the problem of curved beams with mixed and changeable boundary conditions. Problem-I is a both-ends-fixed curved beam under uniform radial pressure. Problem-II is a stiffened curved beam which is rigidly fixed at its one end and the other end is subjected to uniform shear and tensile loading. The two opposing curved edges of the beam are subjected to rigid circumferential stiffeners. Solutions of stresses and displacements along different radial and tangential locations are obtained, some of which, especially those around the critical regions are presented in a comparative fashion mainly in the form of graphs. Comparison has also been made with the available numerical solutions obtained using standard methods.

## 5.2 BOTH-ENDS-FIXED CURVED BEAM

A beam of narrow rectangular cross section and with a circular axis is constrained at both ends and is under the action of uniformly distributed radial loading on its convex surface as shown in Fig. 5.1. The beam has an angular span of $90^o$ and outer to inner radius ratio as, $r_o/r_i = 1.75$.

A (45 × 55) uniform curvilinear mesh network is used to discretize the curved beam as shown in Fig. 5.2. Analytical solution with mixed boundary conditions like this problem has rarely been attempted as the boundary conditions of these practical elastic problems pose serious difficulty in their solutions. As a result, no satisfactory analytical solution for this problem is available in the literature and thus the solutions from $\psi$-formulation are only compared with the solutions from FEM.

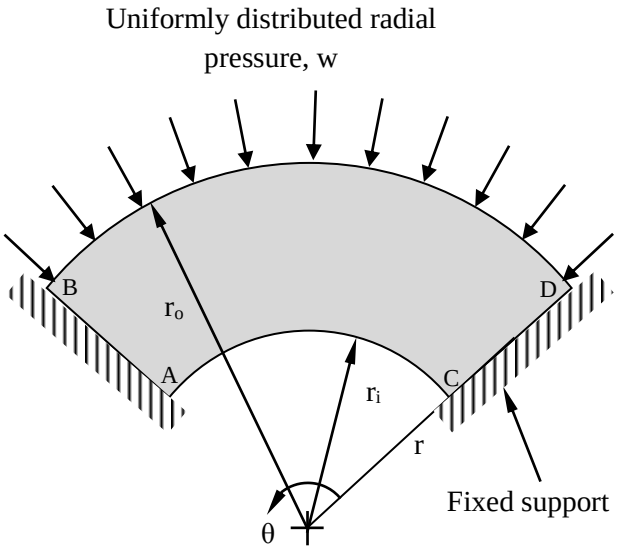


**Figure 5.1:** Both-ends-fixed curved beam under uniform radial pressure at the outer surface.

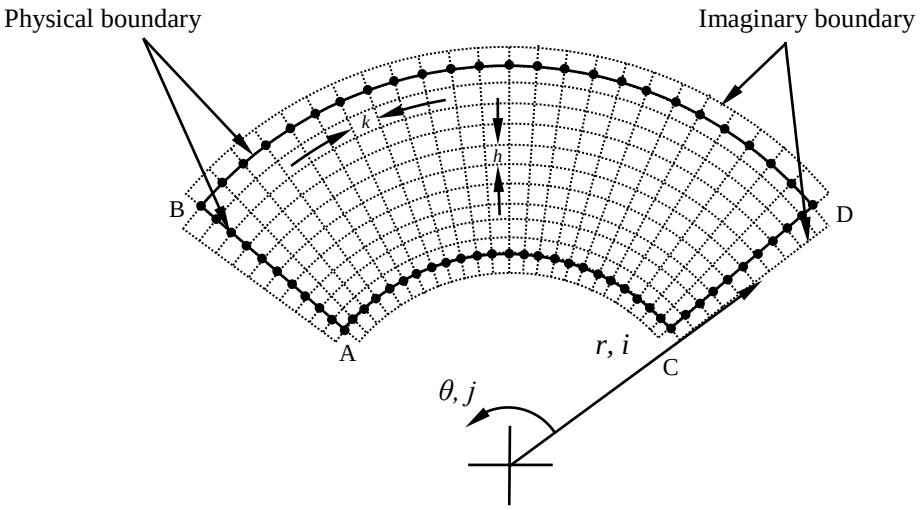


**Figure 5.2:** Discretization of the both-ends-fixed curved beam.

The boundary conditions at different surfaces of the beam which are used to generate the present DPM solutions are listed in Table 5.1. Special cares have been taken to model the boundary conditions at the four corner nodes of the beam, the details of which are illustrated in Table 5.2.

Table 5.1

Boundary conditions used for the both-ends-fixed beam for obtaining the present solution

| Problem | Boundary | Boundary conditions | |
|---|---|---|---|
| | | Normal component | Tangential component |
| Both-ends-fixed beam (Fig. 5.1) | Right radial surface, $\theta=0^o$ | $u_r(r, 0)=0$ | $u_\theta(r, 0)=0$ |
| | Left radial surface, $\theta= \theta_{\max}$ | $u_r(r, \theta_{max})=0$ | $u_\theta(r, \theta_{max})=0$ |
| | Outer circumferential surface, $r=r_o$ | $\sigma_r(r_o, \theta)=-w$ | $\tau_{r\theta}(r_o, \theta)=0$ |
| | Inner circumferential surface, $r=r_i$ | $\sigma_r(r_i, \theta)=0$ | $\tau_{r\theta}(r_i, \theta)=0$ |

Table 5.2

Boundary condition modeling for the corner points of the both-end-fixed beam

| Corner point* | Given boundary conditions | Used conditions | Correspondence between mesh-points and given boundary conditions | |
|---|---|---|---|---|
| | | | Mesh point on the physical boundary | Mesh point on the imaginary boundary |
| A | $[(u_n, u_t), (\sigma_n, \sigma_t)]$ | $[u_n, u_t, \sigma_t]$ | $u_\theta=0$ | $u_r=0, \tau_{r\theta}=0$ |
| B | $[(u_n, u_t), (\sigma_n, \sigma_t)]$ | $[u_n, u_t, \sigma_t]$ | $u_\theta=0$ | $u_r=0, \tau_{r\theta}=0$ |
| C | $[(u_n, u_t), (\sigma_n, \sigma_t)]$ | $[u_n, u_t, \sigma_t]$ | $u_\theta=0$ | $u_r=0, \tau_{r\theta}=0$ |
| D | $[(u_n, u_t), (\sigma_n, \sigma_t)]$ | $[u_n, u_t, \sigma_t]$ | $u_\theta=0$ | $u_r=0, \tau_{r\theta}=0$ |

* Refer to Fig. 5.1.

It can be seen from Table 5.2 that three out of the available four boundary conditions are satisfied at each corner nodes of the domain and the remaining one is taken as redundant. It can be mentioned that usual computational approaches use two out of four conditions at each

corner nodes to generate the solution and thus the stress obtained, especially around the corner regions of the two supporting ends deviate more from the actual state of stresses.

### 5.2.1 Distribution of displacement components

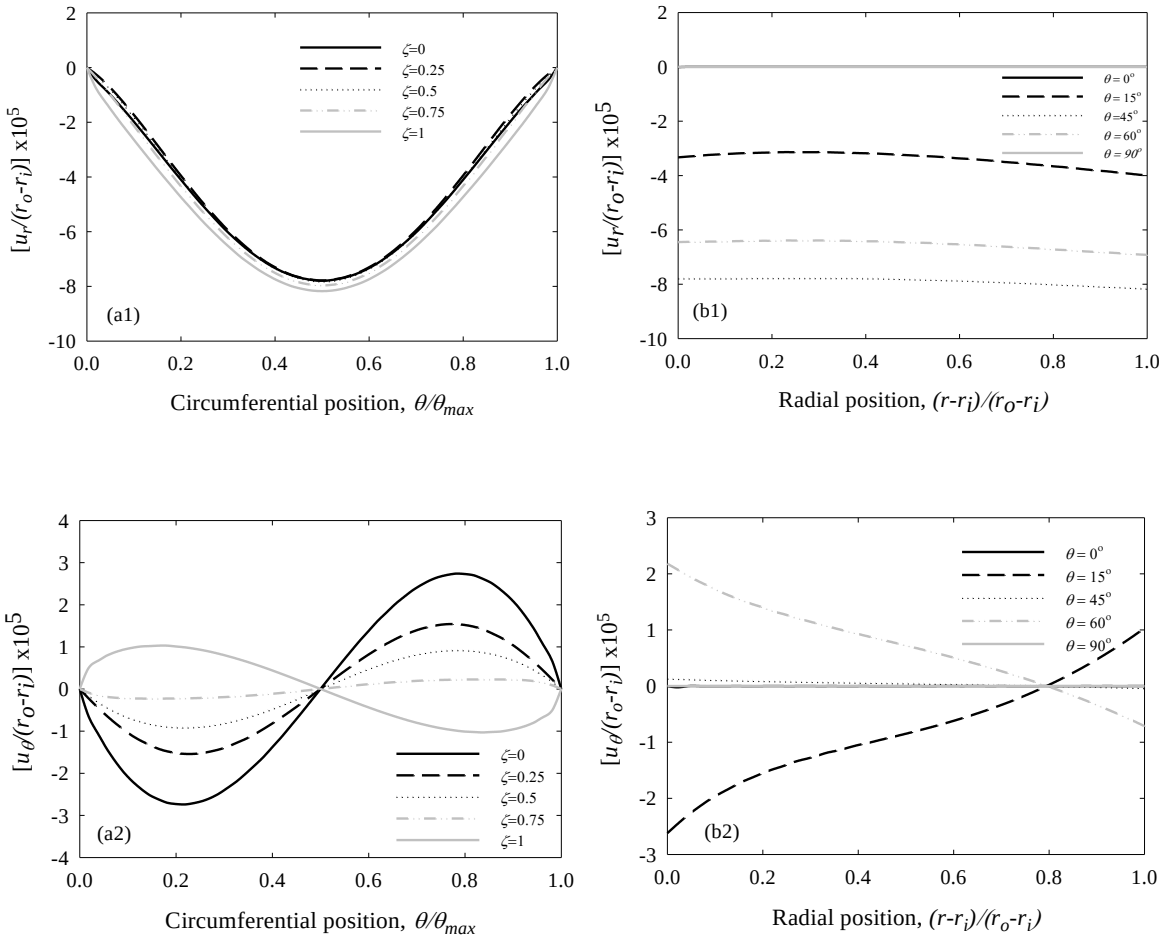


**Fig. 5.3:** Distribution of (a1) radial displacement along circumferential position, (b1) radial displacement along radial position, (a2) tangential displacement along circumferential position and (b2) tangential displacement along radial position.

This section describes the distribution of displacement components at different beam sections as obtained from the new displacement potential formulation (Formulation-I). In the case of present problem, displacement components are normalized with respect to the beam thickness ($r_o$-$r_i$). The distribution is presented along both circumferential and radial position of the beam. To identify the results of tangential layers at different radial positions, a radial function is defined as, $\xi = (r\text{-}r_i)/(r_o\text{-}r_i)$; $\xi = 0$ and 1 refer to the inner and outer edges of the curved

beam, respectively. For distributions along radial positions, five different radial layers have been considered with angular positions as, $\theta = 0^o$, $15^o$, $45^o$, $60^o$ and $90^o$.

Fig. 5.3(a1) describes the distribution of radial displacement along the circumferential position of the beam. Distributions for five different tangential layers have been considered with the value of radial function $\xi = 0$, 0.25, 0.5, 0.75 and 1.0. From the distributions it is seen that, at both the fixed ends, the radial displacements are zero (as expected), which are found to increase from the ends towards the mid-section, and eventually the maximum radial displacement is observed at the mid-span section of the beam. Since two ends of the beam are fixed, this satisfies the boundary conditions at these two ends properly. Again, the outer circumference (convex circumference) of the beam which is loaded by uniform radial pressure is found to have the maximum radial displacement.

Fig. 5.3(b1) shows the distribution of the radial displacement along radial positions of the beam. Both the fixed ends of the beam ($\theta = 0^o$, $90^o$) are found to have zero radial displacement and thus conforms to the applied boundary condition appropriately. Maximum radial displacement is found to occur at the radial layer with, $\theta = 45^o$. Radial displacement is found to vary almost linearly along the radial position of the beam.

Fig. 5.3(a2) and 5.3(b2) describes the distribution of tangential displacement along circumferential position and radial position of the beam respectively. From the figure the tangential displacement is found to be anti-symmetric about the mid-span section of the beam. Maximum tangential displacement is found at the inner circumference of the beam. The ends are found to have zero tangential displacement which satisfies the given boundary conditions at these ends.

### 5.2.2 Distribution of stress components

This section describes the distribution of stress components at different beam sections as obtained from the new displacement potential formulation (Formulation-I). For this purpose, the stress components are normalized with respect to the radial loading parameter, $w$. In this case also, the distribution is presented along both circumferential and radial position of the beam where, different tangential and radial layers of the beam are expressed by different values of $\xi$ and $\theta$ respectively.

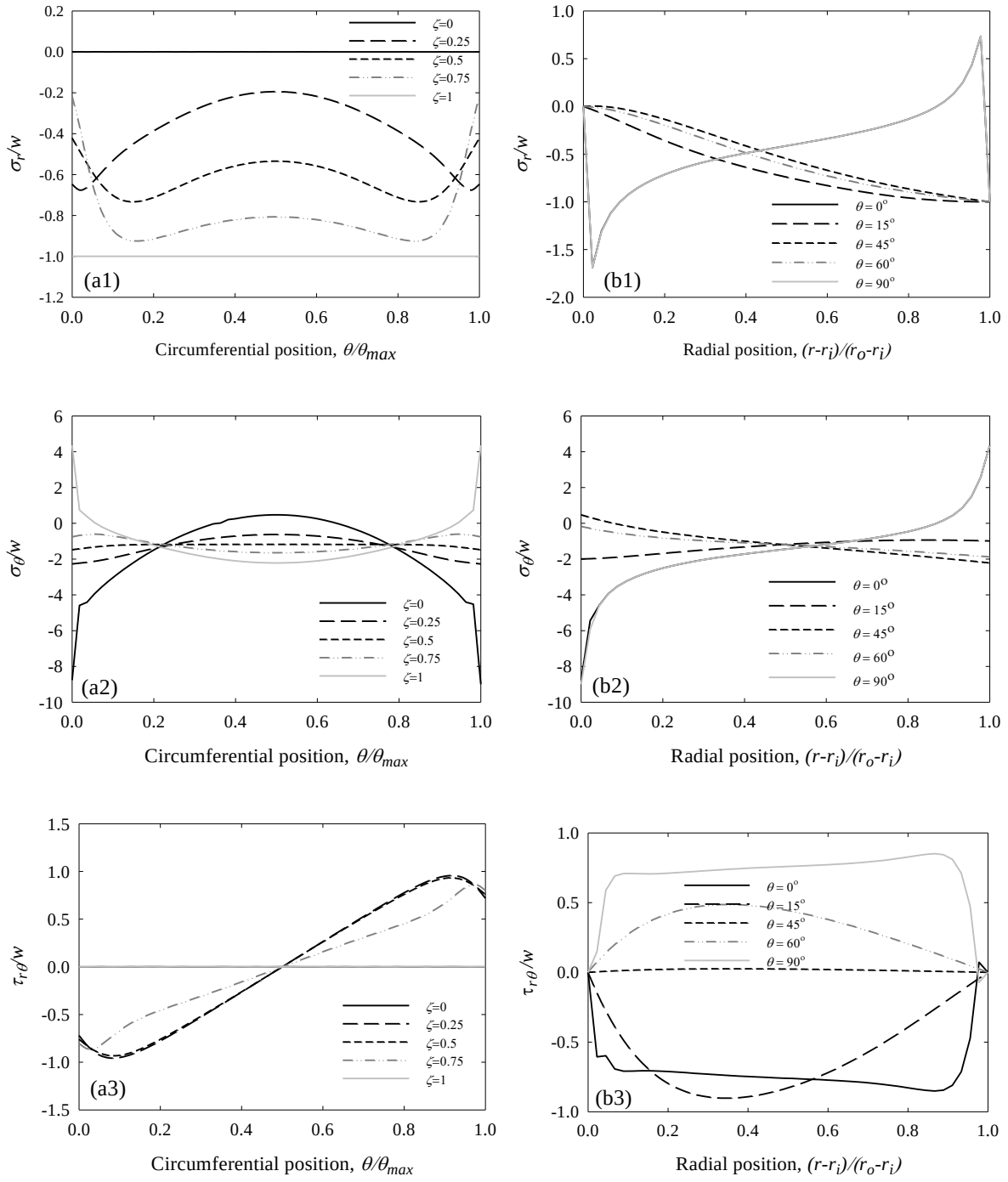


**Figure 5.4:** Distribution of (a1) radial stress along circumferential position, (b1) radial stress along radial position, (a2) tangential stress along circumferential position, (b2) tangential stress along radial position, (a3) shear stress along circumferential position, (b3) shear stress along radial position.

Fig. 5.4(a1) describes the distribution of radial stress component along the beam circumference. As expected, the distribution is found to be symmetric about the mid-span of the beam. The inner and outer circumference of the beam is found to have zero and unity value of normalized radial stress respectively. This is in perfect agreement with the given boundary conditions at inner and outer circumference of the curved beam. The radial stress for rest of the tangential layers resides in between the inner and outer layer of the beam. Fig. 5.4(b1) shows the distribution of radial stress along the radial position for five different tangential positions ($\theta$ = 0$^o$, 15$^o$, 45$^o$, 60$^o$ and 90$^o$) of the beam. The value of normalized radial stress is found to vary in between zero and unity except the two fixed ends which is found to experience a stress concentration just before the inner and outer circumferences of the beam.

Fig. 5.4(a2) illustrates the distribution of tangential stress component along circumferential position of the beam. Again in this case also the distribution is found to be symmetrical about the mid-span of the beam. The maximum tangential stress occurs at the inner circumference of the beam followed by the outer circumference. Fig. 5.4(b2) shows the distribution of tangential stress along radial position of the beam. The maximum stress occurs at the fixed ends of the beam which is found to be more than 8 times the applied loading. Fig. 5.4(a3) depicts the variation of shear stress along the circumference of the beam. The shear stress component is found to be anti-symmetric about the mid-span of the beam. The inner and outer circumference of the beam is found to have zero shear stress which satisfies the applied boundary condition appropriately. Distribution of shear stress along the radial position is shown in Fig. 5.4(b3). Shear stress for all the radial layers is found to have zero value at inner and outer radius of the beam. Shear stress is found to be zero along the $\theta$ = 45$^o$ layer which is the layer of symmetry.

### 5.2.3 Effect of curvature

This section describes the effects of curvature on the distribution of tangential stress and shear stress components. Here, the fixed end has been chosen as the section of interest to demonstrate the effect as it has been identified as the most critical section of the beam in terms of stresses. This effect is realized in terms of a curvature parameter $C_r$ which is defined by the following relation [23]:

$$C_r = \int_{r_i}^{r_o} \frac{1}{r} dr = \ln \frac{r_o}{r_i} \tag{5.1}$$

The results have been shown for five different values of $C_r$ ranging from 0.26 to 1.09. It is important to mention here that the thickness of the beam is kept constant for all five cases of different curvature values.

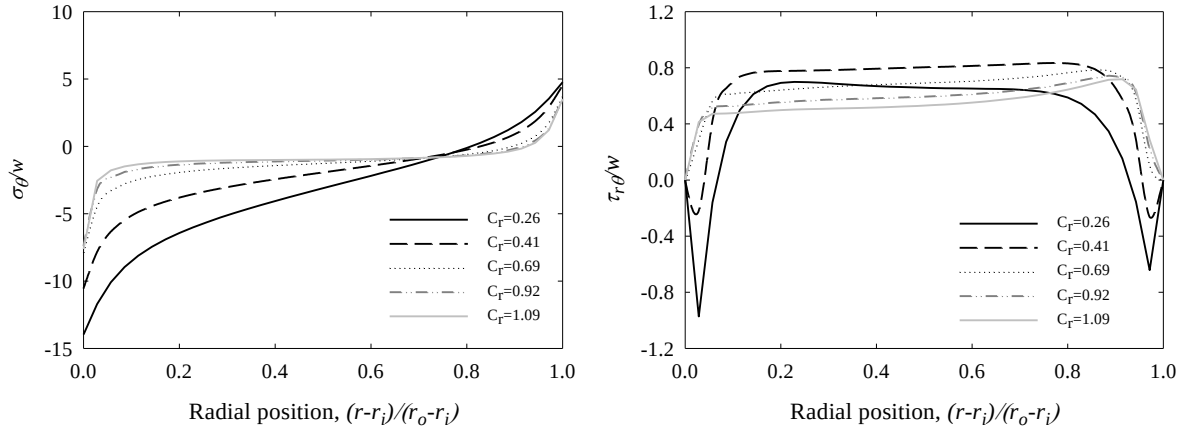


**Figure 5.5:** Effect of curvature on the distribution of: (a) tangential stress, (b) shear stress at inner fixed end.

Fig. 5.5(a) shows the effect of curvature on the tangential stress component along the radial position at the fixed end of the beam. The tangential stress is found to increase with the decrease of curvature and the maximum value of stress is observed at the inner radial position of the beam. Fig. 5.5(b) demonstrates the effect of curvature on the shear stress component along the radial position at the fixed end of the bar. The shear stress is also found to increase with the decrease of curvature. A stress concentration is observed at the inner and outer radial locations of the beam for $C_r \leq 0.4$.

### 5.2.4 Deformed shape

Fig. 5.6 describes the original and deformed shapes of the both-ends-fixed beam under uniform radial pressure over its convex surface. The deformation is 1000 times magnified to make the deformation observable. As expected, no deformation can be observed at the fixed

ends of the beam. Deformation increases from zero to maximum value from the fixed end to the mid-circumference of the beam. Moreover the deformed shape of the beam is found to be symmetrical about the mid-circumference likewise the original shape of the beam.

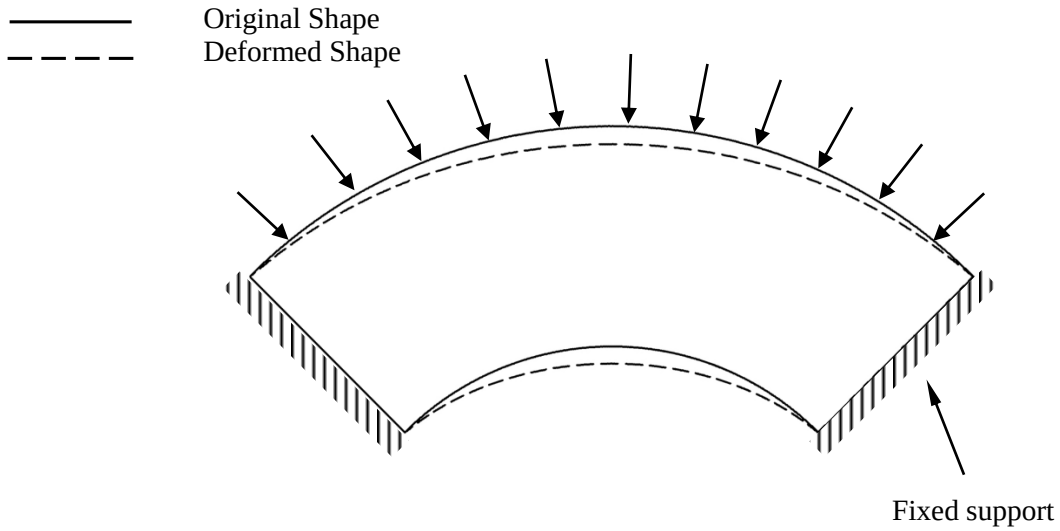


**Figure 5.6:** Original and deformed shapes of the both-ends-fixed curved beam ($r_o/r_i$ = 1.75) under uniform radial pressure (magnification factor = 1000).

### 5.2.5 Comparison of the present $\psi$-formulation solution with the FEM solution

Analytical solutions of stress problem with mixed boundary conditions, like the present beam problem have rarely been attempted as the boundary conditions pose serious difficulty in their solution process. It is mentioned that exact analytical solution for stresses in the built-in beam is not available in the literature, and thus the present $\psi$- solutions are compared with the corresponding solutions obtained by FEM. Finite element solutions were obtained using the same PLANE 183 element with a dense element network that comprises of a total 12780 nodal points.

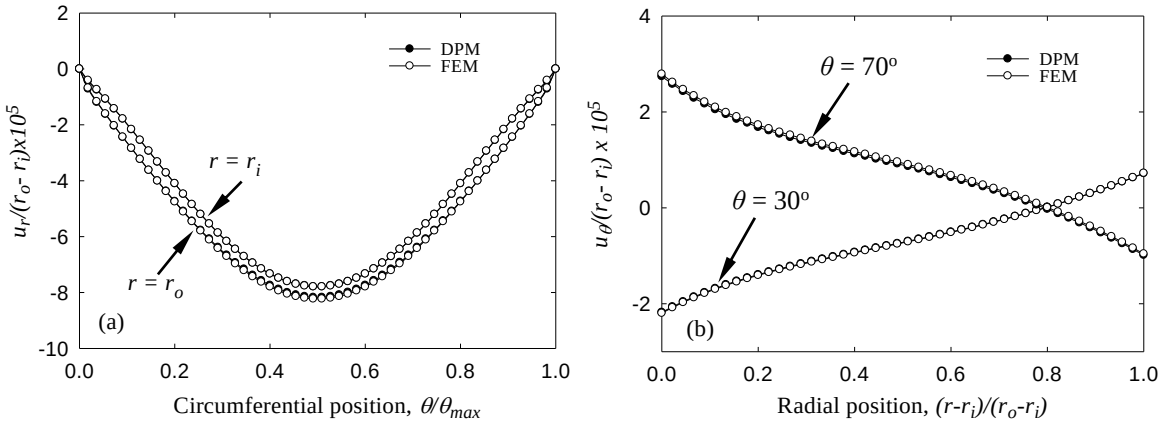


**Figure 5.7:** Comparison of solutions of displacement components at different sections of the both-ends-fixed curved beam (Problem-II): (a) radial displacement, (b) circumferential displacement.

Fig. 5.7(a) presents the distribution of radial displacement along the inner and outer circumferences of the beam. The inner and outer circumferences have been chosen here for consideration, because the maximum and minimum radial displacements are found to occur at these surfaces. The figure compares the present DPM solutions with the corresponding FEM solutions of the beam. From the distributions it is seen that, at both the fixed ends, the radial displacements are zero (as expected), which are found to increase from the ends towards the mid-section, and eventually the maximum radial displacement is observed at the mid-span section of the beam. The distribution of tangential component of displacement for two different circumferential sections ($\theta$ = 30$^o$, $\theta$ = 70$^o$) is shown along the beam depth in Fig. 5.7(b). It should be noted here that due to the anti-symmetric nature of distribution of the tangential displacement component with respect to mid-span section, the value of tangential displacement for $\theta$ = 30$^o$ changes from negative to positive value at the inner and outer circumference, respectively, whereas the displacement for $\theta$ = 70$^o$ decreases from its maximum positive value at the inner surface to a negative value at the outer circumference of the beam. From the comparison of two solutions, namely, DPM and FEM for both the displacement components at different sections of beam, it is observed that the two solutions are in excellent agreement with each other, both in terms of magnitude as well as nature of variation.

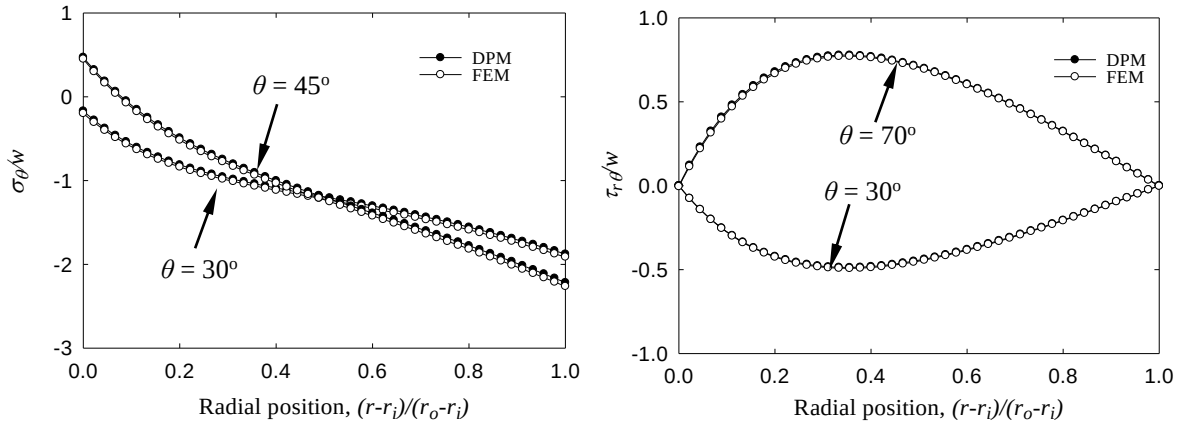


(a) (b)

**Figure 5.8:** Comparison of solutions of stress components at different sections of the both-ends-fixed curved beam (Problem- II): (a) circumferential stress, (b) shear stress.

Fig. 5.8 shows the comparison of solutions of stress components at different sections of the beam. Fig 5.8(a) shows the distribution of the normalized bending stress along the beam depth for two different circumferential sections of the beam. The distributions are found to differ from the standard linear distributions of bending stresses in a straight beam. More specifically, the nonlinearity associated with the distributions is prominent particularly for the lower half of the beam depth. Bending stress distributions for sections $\theta = 30^o$ and $45^o$ show that the majority portion of the beam is under compression. More specifically, for the mid-span section ($\theta = 45^o$), only 1% of the depth near the inner boundary is under tension. Fig. 5.8(b) depicts the distribution of shear stress over the beam depth for two different circumferential sections, $\theta = 30^o$ and $70^o$. Due to anti-symmetric nature of the distribution, one of the distributions is concave upward and the other is concave downward. At both the inner and outer surface of the beam, the value of shear stress is found to be zero, which, in turn, reveals the conformity of the present solutions with the given boundary conditions ($\tau_{r\theta} = 0$ at both $r = r_i$ and $r = r_o$ ). Another interesting thing is that the curvature of the beam causes the shear distribution over the beam depth to deviate from the standard parabolic distribution obtained for the case of straight slender beams. Likewise the case of displacements, the present single function computational solutions for stress at different sections of the beam are found to be in excellent agreement with the corresponding solutions of standard computational approach.

## 5.3 STIFFENED CURVED BEAMS

A curved beam with circular axis is considered, where the inner and outer edges of the beam are subjected to circumferential stiffeners. The beam is assumed to have a narrow rectangular cross section with an angular span of 90°, and the outer to inner radius ratio ($r_o/r_i$) is varied over a range from 1.1 to 3.0. One end of the beam is rigidly fixed and the other end is subjected to two different loading conditions as illustrated in Fig. 5.9. Material properties of the beam, namely, modulus of elasticity and Poisson's ratio are taken as E = 207 GPa and ν = 0.29, respectively. A uniform curvilinear mesh network of (61×71) mesh points is used to discretize the curved beam.

The use of stiffeners in the construction of marine and aerospace structure is quite extensive. The stiffeners are basically designed to meet the strength or stiffness requirements of a particular situation. At the stiffened boundary the stiffness of the material is very high which implies a very low strain and thus a very low deformation. Stiffeners are mathematically modeled by considering zero strain/displacement at the stiffened region. In case where rigid body motion of the structure is allowed the stiffener is mainly modeled by considering zero strain at the stiffened region but in case where rigid body motion is not allowed and the stiffener is connected to the fixed end zero strain condition and zero displacement condition both gives the same effect.

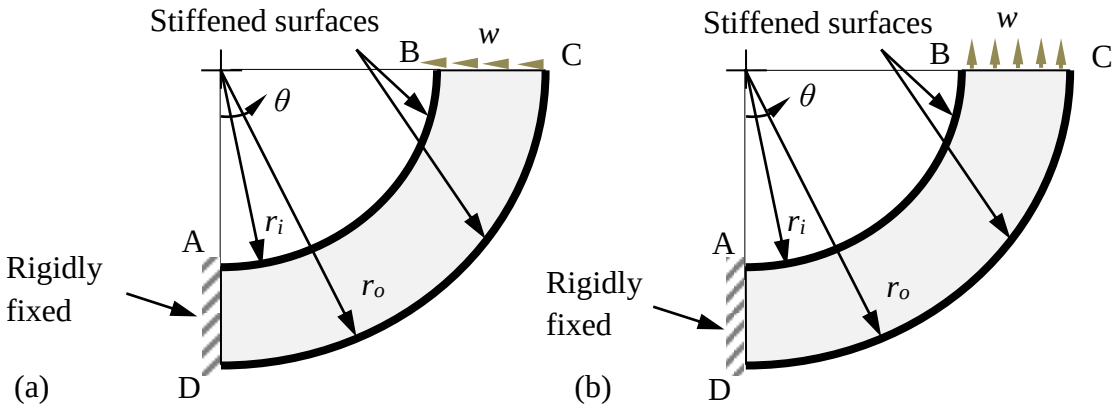


**Figure 5.9:** Thick stiffened curved beam under (a) shear loading (case- I); (b) tensile loading (case- II).

The boundary conditions at different surfaces of the beam which are used to generate the present DPM solutions are listed in Table 5.3 and 5.4. Special cares have been taken to model

the boundary conditions at the four corner nodes of the beam, the details of which are illustrated in Table 5.5 and 5.6.

Table 5.3

Boundary conditions used for the curved stiffened beam under shear for obtaining the present solution

| Problem | Boundary | Boundary conditions | |
|---|---|---|---|
| | | Normal component | Tangential component |
| Curved stiffened beam (Fig. 5.9(a)) | Left radial surface, $\theta=0^o$ | $u_r(r, 0)=0$ | $u_\theta(r, 0)=0$ |
| | Right radial surface, $\theta=\theta_{max}$ | $\sigma_\theta(r, \theta)=0$ | $\tau_{r\theta}(r_o, \theta)=-w$ |
| | Outer circumferential surface, $r=r_o$ | $\sigma_r(r_o, \theta)=0$ | $u_\theta(r_o, \theta)=0$ |
| | Inner circumferential surface, $r=r_i$ | $\sigma_r(r_i, \theta)=0$ | $u_\theta(r_i, \theta)=0$ |

Table 5.4

Boundary conditions used for the curved stiffened beam under tension for obtaining the present solution

| Problem | Boundary | Boundary conditions | |
|---|---|---|---|
| | | Normal component | Tangential component |
| Curved stiffened beam (Fig. 5.9(b)) | Left radial surface, $\theta=0^o$ | $u_r(r, 0)=0$ | $u_\theta(r, 0)=0$ |
| | Right radial surface, $\theta=\theta_{max}$ | $\sigma_\theta(r, \theta)=w$ | $\tau_{r\theta}(r_o, \theta)=0$ |
| | Outer circumferential surface, $r=r_o$ | $\sigma_r(r_o, \theta)=0$ | $u_\theta(r_o, \theta)=0$ |
| | Inner circumferential surface, $r=r_i$ | $\sigma_r(r_i, \theta)=0$ | $u_\theta(r_i, \theta)=0$ |

Table 5.5

Boundary condition modeling for the corner points of the curved stiffened beam under shear

| Corner point* | Given boundary conditions | Used conditions | Correspondence between mesh-points and given boundary conditions | |
|---|---|---|---|---|
| | | | Mesh point on the physical boundary | Mesh point on the imaginary boundary |
| A | $[(u_n, u_t), (\sigma_n, u_t)]$ | $[u_n, u_t, \sigma_n]$ | $u_\theta=0$ | $u_r=0, \sigma_r=0$ |
| B | $[(\sigma_n, u_t), (\sigma_n, \sigma_t)]$ | $[\sigma_n, \sigma_n, \sigma_t]$ | $\sigma_\theta=0$ | $\sigma_r=0, \tau_{r\theta}=-w$ |
| C | $[(\sigma_n, u_t), (\sigma_n, \sigma_t)]$ | $[\sigma_n, \sigma_n, \sigma_t]$ | $\sigma_\theta=0$ | $\sigma_r=0, \tau_{r\theta}=-w$ |
| D | $[(u_n, u_t), (\sigma_n, u_t)]$ | $[u_n, u_t, \sigma_n]$ | $u_\theta=0$ | $u_r=0, \sigma_r=0$ |

* Refer to Figure 5.9(a).

Table 5.6

Boundary condition modeling for the corner points of the curved stiffened beam under tension

| Corner point* | Given boundary conditions | Used conditions | Correspondence between mesh-points and given boundary conditions | |
|---|---|---|---|---|
| | | | Mesh point on the physical boundary | Mesh point on the imaginary boundary |
| A | $[(u_n, u_t), (\sigma_n, u_t)]$ | $[u_n, u_t, \sigma_n]$ | $u_\theta=0$ | $u_r=0, \sigma_r=0$ |
| B | $[(\sigma_n, u_t), (\sigma_n, \sigma_t)]$ | $[\sigma_n, \sigma_n, \sigma_t]$ | $\sigma_\theta=w$ | $\sigma_r=0, \tau_{r\theta}=0$ |
| C | $[(\sigma_n, u_t), (\sigma_n, \sigma_t)]$ | $[\sigma_n, \sigma_n, \sigma_t]$ | $\sigma_\theta=w$ | $\sigma_r=0, \tau_{r\theta}=0$ |
| D | $[(u_n, u_t), (\sigma_n, u_t)]$ | $[u_n, u_t, \sigma_n]$ | $u_\theta=0$ | $u_r=0, \sigma_r=0$ |

* Refer to Figure 5.9(b).

### 5.3.1 Distribution of displacement components

The solution for the distribution of displacement components of the stiffened curved beam as obtained by the present $\psi$- formulation (Formulation- II) is presented in this section. To make the results non-dimensional, the displacements are expressed as the ratio of the actual displacement and the thickness of the beam. To identify the results of tangential layers at different radial positions, a radial function is defined as, $\xi = (r\text{-}r_i)/(r_o\text{-}r_i)$; $\xi = 0$ and 1 refer to the inner and outer edges of the curved beam, respectively.

Fig. 5.10(a.1) and 5.10(b.1) describes the distribution of radial displacement along the length of the curved beam for case- I and case- II respectively. In both cases, the radial displacement is zero at the fixed end which is in full agreement with the given boundary condition at this end. For both shear and tensile loading the radial displacement is found to be dominant near the loaded end of the beam.

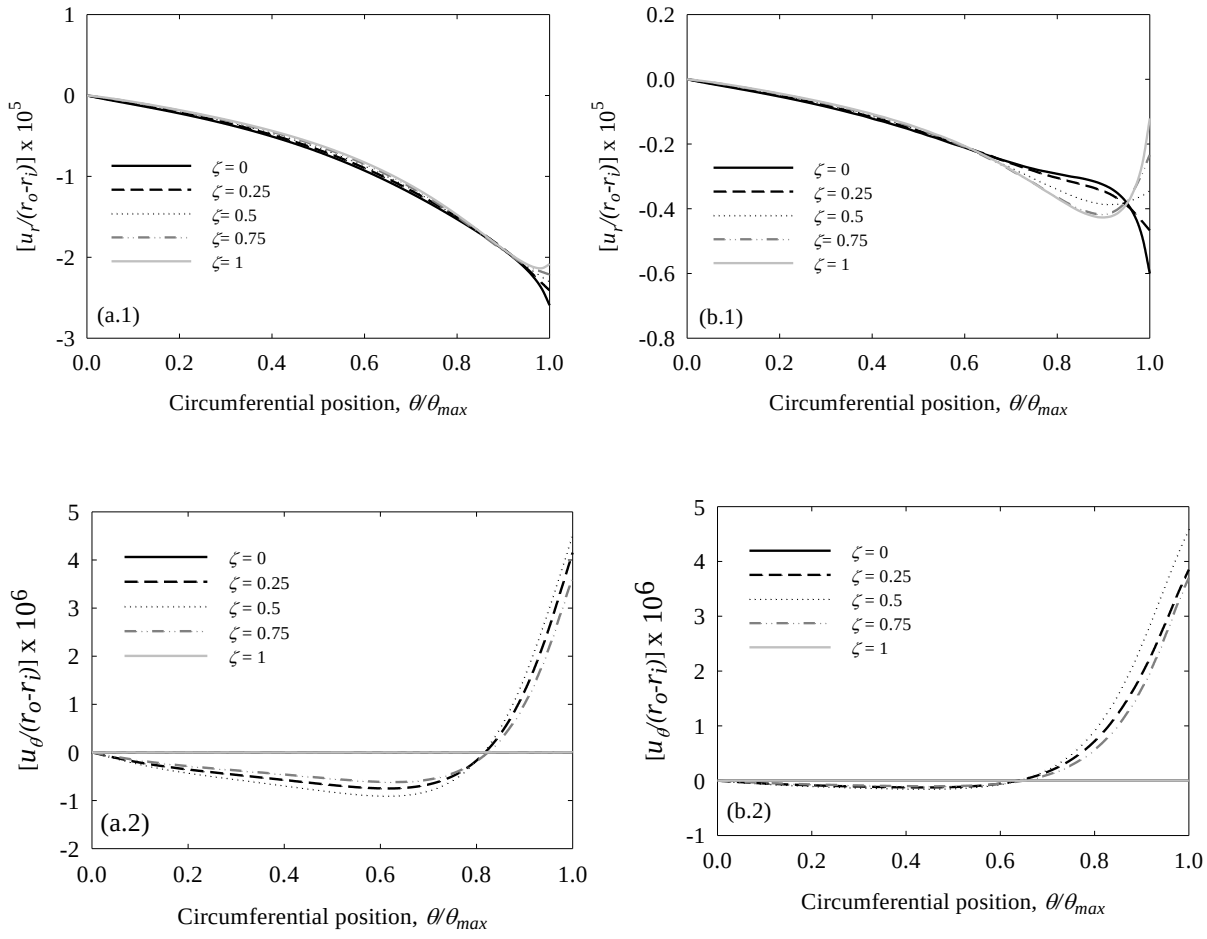


**Figure 5.10:** Distribution of displacement components along the beam length for (a) shear loading (case- I), (b) tensile loading (case- II)

Fig. 5.10(a.2) and 5.10(b.2) show the distributions of circumferential displacement along the length of the curved beam for case-I and case-II, respectively. In both cases, circumferential displacement along the inner and outer circumference is zero. This is in full conformity with the given boundary conditions for the circumferential stiffeners. In both cases, circumferential displacement becomes dominant for the regions near the loaded end. For the two different types of loadings, the distributions as well as the magnitudes of maximum circumferential displacements are found to be very similar.

### 5.3.2 Deformed shape

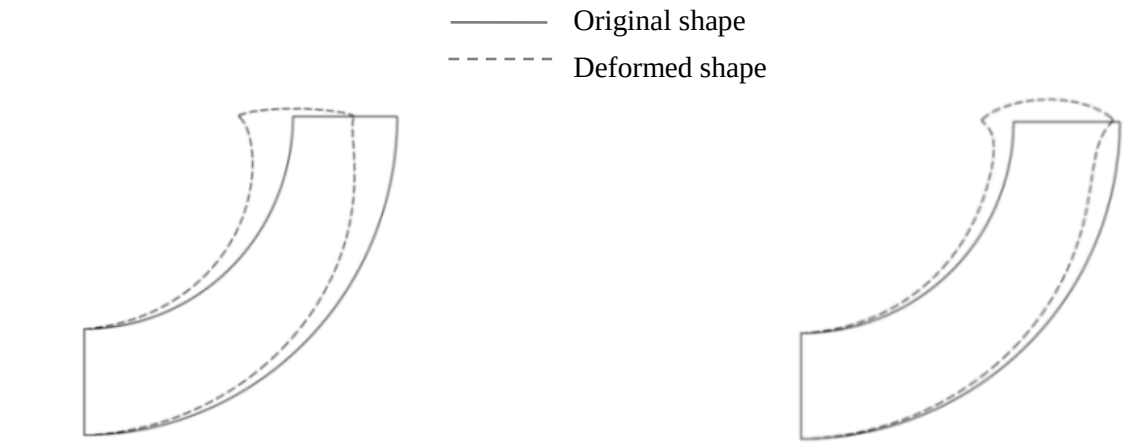


**Figure 5.11:** Original and deformed shapes for (a) case-I (magnification factor = 1000), (b) case-II (magnification factor = 5000)

Fig. 5.11(a) and (b) illustrate the original and deformed shapes of the curved beam ($r_o/r_i$ = 1.5) for both the cases of shear loading and tensile loading, respectively. The deformed shapes are found to assume somewhat similar configuration even though the corresponding loadings were different from each other. This is mainly because of the supporting condition as well as initial curvature of the bar.

### 5.3.3 Distribution of stress components

This section describes the distribution of stress components at different sections of the beam. To make the results non-dimensional, the stresses are expressed as the ratio of the stress and the applied loading parameter, $w$. To identify the results of tangential layers at different radial positions, a radial function is defined as, $\xi = (r\text{-}r_i)/(r_o\text{-}r_i)$; $\xi = 0$ and 1 refer to the inner and outer edges of the curved beam, respectively.

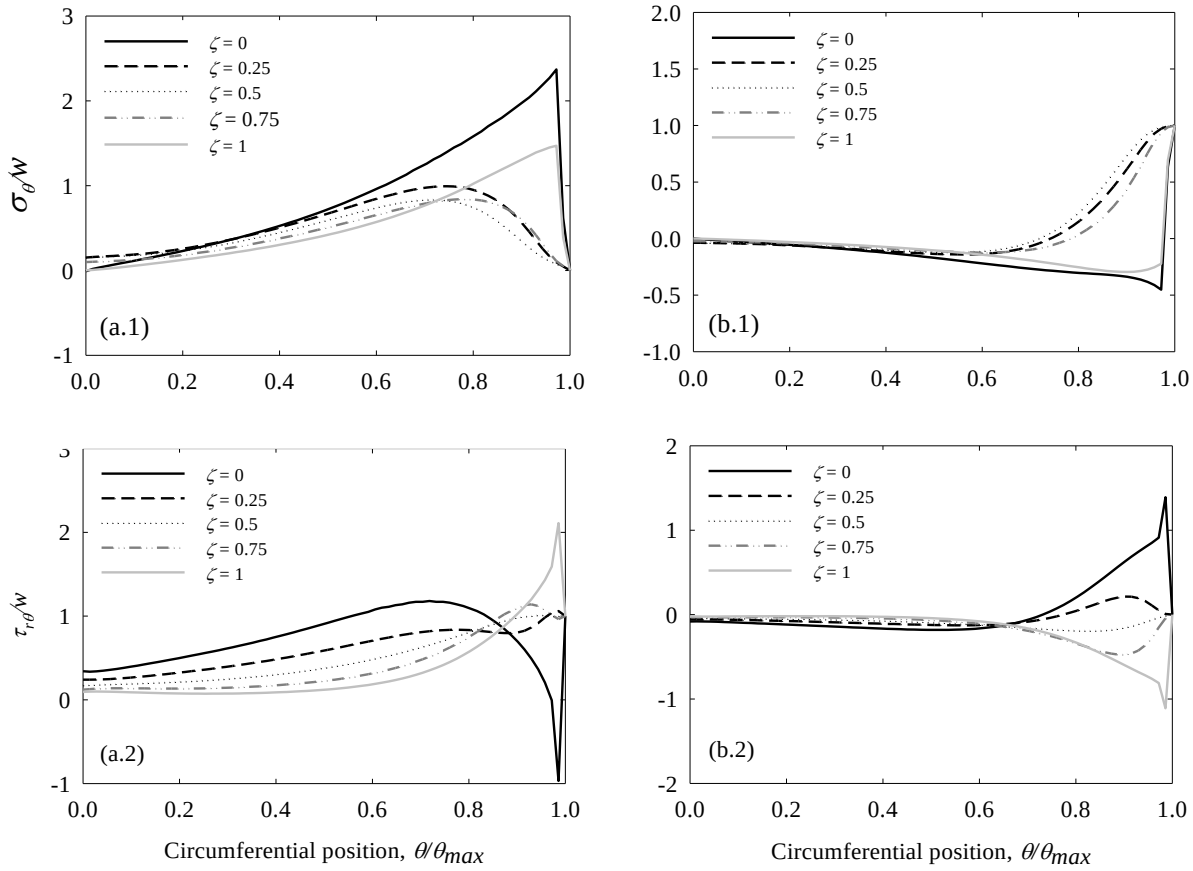


**Figure 5.12:** Distributions of stress components at various radial sections of the curved beam ($r_o/r_i$ = 1.5): (a) shear loading; (b) tensile loading.

Fig. 5.12(a.1) describes the distribution of the tangential stress along the circumferential position of the beam for under shear loading case. From the distributions, the maximum tangential stress is found to occur at the inner circumference of the beam followed by the outer circumference. The maximum stress occurs at a section just before the radial loaded end, the value of which is nearly 2.4 times the applied shear loading. The value of tangential stress at the loaded end is found to be zero, which satisfies one of the applied boundary

conditions at this end. Fig. 5.12 (b.1) shows the similar distributions for case-II. In this case the value of tangential stress at the loaded end is unity, which matches exactly with the applied loading condition. Fig. 5.12(a.2) and 5.12(b.2) show the distribution of shear stress along the circumferential positions of the beam for case-I and case-II, respectively. It is seen from the distributions that, for case-I, maximum shear stress occurs at the outer circumference of the beam, whereas, for case-II, maximum shear stress occurs at the inner circumference of the beam. Shear stress at the upper radial surface is found to be unity and zero for case-I and case-II respectively, which is in good agreement with applied loading.

### 5.3.4 Effect of beam thickness

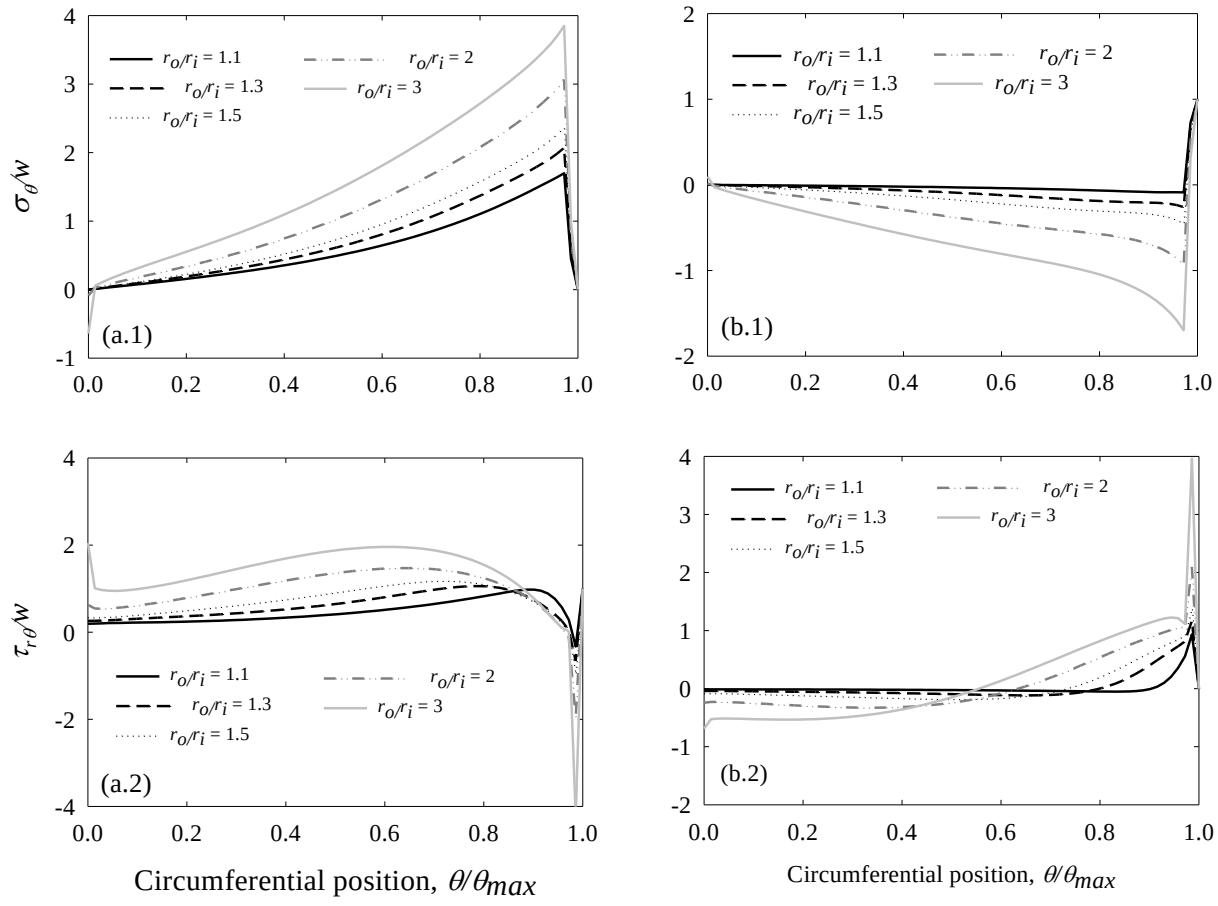


**Figure 5.13:** Effect of beam thickness on the stress distribution at stiffened sections: (a) shear loading (b) tensile loading.

The effect of beam thickness on the distribution of circumferential and shear stresses at the stiffened sections is described in this section. This effect is realized in terms of a ratio of outer radius to inner radius, and the results are shown for five different bar thicknesses ranging from 1.1 to 3.0. Here, the inner circumference has been chosen as the section of interest to demonstrate the effect for all the thickness ratios, as it has been identified as the most critical section of the bar in terms of stresses except for shear stresses in case-I.

Figure 5.13(a.1) and 5.13(b.1) demonstrate the effect of beam thickness on the distribution of circumferential stress for case-I and case-II respectively. From the figures it can be seen that the values of tangential stress increase with the increase of the beam thickness for both shear and tensile loading conditions. Shear stress distributions are also found to experience the similar effect of beam thickness as observed from figures 5.13(a.2) and 5.13(b.2). In this case, concentration of stress is observed just before the loaded end of the bar, the intensity of which is however found to increase for higher thickness ratios.

## 5.4 CONCLUSIONS

Two classical problems of solid mechanics have been analyzed using the present displacement potential formulation. In case of the both-ends-fixed beam problem the solutions are compared with the available numerical solution. All the comparisons show a very good agreement between the present displacement potential method (DPM) solution and other available solutions. The effect of beam curvature and the deformed shape of the both-ends-fixed beam have also been described using the present DPM solution. For the stiffened curved beam problem, it is observed that the beam becomes more critical in terms of stresses under shear loading compared to that under tensile loading of identical intensity. More importantly, both the circumferential and shear stresses are found to be more or less equally dominant in defining the overall state of stress at the stiffened edges, which is however not the case for straight beams. In that case, shear stress is found to be mainly responsible to describe the corresponding stress state. Finally, both the shear and tangential stresses at the stiffened edges are found to vary quite significantly by the aspect ratio of the curved beam.

Chapter 06

# ANALYSIS OF DEEP ARCHES

## 6.1 INTRODUCTION

An arch is a structure that spans a space and supports structure and weight above it. Arches have many forms, but all fall into three basic categories: Circular, pointed, and parabolic. The semicircular arch is among the most popular arch forms used by designers today. Its smooth, continuous curve makes it easily adaptable to various styles and applications. Usually these arches carry compressive loads. Today arches are mainly made of steel or of reinforced or pre-stressed concrete and can support both tensile as well as compressive loads. In this chapter, using the present displacement potential method (DPM), two semi-circular arch problems have been solved numerically. In order to obtain the numerical results of the problems, values for Young's modulus and Poisson's ratio of 207 GPa and 0.29, respectively, are used. Problem-I is an example of a deep semi-circular arch problem. The arch considered here is simply supported at both ends and is subjected to the action of uniform radial pressure over a certain portion (21%) of its angular span at the convex surface of the arch. In this case, the ratio of the outer to inner radius is $r_o/ r_i = 1.25$. Problem-II is another example of a deep semi-circular arch problem, but in this case the arch considered is fixed at both ends and under the action of uniform radial pressure over a certain portion of its angular span at the convex surface of the arch. In this case, the ratio of the outer to inner radius is $r_o/ r_i = 1.25$. Solutions of stresses and displacements of both the problems are presented along different radial and circumferential sections of the arch. Effect of curvature is also considered for the analysis of the problems.

## 6.2 SEMI-CIRCULAR DEEP ARCH WITH SIMPLE SUPPORTS

A semi-circular simply supported deep arch is considered as the first problem of this chapter to demonstrate the capability of the present mathematical and numerical modeling to solve arch problems. The arch considered here has the ratio of the outer to inner radius, $r_o/ r_i = 1.25$ and the angular span $180^o$. It is simply supported at both ends and under the action of uniform

radial pressure over 21% of its angular span applied symmetrically from the mid-span at the convex surface of the arch. The geometry and loading condition of the arch are shown in Fig. 6.1.

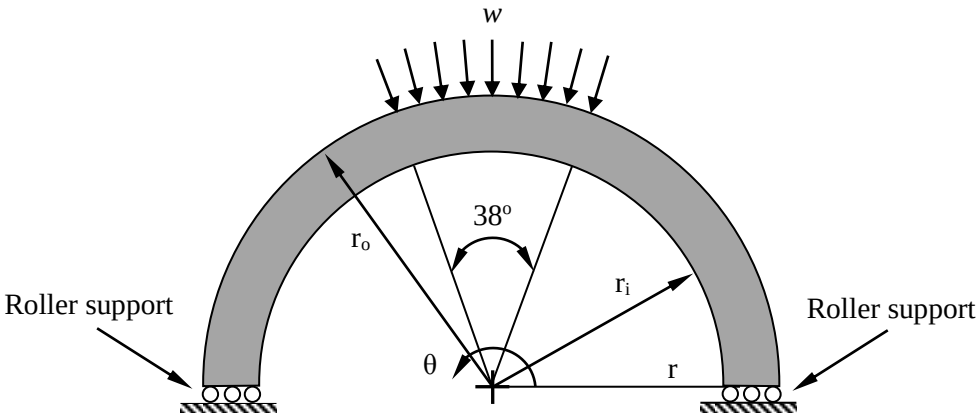


**Figure 6.1:** Geometry and loading of the semi-circular simply supported arch.

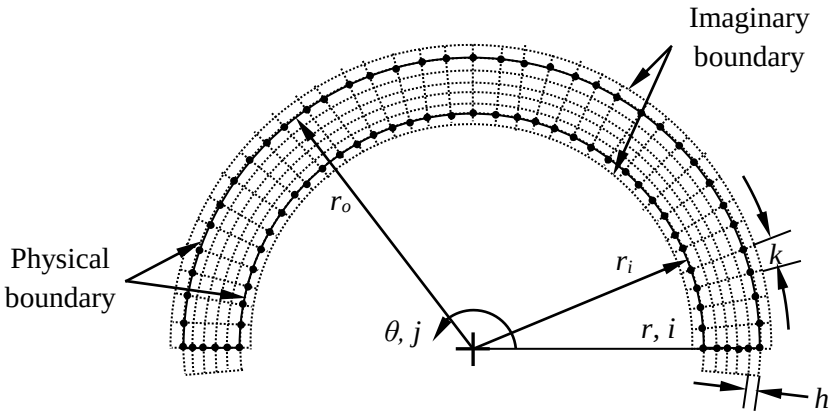


**Figure 6.2:** Discretization of the semi-circular deep arch.

A uniform curvilinear finite difference mesh network of (45×55) nodes is used to solve the problem (Fig. 6.2). The mathematical conditions used to model the actual physical conditions at the two radial and two circumferential surfaces of the arch are described in Table 6.1. In this case, no special care is necessary to model the four corner points of the arch as there are only three conditions available at each corner point due to the common zero shear stress condition from each side of the corner points.

Table- 6.1

Boundary conditions used for the semi-circular simply supported deep arch for obtaining the present solution

| Problem | Boundary | Boundary conditions | |
|---|---|---|---|
| | | Normal component | Tangential component |
| Semi-circular simply supported deep arch (Fig. 6.1) | Right radial surface, $\theta=0^o$ | $u_\theta(r, 0)=0$ | $\tau_{r\theta}(r, 0)=0$ |
| | Left radial surface, $\theta= \theta_{max}$ | $u_\theta(r, \theta_{max})=0$ | $\tau_{r\theta}(r, \theta_{max})=0$ |
| | Outer circumferential surface, $r=r_o$ | $\sigma_r(r_o,\theta)=\begin{cases}-w & (71^o \le \theta \le 109^0) \\ o & \text{(otherwise)}\end{cases}$ | $\tau_{r\theta}(r_o, \theta)=0$ |
| | Inner circumferential surface, $r=r_i$ | $\sigma_r(r_i, \theta)=0$ | $\tau_{r\theta}(r_i, \theta)=0$ |

### 6.2.1 Distribution of displacement components

This section describes the distribution of displacement components at different sections of the arch as obtained from the new displacement potential formulation (Formulation-I). In the case of present problem, displacement components are normalized with respect to the beam thickness ($r_o$-$r_i$). The distribution is presented along both circumferential and radial position of the arch. To identify the results of tangential layers at different radial positions, a radial function is defined as, $\xi = (r\text{-}r_i)/(r_o\text{-}r_i)$; $\xi = 0$ and 1 refer to the inner and outer edges of the curved beam, respectively. For distributions along radial positions, five different radial layers have been considered with angular positions as, $\theta = 0^o$, $45^o$, $95^o$, $150^o$ and $180^o$.

Fig. 6.3(a1) describes the distribution of radial displacement along the circumferential position of the arch. Distributions for five different tangential layers have been considered with the value of radial function $\xi = 0$, 0.25, 0.5, 0.75 and 1.0. From the distribution the radial displacement is found to be the maximum at the mid-circumferential position of the arch where the radial is applied. The distribution for different tangential layers is found to be very similar and in fact no significant difference can be observed in terms of nature of variation and value from this graph. This small difference is due to the small thickness of the arch compared to its inner and outer radius. Fig. 6.3(b1) shows the distribution of radial displacement along radial location of the arch. For all the sections radial displacement is also

found to be almost constant throughout the radial location of the arch and the maximum radial displacement is observed at mid-circumferential location ($\theta = 90^o$) of the arch.

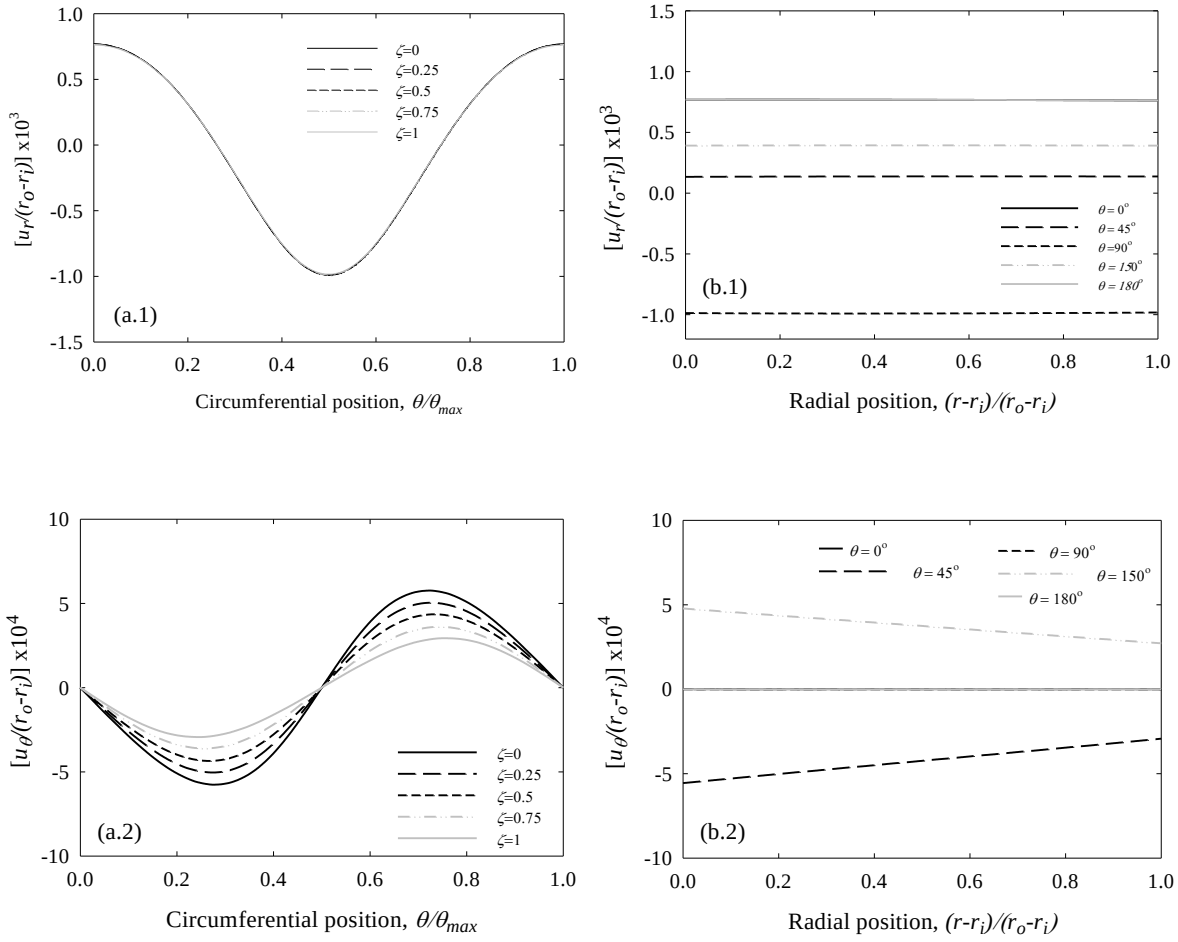


**Figure 6.3:** Distribution of displacement components of the deep simply supported arch along (a) circumferential position, (b) radial position.

Fig. 6.3(a2) and (b2) shows the distribution of tangential displacement along the circumferential and radial locations respectively. At both the simply supported ends the tangential displacement is found to be zero which is in complete agreement with the applied boundary condition [Table 6.1]. The distribution is found to be symmetric about the mid-circumference of the arch with a zero tangential displacement at this position. This is also in a good agreement with the expected solution, as the problem is symmetric about the mid-circumference of the arch both in terms of geometry and boundary conditions.

### 6.2.2 Distribution of stress components

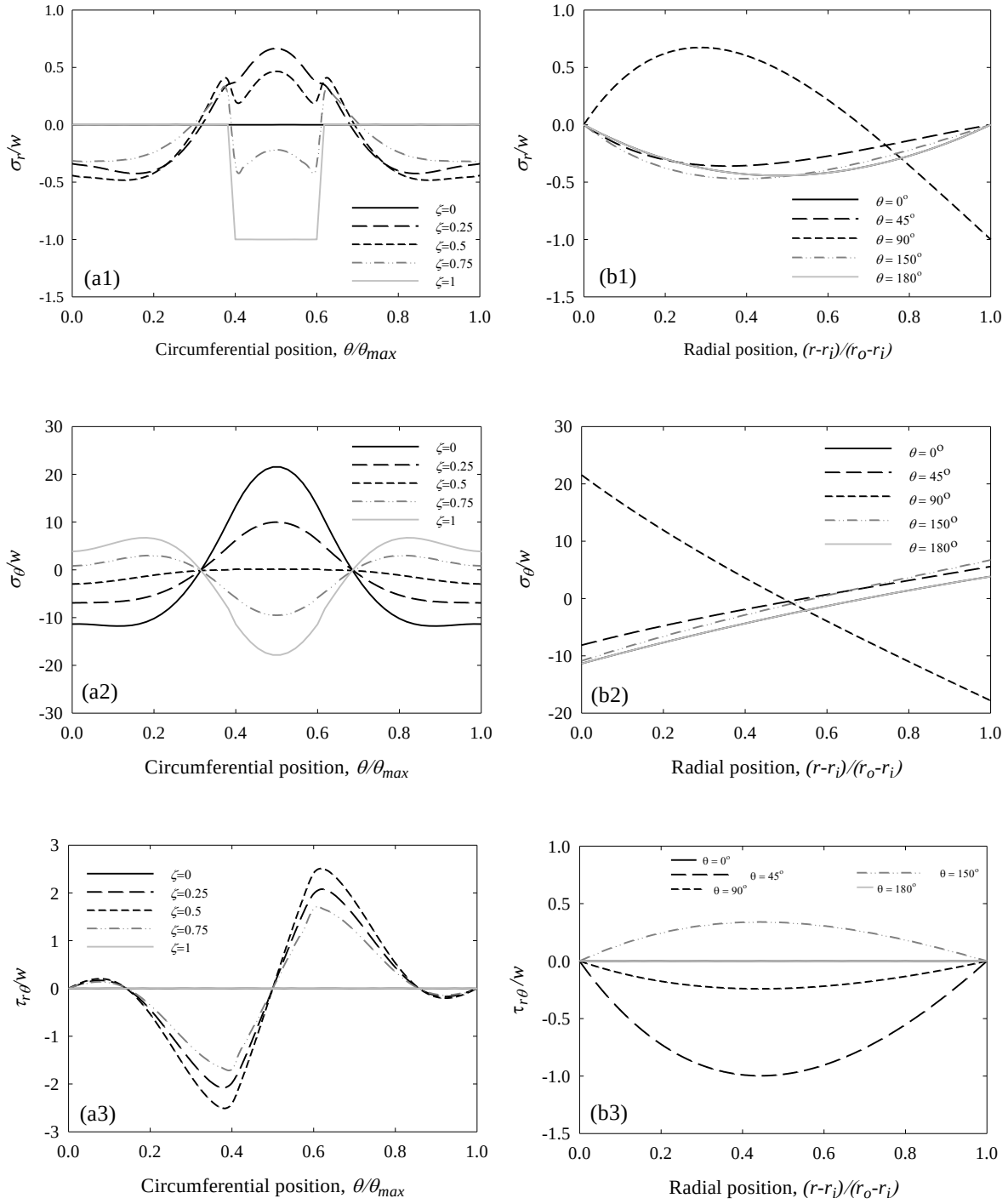


**Figure 6.4:** Distribution of (a1) radial stress along circumferential position, (b1) radial stress along radial position, (a2) tangential stress along circumferential position, (b2) tangential stress along radial position, (a3) shear stress along circumferential position, (b3) shear stress along radial position.

This section describes the distribution of stress components at different sections of the arch. Here, stress components are normalized with respect to the applied loading parameter, *w*. The distribution is presented along both circumferential and radial position of the arch. Different tangential and radial layers are identified in the similar manner as in the case of displacement components.

Fig. 6.4(a1) and (b1) describe the distribution of radial stress along the circumferential and radial locations of the simply supported arch respectively. Both the figures show zero radial stress at the inner and outer circumference of the arch except the region under loading where the radial stress is equal to the applied loading. This is in perfect match with the applied boundary condition [Table 6.1]. It is also observed that radial stress is small compared to the applied loading for rest of the regions of the arch.

Fig. 6.4(a2) describes the distribution of tangential stress along the circumferential position of the simply supported arch. For the layers with $\xi$ = 0, 0.25 and 0.5, the arch is found to be under compression for the regions near the simple support (almost 32% of the circumference from each end) and under tension for the regions near the mid circumference. For rest of the tangential layer vice-versa is observed. Maximum stress is found at the inner circumference of the arch.

Fig. 6.4(b2) describes the distribution of tangential stress along the radial position of the arch. Tangential stress is found to change from compression to tension from inner to outer radius of the arch for all the sections except the section at $\theta = 90^o$ where the tangential stress is found to change from tension to compression from inner to outer radius of the arch. Maximum tangential stress is found to occur at the $\theta = 90^o$ section with a value more than 20 times of the applied loading at the inner circumference of the arch.

Fig. 6.4(a3) and (b3) describes the distribution of shear stress along the circumferential and radial position of the simply supported arch. From both the graphs the shear stress is found to be zero at the inner and outer circumference of the arch. This is in full conformity with the applied boundary condition at these two ends [Table 6.1]. Again the distribution is found to be symmetric about the mid-circumference of the arch with zero shear stress at the axis of symmetry likewise the case of tangential displacement which is the due to the symmetric nature of the problem about the mid-circumference of the arch. Moreover maximum shear stress is found to occur at the layer with $\xi = 0.5$ near the section with $\theta = 70^o$ and $110^o$.

### 6.2.3 Effect of curvature

This section describes the effects of curvature on the distribution of tangential stress component. The effect of curvature on the distribution has been shown for both along circumferential location and radial location of the arch. For distribution along circumference of the arch, inner circumference has been chosen as the section of interest as it has been identified as the tangential layer with maximum tangential stress (Fig. 6.3(a2)). For distribution along radial position, $\theta = 90^o$ section has been chosen as the section of interest to demonstrate the effect as it has been identified as the most critical section of the beam in terms of tangential stress (Fig. 6.3 (b2)). This effect is realized in terms of a curvature parameter $C_r$ which is defined by the following relation:

$$C_r = \int_{r_i}^{r_o} \frac{1}{r} dr$$

The results have been shown for five different values of $C_r$ ranging from 0.26 to 1.09. It is important to mention here that the thickness of the arch is kept constant for all five cases of different curvature values.

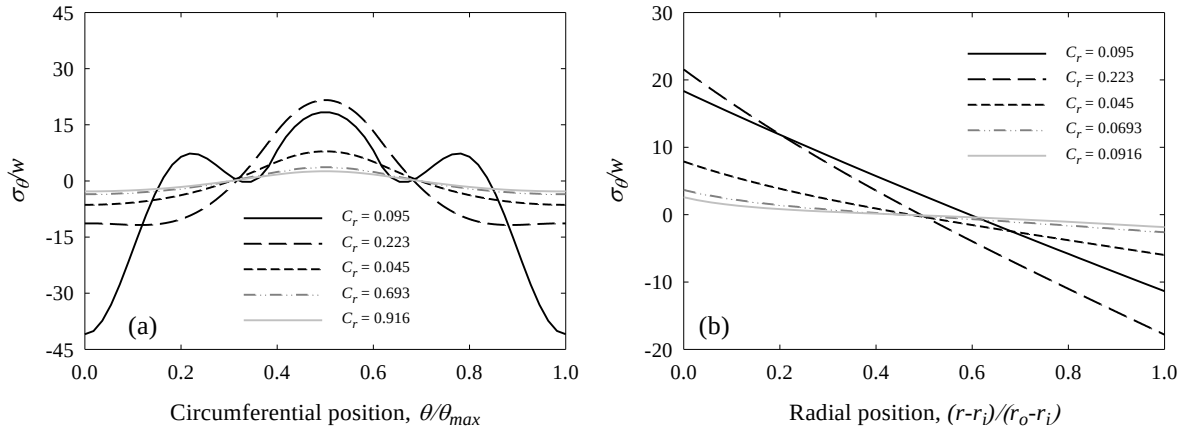


**Figure 6.5:** Effect of curvature on the distribution of tangential stress along (a) circumferential position at the inner circumference, (b) radial position at $\theta = 90^o$ section.

Fig. 6.5(a) describes the effect of curvature on the distribution of tangential stress along the circumferential location of the arch at the inner circumference. With a decrease of curvature, the tangential stress is found to increase throughout the circumference of the arch for all the

cases except the one with $C_r$ = 0.095. In this case, tangential stress is found to decrease at the mid-circumferential region though significantly increases at both the ends of the arch. Finally, maximum value of tangential stress at the mid-circumference is found to be more than 20 times the applied loading, whereas more than 40 times the applied loading at the simply supported ends of the arch.

Fig. 6.5(b) describes the effect of curvature on the distribution of tangential stress along the radial location at $\theta = 90^o$ section of the arch. Likewise the previous figure, tangential stress is found to increase with decrease in curvature of the arch in all cases except the case with $C_r$ = 0.095 where the tangential stress is found to decrease with respect to the previous lower curvature arch ($C_r$ = 0.223). Finally maximum tangential stress is found to occur at the inner circumference of the arch which is more than 20 times the applied loading.

### 6.2.4 Deformed shape of the semi-circular simply supported deep arch

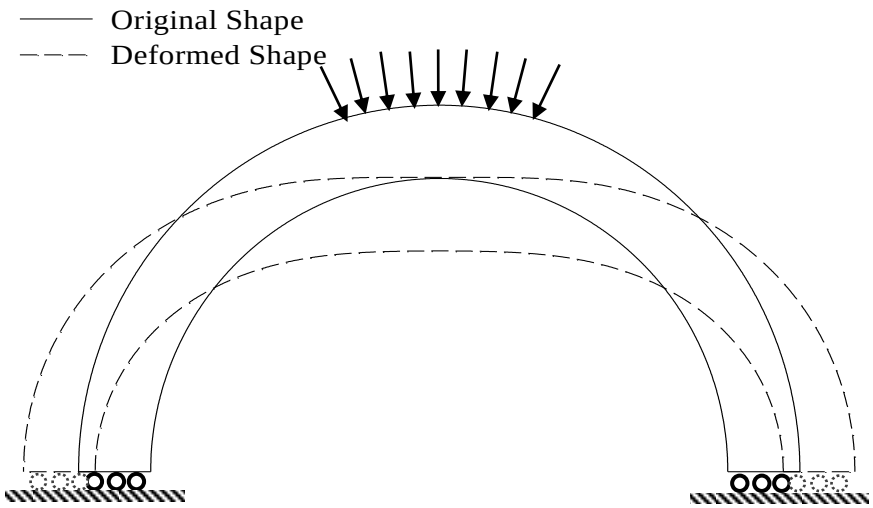


**Figure 6.6:** Original and deformed shape of the semi-circular simply supported deep arch (magnification factor = 1000).

Fig. 6.6 shows the original and deformed shapes of the semi-circular simply supported deep arch. The deformation is 1000 times magnified to make the deformation observable. Major change in shape is observed at the regions near the mid-circumference of the arch which is under the action of uniformly distributed radial pressure. The two roller supported ends are

found to move from its original position. Finally, the deformed shape of the beam is found to be symmetrical about the mid-circumference likewise the original shape of the beam.

## 6.3 SEMI-CIRCULAR DEEP ARCH WITH BUILT-IN SUPPORTS

A semi-circular deep arch with fixed-fixed end condition is considered as the second problem of this chapter. The arch considered here has the ratio of the outer to inner radius, $r_o / r_i = 1.5$ and the angular span $180^o$. It is rigidly fixed at both ends and under the action of uniform radial pressure over 21% of its angular span applied symmetrically from the mid-span at the convex surface of the arch. The geometry and loading condition of the arch are shown in figure 6.7.

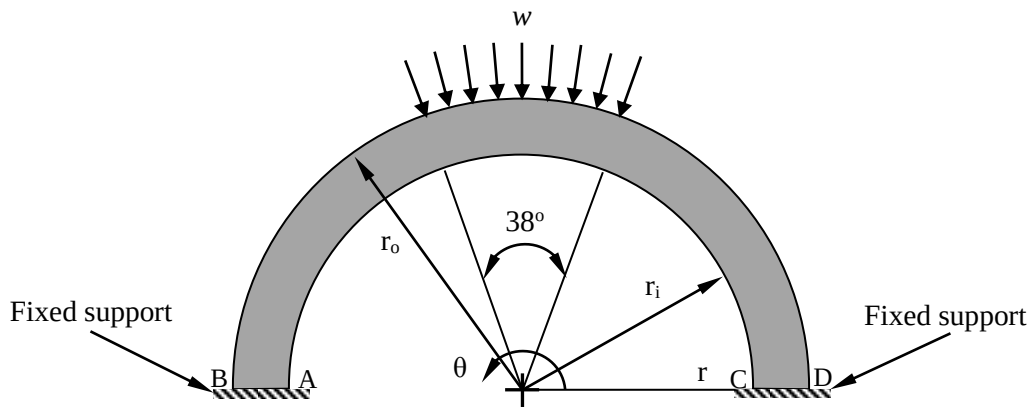


**Figure 6.7:** Geometry and loading of the semi-circular both-ends-fixed deep arch.

A uniform curvilinear finite difference mesh network of (45×55) nodes is used to solve the problem (Fig. 6.2). The mathematical conditions used to model the actual physical conditions at the two radial and two circumferential surfaces of the arch are described in Table 6.2. Special cares have been taken to model the boundary conditions at the four corner nodes of the beam, the details of which are illustrated in Table 6.3.

Table 6.2

Boundary conditions used for the both-ends-fixed semi-circular deep arch for obtaining the present solution

| Problem | Boundary | Boundary conditions | |
|---|---|---|---|
| | | Normal component | Tangential component |
| Both-ends-fixed semi-circular arch (Fig. 6.7) | Right radial surface, $\theta=0^o$ | $u_r(r, 0)=0$ | $u_\theta(r, 0)=0$ |
| | Left radial surface, $\theta= \theta_{max}$ | $u_r(r, \theta_{max})=0$ | $u_\theta(r, \theta_{max})=0$ |
| | Outer circumferential surface, $r=r_o$ | (i) $\sigma_r(r_o, \theta)=-w$; for loaded portion, (ii) $\sigma_r(r_o, \theta)=0$; for unloaded portion | $\tau_{r\theta}(r_o, \theta)=0$ |
| | Inner circumferential surface, $r=r_i$ | $\sigma_r(r_i, \theta)=0$ | $\tau_{r\theta}(r_i, \theta)=0$ |

Table 6.3

Boundary condition modeling for the corner points of the both-end-fixed semi-circular deep arch

| Corner point* | Given boundary conditions | Used conditions | Correspondence between mesh-points and given boundary conditions | |
|---|---|---|---|---|
| | | | Mesh point on the physical boundary | Mesh point on the imaginary boundary |
| A | $[(u_n, u_t), (\sigma_n, \sigma_t)]$ | $[u_n, u_t, \sigma_t]$ | $u_\theta=0$ | $u_r=0, \tau_{r\theta}=0$ |
| B | $[(u_n, u_t), (\sigma_n, \sigma_t)]$ | $[u_n, u_t, \sigma_t]$ | $u_\theta=0$ | $u_r=0, \tau_{r\theta}=0$ |
| C | $[(u_n, u_t), (\sigma_n, \sigma_t)]$ | $[u_n, u_t, \sigma_t]$ | $u_\theta=0$ | $u_r=0, \tau_{r\theta}=0$ |
| D | $[(u_n, u_t), (\sigma_n, \sigma_t)]$ | $[u_n, u_t, \sigma_t]$ | $u_\theta=0$ | $u_r=0, \tau_{r\theta}=0$ |

* Refer to Figure 6.7.

### 6.3.1 Distribution of displacement components

This section describes the distribution of displacement components at different sections of the arch as obtained from the new displacement potential formulation (Formulation-I). In the case of present problem, displacement components are normalized with respect to the beam thickness ($r_o$-$r_i$). The distribution is presented along both circumferential and radial position of the arch. To identify the results of tangential layers at different radial positions, a radial function is defined as, $\xi = (r\text{-}r_i)/(r_o\text{-}r_i)$; $\xi = 0$ and 1 refer to the inner and outer edges of the curved beam, respectively. For distributions along radial positions, five different radial layers have been considered with angular positions as, $\theta = 0^o$, $45^o$, $95^o$, $150^o$ and $180^o$.

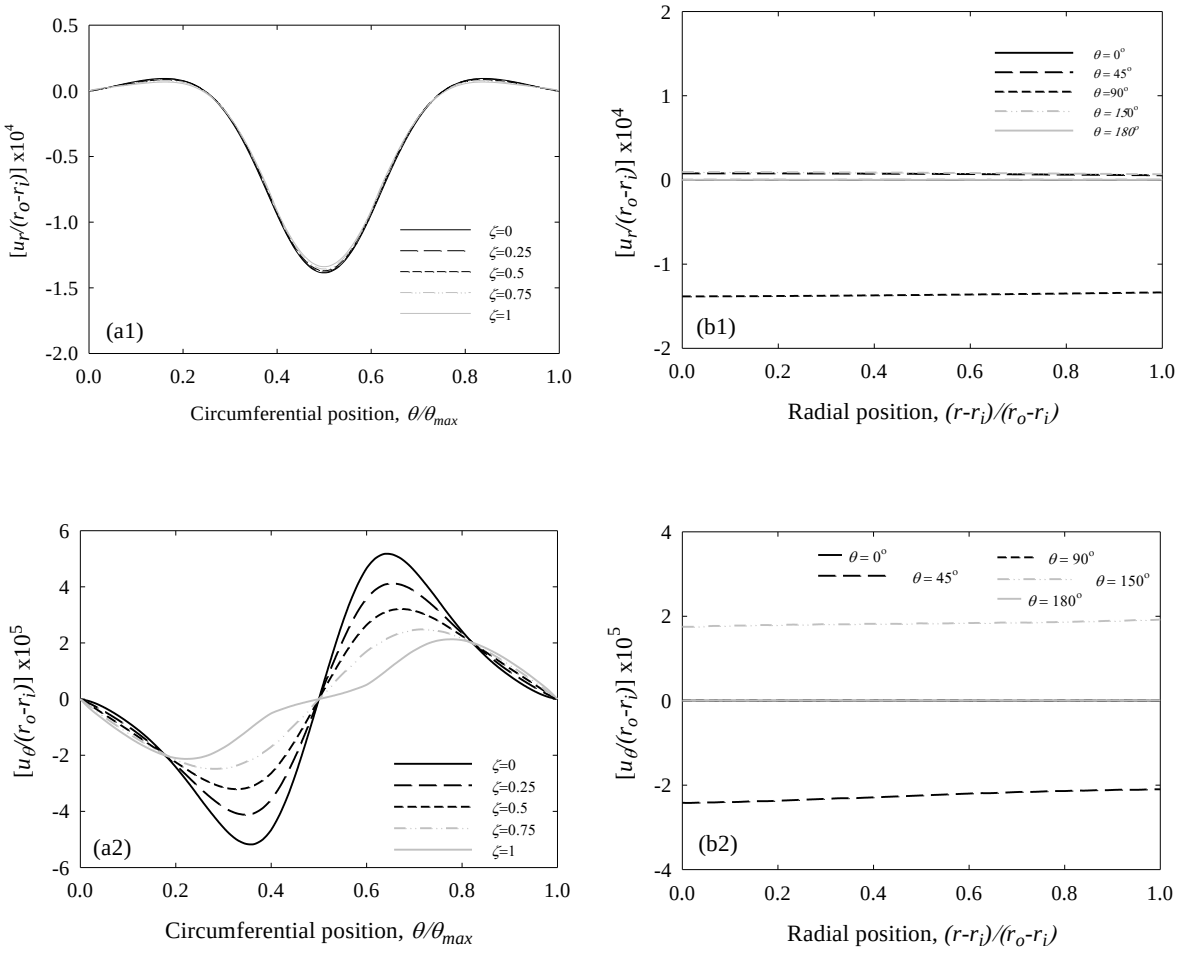


**Figure 6.8:** Distribution of displacement components of the both-ends-fixed deep arch along (a) circumferential position, (b) radial position.

Fig. 6.8(a1) describes the distribution of radial displacement along the circumferential position of the arch. Distributions for five different tangential layers have been considered with the value of radial function $\xi$ = 0, 0.25, 0.5, 0.75 and 1.0. From the distribution the radial displacement is found to be the maximum at the mid-circumferential position of the arch where the radial is applied. The distribution for different tangential layers is found to be very similar and in fact no significant difference can be observed in terms of nature of variation and value from this graph. This small difference is due to the small thickness of the arch compared to its inner and outer radius. Fig. 6.8(b1) shows the distribution of radial displacement along radial location of the arch. For all the sections radial displacement is also found to be almost constant throughout the radial location of the arch and the maximum radial displacement is observed at mid-circumferential location ($\theta = 90^o$) of the arch. Finally both 6.8(a1) and (b1) shows zero radial displacement at the fixed end of the arch which actually proves the conformity of the solution with the given boundary conditions [Table 6.2].

Fig. 6.8(a2) and (b2) shows the distribution of tangential displacement along the circumferential and radial locations respectively. At both the fixed ends the tangential displacement is found to be zero which is in complete agreement with the applied boundary condition [Table 6.2]. Moreover the zero tangential displacement is observed at the mid circumferential location ($\theta = 90^o$) of the arch which represents the axis of symmetry for this problem. Finally the distribution of tangential displacement is found to be symmetric about this mid-circumferential section ($\theta = 90^o$) of the arch which is in a good agreement with the expected solution, as the problem is symmetric about the mid-circumference of the arch both in terms of geometry and boundary conditions.

### 6.3.2 Distribution of stress components

This section describes the distribution of stress components at different sections of the arch. Here, stress components are normalized with respect to the applied loading parameter, *w*. The distribution is presented along both circumferential and radial position of the arch. Different tangential and radial layers are identified in the similar manner as in the case of displacement components.

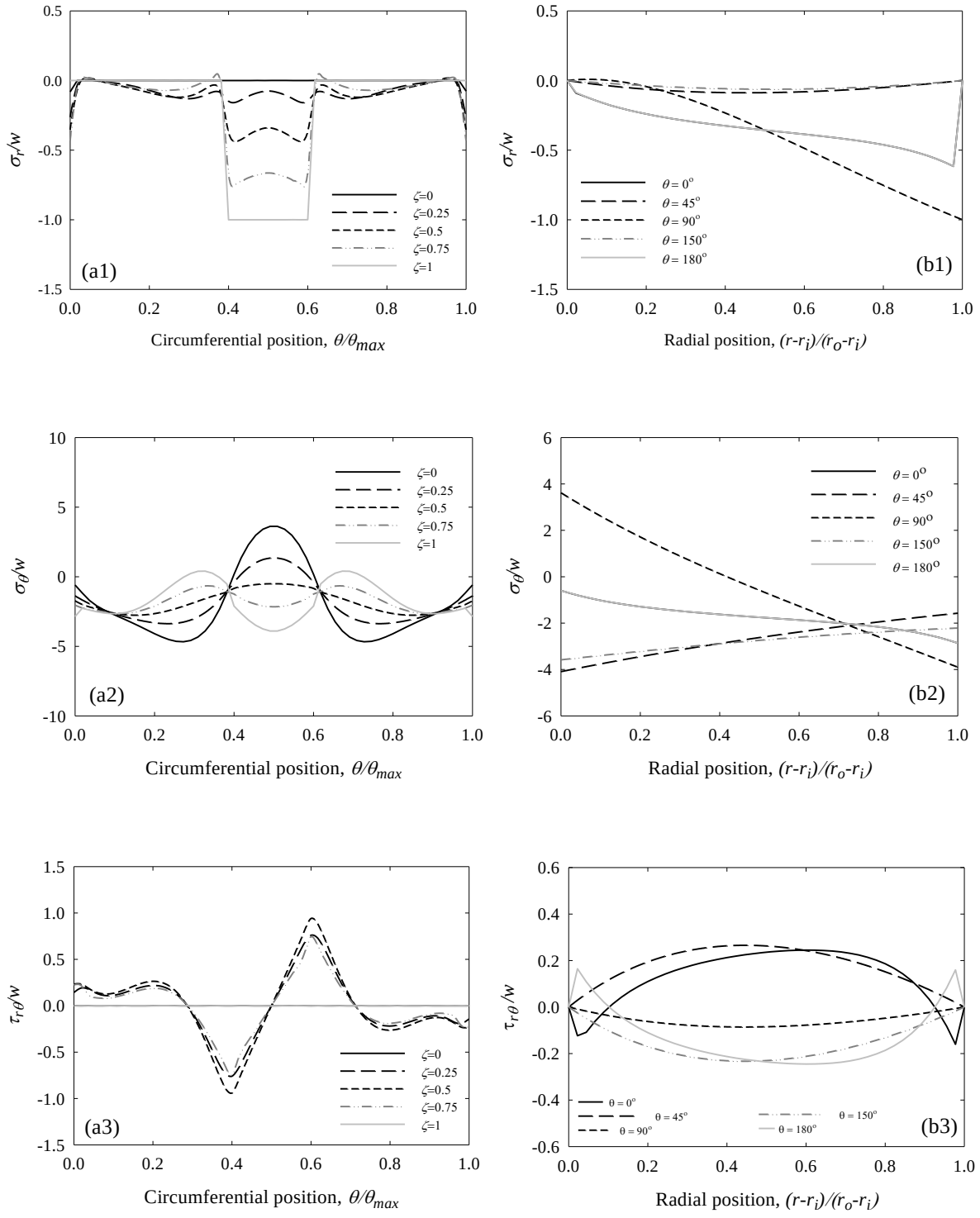


**Figure 6.9:** Distribution of (a1) radial stress along circumferential position, (b1) radial stress along radial position, (a2) tangential stress along circumferential position, (b2) tangential stress along radial position, (a3) shear stress along circumferential position, (b3) shear stress along radial position.

Fig. 6.9(a1) and (b1) describe the distribution of radial stress along the circumferential and radial locations of the both-ends-fixed arch respectively. Both the figures show zero radial stress at the inner and outer circumference of the arch except the region under loading where the radial stress is equal to the applied loading. This is in perfect match with the applied boundary condition [Table 6.2]. It is also observed that radial stress is relatively small compared to the applied loading for rest of the regions of the arch.

Fig. 6.9(a2) describes the distribution of tangential stress along the circumferential position of the both-ends-fixed arch. Inner circumferential layer is found to be under maximum tangential stress followed by the outer circumferential layer. Rest of the tangential layers lie in-between these two layers. Moreover, the maximum value of tangential stress is almost 4.67 times the applied loading and found at an angular position about $51^o$ from either of the fixed ends. Finally the distribution is found to be symmetrical about the mid-circumference as expected.

Fig. 6.9(b2) describes the distribution of tangential stress along the radial position of the arch. Tangential stress is found to be compressive stress for all the sections except the section at $\theta = 90^o$ where the tangential stress is found to change from tension to compression from inner to outer radius of the arch. Among these five sections maximum tangential stress is found to occur at the $\theta = 45^o$ section with a value just less than 4 times the applied loading at the inner circumference of the arch.

Fig. 6.9(a3) and (b3) describes the distribution of shear stress along the circumferential and radial position of the both-ends-fixed deep arch. From both the graphs the shear stress is found to be zero at the inner and outer circumference of the arch. This is in full conformity with the applied boundary condition at these two ends [Table 6.2]. Again the distribution is found to be symmetric about the mid-circumference of the arch with zero shear stress at the axis of symmetry likewise the case of tangential displacement which is the due to the symmetric nature of the problem about the mid-circumference of the arch. Moreover maximum shear stress is found to occur at the layer with $\xi = 0.5$ near the section with $\theta = 74^o$ from either of the fixed ends. Finally the maximum value of the shear stress found from these graph is almost 0.94 times the applied loading parameter, $w$.

### 6.3.3 Effect of curvature

This section describes the effects of curvature on the distribution of tangential stress component. The effect of curvature on the distribution has been shown for both along circumferential location and radial location of the arch. For distribution along circumference of the arch, inner circumference has been chosen as the section of interest as it has been identified as the tangential layer with maximum tangential stress (Fig. 6.9(a2)). For distribution along radial position, $\theta = 45^o$ section has been chosen as the section of interest to demonstrate the effect as it has been identified as the most critical section of the beam in terms of tangential stress (Fig. 6.9(b2)). This effect is realized in terms of a curvature parameter $C_r$ which is defined by the following relation:

$$C_r = \int_{r_i}^{r_o} \frac{1}{r} dr$$

The results have been shown for five different values of $C_r$ ranging from 0.26 to 1.09. It is important to mention here that the thickness of the arch is kept constant for all five cases of different curvature values.

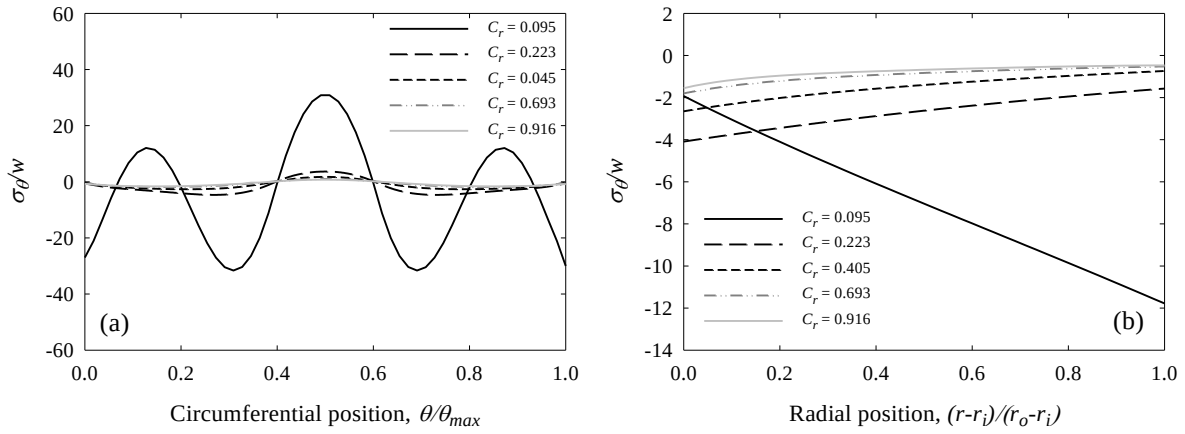


**Figure 6.10:** Effect of curvature on the distribution of tangential stress along (a) circumferential position at the inner circumference, (b) radial position at $\theta = 45^o$ section.

Fig. 6.10(a) describes the effect of curvature on the distribution of tangential stress along the circumferential location of the arch at the inner circumference. With a decrease of curvature, the tangential stress is found to increase throughout the circumference of the arch for all the cases. For the case with $C_r$ = 0.095, tangential stress is found to increase tremendously

compared to other cases. Moreover, the maximum value of tangential stress is found to be more than 31 times the applied loading at an angular position $\theta = 58^o$ form either of the fixed ends of the arch.

Fig. 6.10(b) describes the effect of curvature on the distribution of tangential stress along the radial location at $\theta = 45^o$ section of the arch. Likewise the previous figure, tangential stress is found to increase with decrease in curvature of the arch. Again the case with $C_r = 0.095$ shows a rapid increase of tangential stress with respect to the previous lower curvature arch ($C_r = 0.223$). Finally the maximum tangential stress is found to occur at the inner circumference for all the cases except the case with $C_r = 0.095$ where the maximum tangential is found to occur at the outer circumference of the arch which is almost 12 times the applied loading.

### 6.3.4 Deformed shape

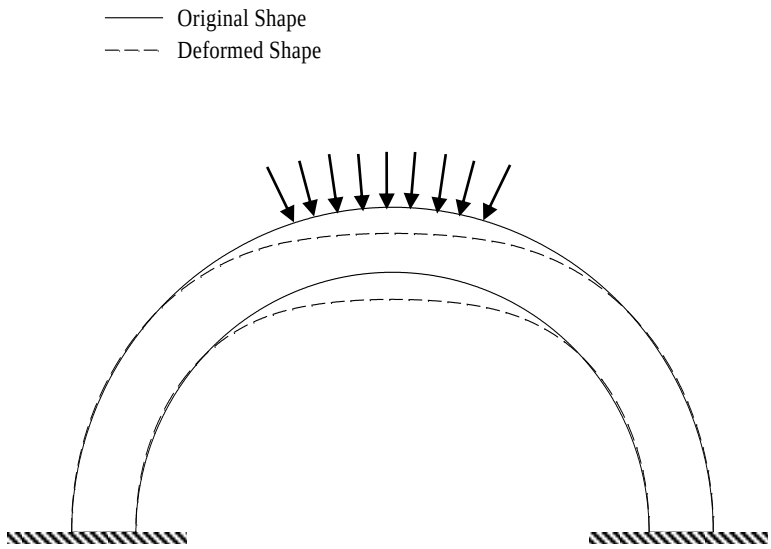


**Figure 6.11:** Original and deformed shape of the both-ends-fixed deep arch (magnification factor = 3000).

Fig. 6.11 shows the original and deformed shapes of the semi-circular both-ends-fixed deep arch. The deformation is 3000 times magnified to make it observable. Major change in shape is observed at the regions near the mid-circumference of the arch which is under the action of uniformly distributed radial pressure. The two fixed ends are found to have no deformation.

Moreover, the deformations near these fixed ends are found to be insignificant compared to the deformation found at the mid-circumference region. Finally, the deformed shape of the beam is found to be symmetrical about the mid-circumference likewise the original shape of the beam.

## 6.4 CONCLUSIONS

Two classical arch problems have been solved using the new displacement potential approach. For both the problems the results are found to meet all of the applied boundary conditions and symmetric conditions where required. Moreover the deformed shapes reveal a good insight about the finial condition of the geometry of the problem. Finally, an important effect of curvature is observed in case of both simply supported and both-ends-fixed deep arches which will be a very important guide for the design of this kind of structural members.

Chapter 07

# ANALYSIS OF CIRCULAR RINGS

## 7.1 INTRODUCTION

In large pipelines, tanks, aircraft, and submarines the circular ring is an important structural element, and for designing such elements it is often necessary to calculate the stresses and deformations produced in such a ring under various conditions of loading and support. In this chapter, using the present displacement potential method (DPM), one ring problem has been solved numerically. In order to obtain the numerical results of the problem, values for Young's modulus and Poisson's ratio of 207 GPa and 0.29, respectively, are used. The problem analyzed is an example of an open-ended stiffened ring problem. The ring considered here has a narrow rectangular cross section with circular axis, and is constrained at one end and the other end is under the action of uniformly distributed combined loading of shear and compression. The outer and inner circumferences of the ring are subjected to rigid circumferential stiffeners. In this case the ratio of the outer to inner radius is $r_o/ r_i = 1.5$ and the angular span of the ring is $350^o$.

## 7.2 OPEN ENDED STIFFENED RING

An open ended stiffened circular ring has been considered as the example to demonstrate the application of the present displacement potential solution in solving circular ring problem. The ring considered has a narrow rectangular cross section with the ratio of outer to inner radius ($r_o/r_i$) as 1.5. One of the ends of the ring is rigidly fixed and the other is subjected to a combined loading uniform tension and shear, as shown in Fig. 7.1. The inner and outer circumferences of the ring are stiffened by circumferential stiffeners. A uniform curvilinear finite difference mesh network of (61×71) nodes is used to solve the problem.

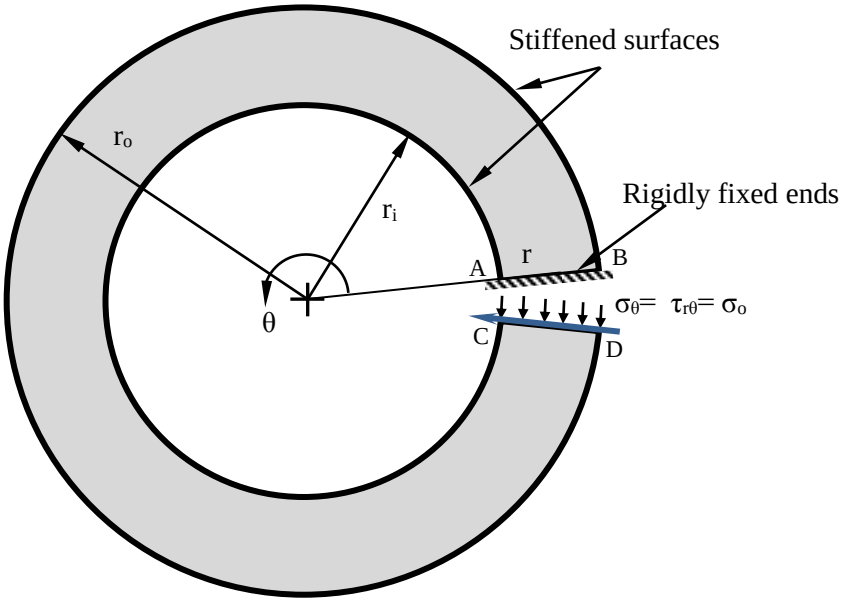


**Figure 7.1:** Geometry and loading of the open ended stiffened circular ring ($r_o/r_i$ = 1.5).

The mathematical conditions used to model the actual physical conditions at the radial and two circumferential surfaces of the ring are described in Table 7.1. The mixed boundary conditions associated with the stiffeners are modeled here by resisting the surfaces in terms of circumferential displacements and assigning zero value to the radial stress component. Special cares have been taken to handle the singularities at the four corner points of the ring, the details of which are summarized in Table 7.2.

Table 7.1

Boundary conditions used for the open ended stiffened ring for obtaining the present solution

| Problem | Boundary | Boundary conditions | |
|---|---|---|---|
| | | Normal component | Tangential component |
| Open ended stiffened ring (Fig. 7.1) | Upper radial surface, $\theta=0^o$ | $u_r(r, 0)=0$ | $u_\theta(r, 0)=0$ |
| | Lower radial surface, $\theta=\theta_{max}$ | $\sigma_\theta(r, \theta_{max})=-\sigma_o$ | $\tau_{r\theta}(r, \theta_{max})=-\sigma_o$ |
| | Outer circumferential surface, $r=r_o$ | $\sigma_r(r_o, \theta)=0$ | $u_\theta(r_o, \theta)=0$ |
| | Inner circumferential surface, $r=r_i$ | $\sigma_r(r_i, \theta)=0$ | $u_\theta(r_i, \theta)=0$ |

Table 7.2

Boundary condition modeling for the corner points of the open-ended stiffened circular ring problem

| Corner point* | Given boundary conditions | Used conditions | Correspondence between mesh-points and given boundary conditions | |
|---|---|---|---|---|
| | | | Mesh point on the physical boundary | Mesh point on the imaginary boundary |
| A | $[(u_n, u_t), (\sigma_n, u_t)]$ | $[u_n, u_t, \sigma_n]$ | $u_\theta=0$ | $u_r=0, \sigma_r=0$ |
| B | $[(u_n, u_t), (\sigma_n, u_t)]$ | $[u_n, u_t, \sigma_n]$ | $u_\theta=0$ | $u_r=0, \sigma_r=0$ |
| C | $[(\sigma_n, u_t), (\sigma_n, \sigma_t)]$ | $[u_t, \sigma_n, \sigma_t]$ | $\sigma_\theta=-\sigma_o$ | $u_\theta=0, \tau_{r\theta}=-\sigma_o$ |
| D | $[(\sigma_n, u_t), (\sigma_n, \sigma_t)]$ | $[u_t, \sigma_n, \sigma_t]$ | $\sigma_\theta=-\sigma_o$ | $u_\theta=0, \tau_{r\theta}=-\sigma_o$ |

* Refer to Fig. 7.1.

### 7.2.1 Distribution of the displacement components

This section describes the solution of displacement components obtained from the present displacement potential formulation (Formulation- II). Here, displacements are normalized with respect to the ring thickness ($r_o$-$r_i$).

Fig. 7.2(a) shows the distribution of the radial displacement along the circumferential axis of the ring. It is evident from the distribution that at the fixed end ($\theta/\theta_{max}$ = 0), radial displacement is zero and it remains nearly constant for more than 50% of its circumference for all the three sections considered. But for the last 40% of the circumference the displacement increases up to its maximum value at the loaded end ($\theta/\theta_{max}$ = 1). Moreover, no significant difference in the radial displacements at the inner and outer surfaces of the ring is observed, which is may be due to the fact that the thickness of the ring is not very high. Fig. 7.2(b) describes the distribution of the tangential displacement along the circumferential axis of the ring. It is observed from the distribution that tangential displacement is zero at both inner and outer circumference of the circular ring. This shows excellent agreement between the solution and the applied boundary condition as can be seen from Table 7.1.

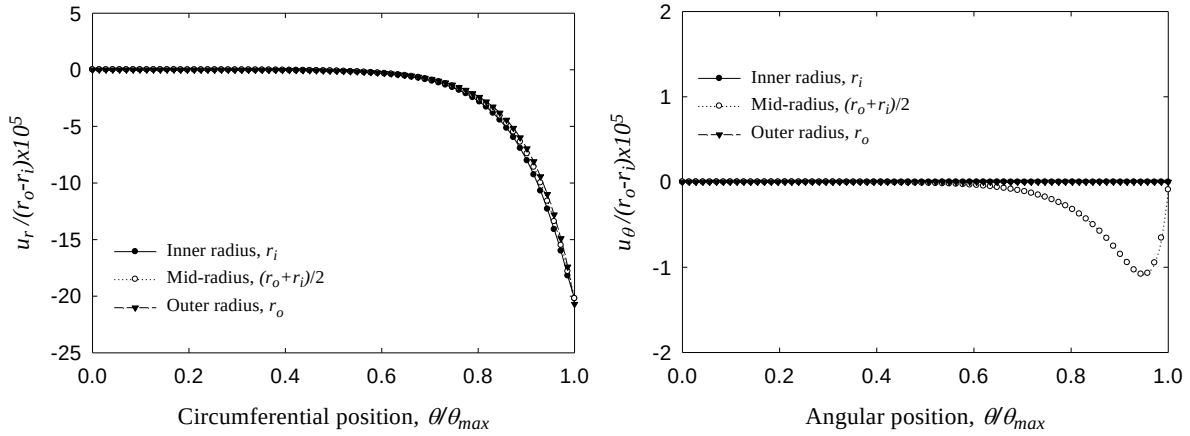


(a) (b)

**Figure 7.2:** Distribution of displacement components of the stiffened circular ring: (a) radial displacement, (b) tangential displacement.

### 7.2.2 Distribution of the stress components

This section describes the solution of stress components obtained from the present displacement potential formulation (Formulation-II). Here, the stresses are normalized with respect to the applied loading intensity, $\sigma_o$ (see Fig. 7.1).

Distribution of tangential and shear stresses along the circumferential axis of the ring is illustrated for three different radial locations in Fig. 7.3. As appears from Fig. 7.3(a), the value of the tangential stress is very small up to almost 60% of the circumference starting from the fixed end; after that it starts to increase rapidly for of the ring. As expected, the normalized tangential stress at the loaded end ($\theta/\theta_{max} = 1$) is found to be unity for all the three sections considered, which is in good conformity with one of the applied boundary conditions at this end. For any circumferential section especially for $\theta/\theta_{max} > 0.6$, the stiffened inner and outer circumferences assume the highest and lowest value of tangential stress, respectively. This is primarily due to the effect of curvature that decreases from the inner surface to the outer surface. A small region of stress concentration is observed at the inner corner region of the loaded end if the ring. The maximum value of tangential stress is observed at the inner circumference of the ring, which is nearly 1.7 times the applied normal loading.

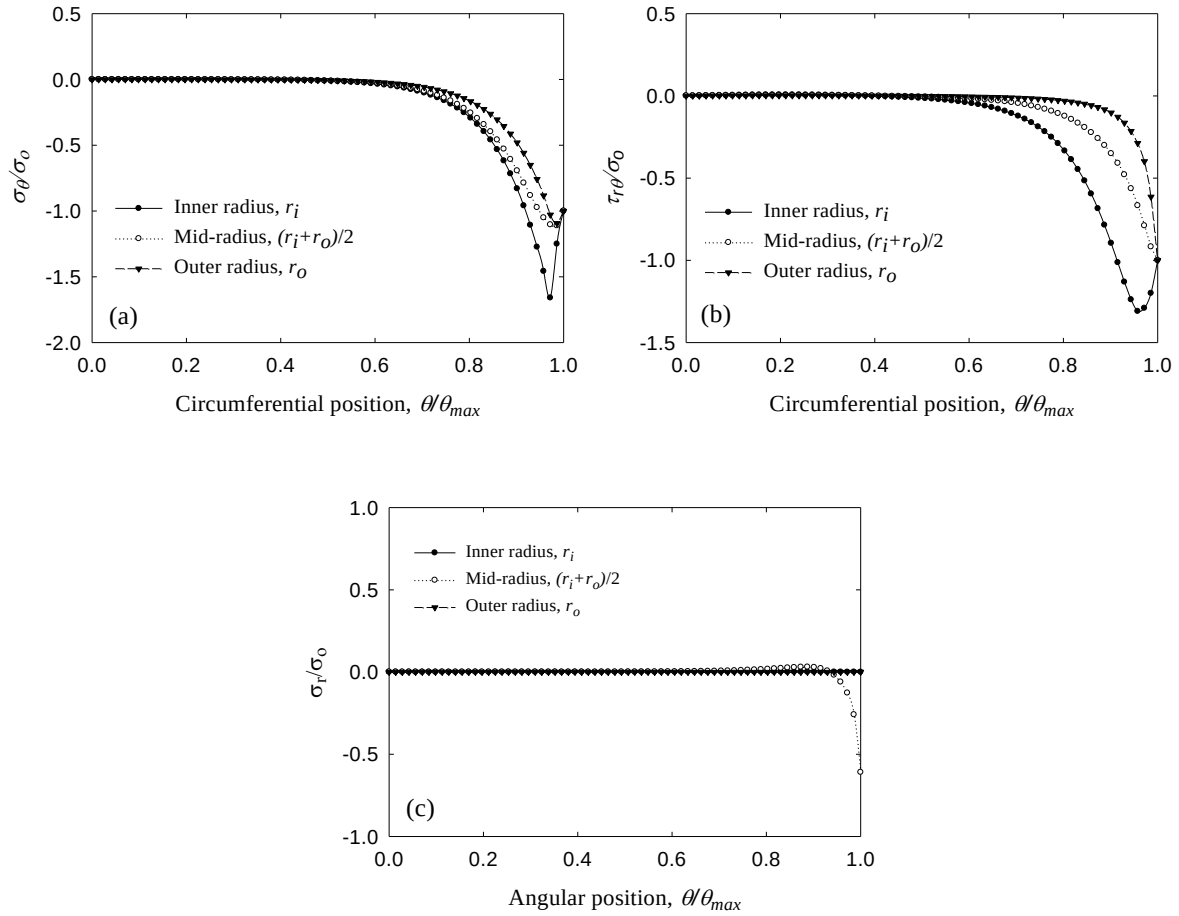


**Figure 7.3:** Distribution of stress components at different sections of the stiffened ring: (a) circumferential stress, (b) shear stress and (c) radial stress.

Fig. 7.3(b) shows the distribution of shear stress along the circumferential axis of the ring for the inner, mid-radial and outer surface. Likewise the case of tangential stress, shear stress is very small for more than 50% of the circumference starting from the fixed end and then increases for the remaining portion of the ring circumference. In case of the outer stiffened surface, the shear stress is found to be negligible for almost 80% of its length measured from the fixed end and then quickly rises to its highest value within the remaining portion of circumference. Again at the inner surface stress concentration occurs just before the loaded end and, in this case, the maximum value of shear stress is found to be 1.3 times the applied shear loading at the end. It is found that the value of the normalized shear stress at the loaded end is unity, which is in agreement with the applied boundary condition at this end. Finally, it can be mentioned here that, all the distributions of displacements and stresses are found to be in excellent agreement with the applied boundary conditions as well as intuitive predictions based on principles of mechanics. Fig. 7.3(c) describes the distribution of the radial stress

along the circumferential axis of the ring. It is observed from the distribution that radial stress is zero at both inner and outer circumference of the circular ring. This again shows very good agreement between the solution and the applied boundary condition as can be seen from Table 7.1.

### 7.2.3 Deformed shape

This section describes the deformed shape of the circular ring under combined normal and shear loading along with the original shape before the loading was applied.

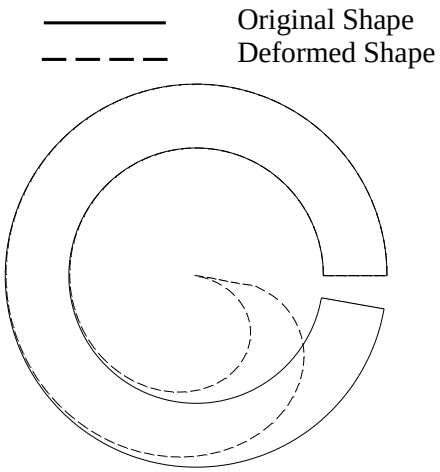


**Figure 7.4:** Deformed shape of the circular stiffened ring (magnification factor = 10000).

Fig. 7.4 shows the corresponding deformed shape in comparison with the original undeformed shape. The deformed shape of the ring verifies appropriate modeling of the boundary conditions used. The radial displacement component is found to play the dominant role in defining the deformed state of the ring, which is because of the fact that the ring is circumferentially stiffened at the two opposing circumferential surfaces. Even though both the circumferential and shear stress applied are of identical intensity, the influence of the shear loading is verified to be much higher for the present ring than that of circumferential loading.

## 7.3 CONCLUSIONS

A classical stress problem has been solved using the new displacement potential approach. The results are found to meet all of the applied boundary conditions where required. Distribution of stress and displacement shows a significant effect of stiffeners on the elastic field of the circular ring. Finally the deformed shape reveals a good insight about the finial condition of the geometry of the stiffened circular ring.

Chapter 08

# EFFECT OF STENCIL SIZE ON THE SOLUTION

## 8.1 INTRODUCTION

To analyze the effect of stencil size on the solution two versions of finite difference expression for different displacement and stress components is prepared. In this case smallest possible stencil is designed using a combination of finite difference expressions of different derivatives of O($h$) and O($h^2$). Both-ends-fixed beam problem solved in chapter 05 is considered here again to demonstrate the effect of stencil size on the DPM solution.

## 8.2 SMALLEST POSSIBLE FINITE DIFFERENCE EXPRESSIONS FOR DIFFERENT DISPLACEMENT AND STRESS COMPONENTS

For the radial component of displacement Eq. (2.23), four different versions of finite-difference expression have been developed for different regions of the boundary. These versions of finite difference expressions are obtained by adapting different combinations of forward and backward differencing scheme in both $r$ and $\theta$- directions . The finite-difference expressions so obtained are as follows:

a) $i$- forward, $j$- forward

$$u_r = a_1\psi(i+1, j+1) - a_1\psi(i+1, j) + (-a_1 + b_1)\psi(i, j+1) + (a_1 - b_1)\psi(i, j) \tag{8.1}$$

b) $i$- forward, $j$- backward

$$u_r = a_1\psi(i+1, j) - a_1\psi(i+1, j-1) + (-a_1 + b_1)\psi(i, j) + (a_1 - b_1)\psi(i, j-1) \tag{8.2}$$

c) $i$- backward, $j$- forward

$$u_r = (a_1 + b_1)\psi(i, j+1) - (a_1 + b_1)\psi(i, j) - a_1\psi(i-1, j+1) + a_1\psi(i-1, j) \tag{8.3}$$

d) *i*- backward, *j*- backward

$$u_r = (a_1 + b_1)\psi(i, j) - (a_1 + b_1)\psi(i, j-1) - a_1\psi(i-1, j) + a_1\psi(i-1, j-1) \tag{8.4}$$

where,

$$a_1 = -\frac{1+\nu}{2r_i hk},\ b_1 = \frac{5+\nu}{2r_i^2 k}$$

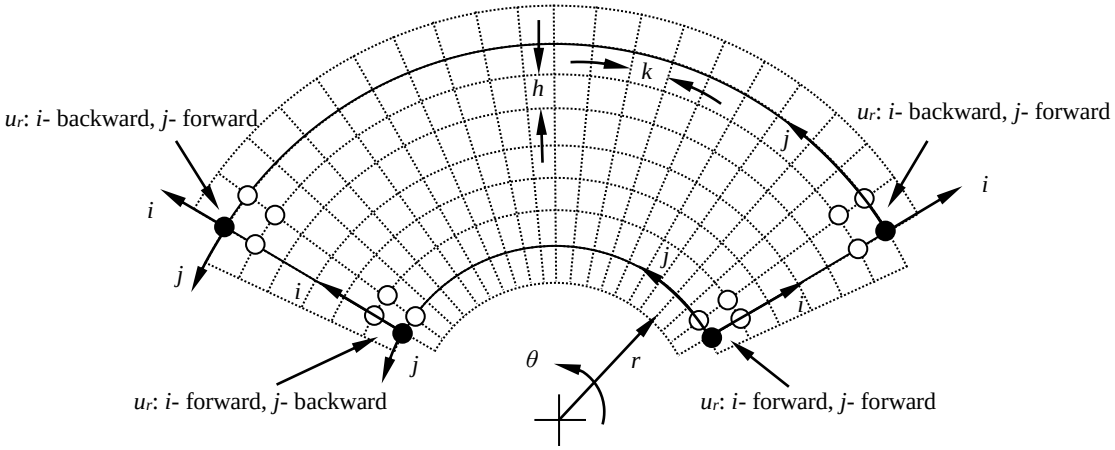


**Figure 8.1:** The smallest finite difference stencil for radial component of displacement ($u_r$) (Formulation-I).

Fig. 8.1 illustrates the above mentioned four stencils for normal component of displacement ($u_r$). It can be seen that each stencil consists of four nodal points and when applied to the boundary mesh points as shown in the figure includes no point exterior to the physical boundary.

For tangential component of displacement no new stencil is designed as the finite difference expression derived in equation (3.26) gives the smallest possible stencil for formulation-I.

Now, for the radial component of stress which is given by Eq. (2.24), two different finite-difference expressions has been developed using the combination of central, forward and backward differencing scheme which are illustrated in Fig. 8.2. Since the stencils have the symmetry about *j*- axis, two versions are sufficient to deal with all the body points involved. The expressions developed are:

a) *i*- central, *j*- forward

$$\begin{aligned}\sigma_r = {} & (A_1 + C_1)\psi(i+1, j+1) + (-A_1 - C_1)\psi(i+1, j) + B_1\psi(i, j+2) \\ & + (-2A_1 - 3B_1 + D_1)\psi(i, j+1) + (2A_1 + 3B_1)\psi(i, j) + (-B_1 - D_1)\psi(i, j-1) \\ & + (A_1 - C_1)\psi(i-1, j+1) + (-A_1 + C_1)\psi(i-1, j)\end{aligned} \tag{8.5}$$

b) *i*- central, *j*- backward

$$\begin{aligned}\sigma_r = {} & (A_1 + C_1)\psi(i+1, j) + (-A_1 - C_1)\psi(i+1, j-1) + (B_1 + D_1)\psi(i, j+1) \\ & + (-2A_1 - 3B_1)\psi(i, j) + (2A_1 + 3B_1 - D_1)\psi(i, j-1) - B_1\psi(i, j-2) \\ & + (A_1 - C_1)\psi(i-1, j) + (-A_1 + C_1)\psi(i-1, j-1)\end{aligned} \tag{8.6}$$

where,

$$A_1 = -\frac{G}{r_i h^2 k},\ B_1 = \frac{\nu G}{r_i^3 k^3},\ C_1 = \frac{(6+\nu)G}{2r_i^2 hk},\ D_1 = -\frac{(10+\nu)G}{2r_i^3 k}$$

The corresponding finite difference expressions for $\sigma_\theta$ which is given by Eq. (2.25) are developed following a procedure similar to that used for the case of $\sigma_r$, as the two differential equations are identical in terms of derivatives, but the differ only in terms of the coefficients. As a result, the finite difference stencils of $\sigma_r$ and $\sigma_\theta$ become identical in their appearance as shown in figure 8.2. The finite difference equations developed for $\sigma_\theta$ are as follows:

a) *i*- central, *j*- forward

$$\begin{aligned}\sigma_\theta = {} & (A_2 + C_2)\psi(i+1, j+1) + (-A_2 - C_2)\psi(i+1, j) + B_2\psi(i, j+2) \\ & + (-2A_2 - 3B_2 + D_2)\psi(i, j+1) + (2A_2 + 3B_2)\psi(i, j) + (-B_2 - D_2)\psi(i, j-1) \\ & + (A_2 - C_2)\psi(i-1, j+1) + (-A_2 + C_2)\psi(i-1, j)\end{aligned} \tag{8.7}$$

b) *i*- central, *j*- backward

$$\begin{aligned}\sigma_\theta = {} & (A_2 + C_2)\psi(i+1, j) + (-A_2 - C_2)\psi(i+1, j-1) + (B_2 + D_2)\psi(i, j+1) \\ & + (-2A_2 - 3B_2)\psi(i, j) + (2A_2 + 3B_2 - D_2)\psi(i, j-1) - B_2\psi(i, j-2) \\ & + (A_2 - C_2)\psi(i-1, j) + (-A_2 + C_2)\psi(i-1, j-1)\end{aligned} \tag{8.8}$$

where,

$$A_2 = \frac{G(2+\nu)}{r_i h^2 k},\ B_2 = \frac{G}{r_i^3 k^3},\ C_2 = -\frac{(7+2\nu)G}{2r_i^2 hk},\ D_2 = \frac{(11+2\nu)G}{2r_i^3 k}$$

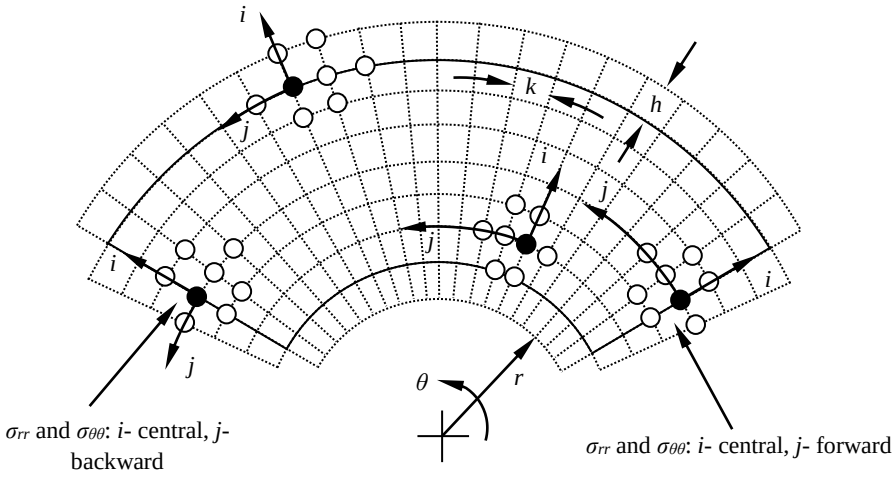


**Figure 8.2:** The smallest finite difference stencil for radial and tangential components ($\sigma_r$, $\sigma_\theta$) of stress (Formulation-I)

Again, for the shear stress component which is given by Eq. (2.26), two different finite-difference expressions have been developed using the combination of central, forward and backward differencing scheme. Since the stencils have the symmetry about *i*- axis, two versions are sufficient to deal with all the body points involved and are illustrated in figure 8.3. The expressions developed are:

a) *i*- forward, *j*- central

$$\begin{aligned}\tau_{r\theta} = {} & A_3\psi(i+2,j) + B_3\psi(i+1,j+1) + (-3A_3 - 2B_3 + C_3 + E_3)\psi(i+1,j) + B_3\psi(i+1,j-1) \\ & +(-B_3 + D_3)\psi(i,j+1) + (3A_3 + 2B_3 - 2C_3 - 2D_3 + F_3)\psi(i,j) + (-B_3 + D_3)\psi(i,j-1) \\ & +(-A_3 + C_3 - E_3)\psi(i-1,j)\end{aligned} \tag{8.9}$$

b) *i*- backward, *j*- central

$$\begin{aligned}\tau_{r\theta} = {} & (A_3 + C_3 + E_3)\psi(i+1,j) + (B_3 + D_3)\psi(i,j+1) + (-3A_3 - 2B_3 - 2C_3 - 2D_3 + F_3)\psi(i,j) \\ & +(B_3 + D_3)\psi(i,j-1) - B_3\psi(i-1,j+1) + (3A_3 + 2B_3 + C_3 - E_3)\psi(i-1,j) \\ & - B_3\psi(i-1,j-1) - A_3\psi(i-2,j)\end{aligned} \tag{8.10}$$

where,

$$A_3 = \frac{G}{h^3},\ B_3 = \frac{-\nu G}{r_i^2 h k^2},\ C_3 = -\frac{4G}{r_i h^2},\ D_3 = \frac{(1+2\nu)G}{r_i^3 k^2},\ E_3 = \frac{9G}{2r_i^2 h},\ F_3 = -\frac{9G}{r_i^3}$$

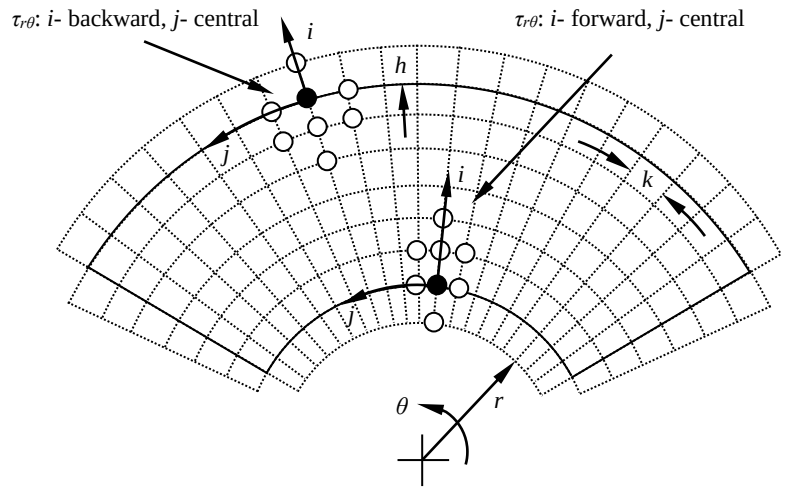


**Figure 8.3:** The smallest finite difference stencil for shear component ($\tau_{r\theta}$) of stress (Formulation-I)

## 8.3 EXAMPLE OF APPLICATION OF SMALLER FDM STENCILS

This section describes the effect of stencil size on the present $\psi$-formulation solution for a curved beam. To demonstrate the effect the curved beam considered is a both-ends-fixed beam. Both-ends-fixed beam considered here is the same beam considered in the chapter 05. Geometrical properties, material properties and mesh network used to solve the problem are similar to the both-ends-fixed beam problem solved in chapter 05. Solutions for tangential displacement and tangential stress along radial sections are considered to demonstrate the effect. FEM solution is also presented along with these two solutions to understand which solution is superiority than the other.

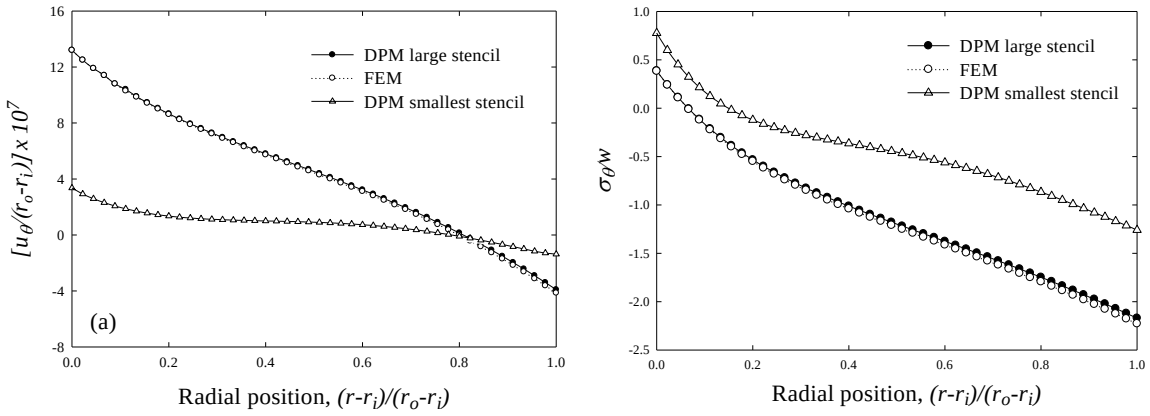


**Figure 8.4:** Comparison of solutions obtained by large stencil DPM and small stencil DPM along with the FEM solution for (a) tangential displacement along radial section at an angular position of 45$^o$; (b) tangential stress along radial section at an angular position of 40$^o$ for the both-ends-fixed beam.

Figure 8.4(a) shows the effect of stencil size on the distribution of tangential displacement along radial position for $\theta = 45^o$ radial section. From the distribution the tangential displacement obtained using large stencil DPM and FEM solution are found to match each other very well where as small stencil DPM solution is found to differ significantly. Same observation can be found from figure 8.4(b) which shows the distribution of tangential stress along radial location for $\theta = 40^o$ radial section. In both cases the solutions obtained by large stencil DPM and FEM shows very good agreement and differ significantly with the smallest stencil DPM solution. This certainly proves that the large stencil DPM produces more reliable solution than the small stencil DPM.

## 8.4 CONCLUSIONS

A curved beam problem is solved using two different sets of stencils. One set of stencil considered here is the smallest possible stencil and the other one is a bigger version of stencil. A significant effect of stencil size is observed from the results. Quality of solution decreases significantly with smaller version of stencils as seen from the comparison with the FEM solution. As a result the bigger version of stencils used in this study is preferred compared to the smaller version of stencils.

Chapter 09

# CONCLUSIONS AND RECOMMENDATIONS

## 9.1 CONCLUSIONS

A new elasticity formulation based on a displacement potential has been developed for the analysis of elastic field of curved structural elements. Based on the mathematical model a new finite-difference computation scheme has been developed for solving problems of curved structural elements with all possible modes of boundary conditions whether they are prescribe in terms of either loadings or constraints or any combination of them. The present computational method provides a simple but efficient approach of analysis as it reduces the two dimensional structural problems in polar coordinate system to finding a single potential function satisfying a single differential equation of equilibrium. Finally, the following conclusions are drawn in relation to the present research work:

1. A new elasticity formulation for the analysis of stresses and displacements in two-dimensional isotropic solids in polar coordinate system is presented in this thesis. The present formulation reduces the problem to finding a single variable from a single governing differential equation and boundary conditions where the boundary conditions can be given in terms of either loadings or restraints or any combination of them. The present formulation can handle mixed-boundary-value problems of elasticity very efficiently.
2. The development of the present displacement potential field formulation eventually leads to two different versions of the formulation, which are denoted by Formulation-I and Formulation-II. The original two variable ($u_r$ and $u_\theta$) equilibrium problem has been reduced to a single variable (potential function $\psi$) problem through the application of a variable reduction scheme, the process of which however gives rise to an option to choose one of the equilibrium equations for necessary treatments. It has been observed that both the second order elliptic partial differential equations of equilibrium are transformed to the same fourth order partial differential equation of

equilibrium when expressed in terms potential function $\psi$. As a result, the two formulations, namely Formulation-I and Formulation-II are based on the same governing differential equation of equilibrium, although the potential function itself is defined in two different ways in case of the two formulations. Finally, the expressions of relevant displacement and stress components of the two formulations become different in terms of both the derivatives and coefficients when expressed in terms of the potential function.

3. A finite-difference computational scheme based on the mathematical formulation is developed in this thesis. A number of boundary-value problems of structural mechanics have been solved and the results, in each case, are verified to be quite reasonable. Moreover, the soundness and suitability of this numerical approach has been established by the study of the graphical results of different problems for the important parameters namely the relevant stress and displacement components.
4. Results obtained from the present computational approach are compared with the available analytical and numerical results for a number of problems. All the comparison shows excellent agreement of the present $\psi$-formulation with the other available analytical and numerical approaches. This validates the mathematical formulation as well as numerical modeling of the present displacement potential method in polar coordinate system.
5. The present displacement potential approach ($\psi$-formulation) differs from the stress function approach ($\phi$-formulation) in the sense that the problem can be formulated in terms of $\psi$ satisfying all modes of boundary conditions exactly. Whereas, the boundary conditions specified as restraints were satisfied approximately in an overall nature by the $\phi$-formulation and the solutions thus obtained were not satisfactory in predicting stresses in the regions of supports, stiffeners as well as guided boundaries. However, using this present $\psi$-formulation, the numerical solutions obtained for mixed-boundary-value problems are valid for the entire region of interest, and provide far better understanding of stress distribution in the critical regions of the boundaries.
6. As far as time for numerical computation is concerned, earlier, two-dimensional mixed-boundary-value stress problems were solved in terms of two variables namely, two displacement components $u_r$ and $u_\theta$, but the time required for the evaluation of two functions simultaneously, satisfying two simultaneous partial differential equations and the mixed boundary conditions, is extremely large and is very much dependent on the nature of the problems. However, the $\psi$-formulation does not suffer

from these shortcomings as in this approach, a single function $\psi$ has to be evaluated satisfying a forth order elliptic partial differential equation and the prescribed boundary conditions and it is also observed that the computational time is almost independent of the nature of problems.

7. Among various numerical approaches, finite difference and finite element methods are the most attractive methods in solving the boundary-value stress problems. In the finite element approach, shape functions are assumed in terms of polynomials to predict the deformation patterns. Thus, the structure is constrained to deflect in the assumed mode, rather than the one it would adopt naturally. Moreover, the constraints give rise to artificial stiffening and increased stored energy in the structure. Therefore, the method is likely to give poor results if the assumed shape function does not satisfy the actual deformation pattern exactly. But the finite difference technique is straight forward in its application and thereby producing more attractive results as they are free from the shortcomings mentioned above.
8. The computer program developed here is completely general and it can handle all modes of mixed as well as changeable boundary conditions. As far as the computer program is concerned, the finite difference method has established its suitability and appropriateness in finding solutions for two-dimensional stress problems through its application in the field of partial differential equations.
9. Both the qualitative and quantitative results and moreover, the comparison with the available analytical and numerical solutions conform the soundness as well as the appropriateness of the computational approach in the field of boundary-value stress problems of curved bodies. It is thus expected that, with time, solutions would be obtained for various practical problems in order to provide better insight and further understanding of the stress distribution in the critical regions of supports, stiffeners and guides of curved structural problems. There is no doubt that the present displacement potential would be a powerful tool in the field of structural mechanics.

## 9.2 FUTURE RECOMMENDATIONS

The new displacement potential method (DPM) has been developed to provide a new avenue for the investigations of elastic curved structures with various mixed boundary conditions of interest. In this connection, it is recommended that the following extensions may be carried out for further developments:

1. The present mathematical formulation in it present form is only applicable for isotropic materials. Formulations based on displacement potential in polar coordinate system for orthotropic and anisotropic materials can be developed in the same way as showed in the present thesis.
2. The present computer program is based on the plane stress assumption and can be extended for plane strain problems in polar coordinate system. The displacement potential formulation in polar coordinate system may also be extended for the analysis of three-dimensional stress problems in cylindrical coordinate system.
3. The computer program developed can handle regular geometric shapes of curved bodies. Numerical modeling for irregular geometric shapes in polar coordinate system may be investigated and thus can be incorporated in the computer program.
4. Attention may be given to incorporate a better treatment for the various forms of singularities in the boundary conditions. The most appropriate method of treating these singularity would be to assume some series of $\psi$ satisfying the local conditions, and then to use these series in truncated form for the evaluation of the functions at these points instead of finite difference expressions.

# BIBLIOGRAPHY


1. Horgan CO, Knowels JK. Recent developments concerning Saint Venant_s principle. *Advances in Applied Mechanics* 1983; **23**:179–269.
2. Durelli AJ, Ranganayakamma B. On the use of photoelasticity and some numerical methods. *Photomechanics and Speckle Metrology SPIE* 1987; **814**:1–8.
3. Durelli AJ, Ranganayakamma B. Parametric solution of stresses in beams. *Journal of Engineering Mechanics* 1989; **115** (2): 401–415.
4. Dow JO, Jones MS, Harwood SA. A new approach to boundary modeling for finite difference applications in solid mechanics. *International Journal for Numerical Methods in Engineering* 1990; **30**:99–113.
5. Timoshenko D, Goodier JN. *Theory of elasticity* (3rd edn). McGraw-Hill Book Company: New York, NY, 1979.
6. Conway HD, Chow L, Morgan GW. Analysis of deep beams. *J Appl Mech Trans ASME* 1951; **18**(2):163–72.
7. Chow L, Conway HD, Winter G. Stresses in deep beams. *Trans ASCE* 1952; Paper No. 2557.
8. Chapel RE, Smith HW. Finite-difference solutions for plane stresses. *AIAA J* 1968; **6**(6):1156–7.
9. Ahmed SR, Idris ABM, Uddin MW. Numerical solution of both ends fixed deep beams. *Computers and Structures* 1996; **61**(1): 21–9.
10. Ahmed SR, Khan MR, Islam KMS, Uddin MW. Investigation of stresses at the fixed end of deep cantilever beams. *Computers and Structures* 1998; **69**:329–38.
11. Saada AS. *Elasticity- Theoryand Applications*. Pergamon Press Inc.: New York, NY, 1974.
12. Shigley JE, Mitchell LD. *Mechanical engineering design* (4th edn). McGraw-Hill Book Company: New York, NY, 1983.
13. Shigley JE, Mischke CR. *Mechanical engineering design* (5th edn). McGraw-Hill Book Company: New York, NY, 1989.
14. Ugural AC, Frenster SK. *Advanced strength and applied elasticity* (2nd edn). Elsevier Publishing Company: North Holland, 1989.

15. Oden JT, Ripperger EA. *Mechanics of elastic structures* (2nd edn). McGraw-Hill Book Company: New York, 1981.
16. Cook RD. Circumferential stress in curved beams. *Trans. ASME, Journal of Applied Mechanics* 1992; **59**:224-225.
17. Brock JE. Stresses in curved beams. *Machine design* 1971; **Mar. 4**:88-90.
18. Perkins HC. Stresses in curved bars. *Trans ASME* 1931; **53**:201-205.
19. Wahl AM. Calculation of stress in crane hooks. *Trans ASME* 1946; **68**:239-242.
20. Winslow AM, Edmonds RHG. Tests and theory of curved beams. *Trans ASME* 1926; **48**:647-663.
21. Wright W. Stresses in curved beams- a tabular method of solution based on Winkler's Theory. *Trans ASME, Journal of Applied Mechanics* 1953; **68**:138-139.
22. Chianese RB and Erdlac RJ. The general solution to the distribution of stresses in a circular ring compressed by two forces acting along a diameter. *Quarterly Journal of Mechanics and Applied Mathematics*1998; **41**(2):239-247.
23. Bagci C. A new strength of materials solution for stresses in curved beams and rings. *Journal of Mechanical Design* 1992; **114**:231-237.
24. Bagci C. Exact elasticity solutions for stresses and deflections in curved beams and rings of exponential and T-sections. *ASME Journal of Mechanical Design* 1993; **115**:346-358.
25. Tutuncu N. Plane stress analysis of end loaded orthotropic curved beams of constant thickness with applications to full rings. *ASME Journal of Mechanical Design* 1998; **120**:368-374.
26. Sloboda A, Honarmandi P. Generalized elasticity method for curved beam stress analysis: analytical and numerical comparison for a lifting hook. *Mechanics Based Design of Structures and Machines* 2007; **35**:319-332.
27. Makowski Z S, Gogate M N. Stress analysis of three-pinned arch-ribbed domes. *ICE Proceedings: Engineering Divisions* 1956. **5**(6);824 –844.
28. Hiroyuki Matsunaga. Interlaminar stress analysis of laminated composite and sandwich circular arches subjected to thermal/mechanical loading. *Composite Structures* 2003; **60**(3):345–358
29. Elmalich, D. and Rabinovitch, O. Stress Analysis of Monolithic Circular Arches Strengthened with Composite Materials. *Journal of Composites for Construction, ASCE* 2009; **13**(5):431–441.

30. Hiroyuki Matsunaga. Free vibration and stability of laminated composite circular arches subjected to initial axial stress. *Journal of Sound and Vibration* (2004); **271**(3-5):651–670.
31. Leon Beskin. General Circular Ring Analysis. *Aircraft Engineering and Technology* 1945, **17**(5):126-132.
32. O.L. Bowie, C.E. Freese. *Elastic analysis for a radial crack in a circular ring. Engineering Fracture Mechanics* 1972; **4**(2):315–321.
33. A. J. Durelli, V. J. Parks, T. L. Chen. Stress and finite-strain analysis of a circular ring under diametral compression. *Experimental Mechanics* 1969; **9**(5):210-214.
34. Xiao Zeng Wang. Theoretical and Numerical Solution of Deflection of the Circular Ring under a Concentrated Force. *Advanced Materials Research* 2013; **690-693**:1919-1922.
35. Cook RD. Axisymmetric finite element analysis for pure moment loading of curved beams and pipe bends. *Computers and structures* 1989; **33**(2):483-487.
36. Rattanawangcharoen N, Bai H and Shah AH. A 3D cylindrical finite element model for thick curved beam stress analysis. *International journal for numerical methods in engineering* 2004, **59**:511–531.
37. Richards TH, Daniels MJ. Enhancing finite element surface stress predictions: a semi-analytic technique for axisymmetric solids. *Journal of Strain Analysis* 1987; **22**(2):75–86.
38. Smart J. On the determination of boundary stresses in finite elements. *Journal of Strain Analysis 1987*; **22**(2):87–96.
39. Prathap Gangan. The curved beam/deep arch/finite ring element revisited. *International Journal for Numerical Methods in Engineering* 1985; **21**:389–407.
40. Ranzi G, Gara F, Leoni G, Bradford MA. Analysis of composite beams with partial shear interaction using available modeling techniques: A comparative study. *Computers & Structures* 2006; **84**:930–941.
41. Ahmed SR, Deb Nath SK, Uddin MW. Optimum shapes of tire-threads for avoiding lateral slippage between tires and roads. *International Journal for Numerical Methods in Engineering* 2005; **64**:729–750.
42. Ahmed SR, Hossain MZ, Uddin MW. A general mathematical formulation for finite-difference solution of mixed-boundary-value problems of anisotropic materials. *Computers and Structures* 2005; **83**:35-51.

43. Hossain MZ, Ahmed SR, Uddin MW. Generalized mathematical model for the solution of mixed-boundary-value elastic problems. Applied Mathematics and Computation 2005; **169**:1247-1275.
44. Deb Nath SK, Ahmed SR. A displacement potential-based numerical solution for orthotropic composite panels under end moment and shear loading. *J. Mechanics of Materials & Structures* 2009; **4**(6):987–1004.
45. Wei Xu, Guoqiang Li. Finite difference three-dimensional solution of stresses in adhesively bonded composite tubular joint subjected to torsion. *International Journal of Adhesion & Adhesives* 2010; **30**:191–199.
46. Akanda MAS, Ahmed SR, Uddin MW. Stress analysis of gear teeth using displacement potential function and finite differences. International Journal for Numerical Methods in Engineering 2002; **53**:1629–40.
47. Akanda MAS, Ahmed SR, Khan MR, Uddin MW. A finite-difference scheme for mixed boundary-value problems of arbitrary-shaped elastic bodies. *Advances in Engineering Software* 2000; **31**(3):173–84.
48. Ahmed SR. Numerical solution of mixed boundary-value elastic problems. Master's thesis, Bangladesh University of Engineering and Tehnology, Bangladesh, 1993.

# APPENDICES

# APPENDIX
# A

## ANSYS model of the both-ends-fixed curved beam


**Figure A.1:** Geometry of the curved beam.

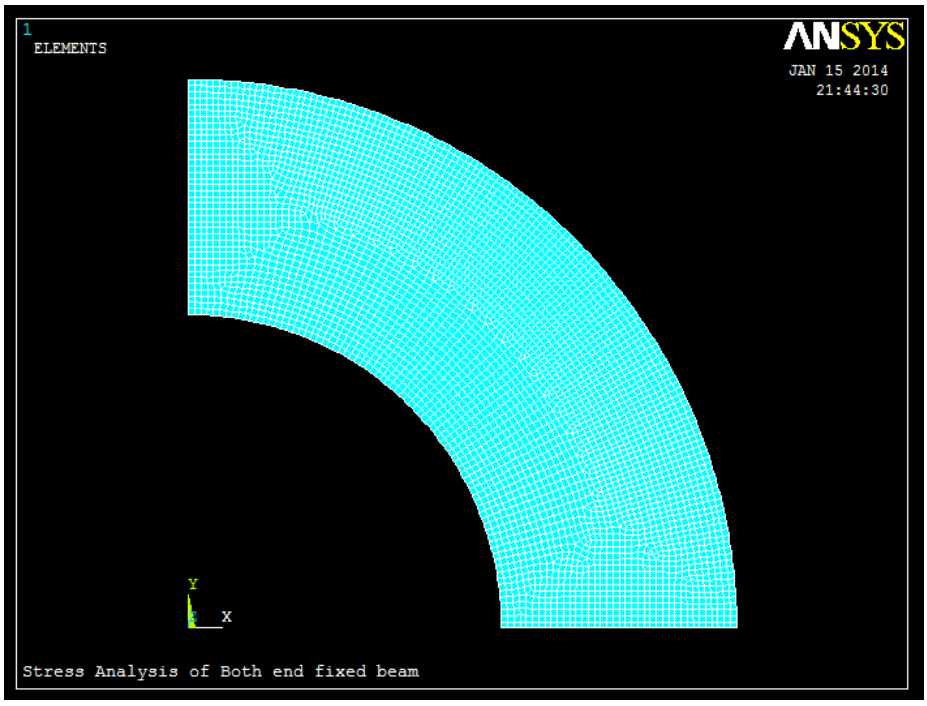


**Figure A.2:** Meshed geometry of the curved beam.

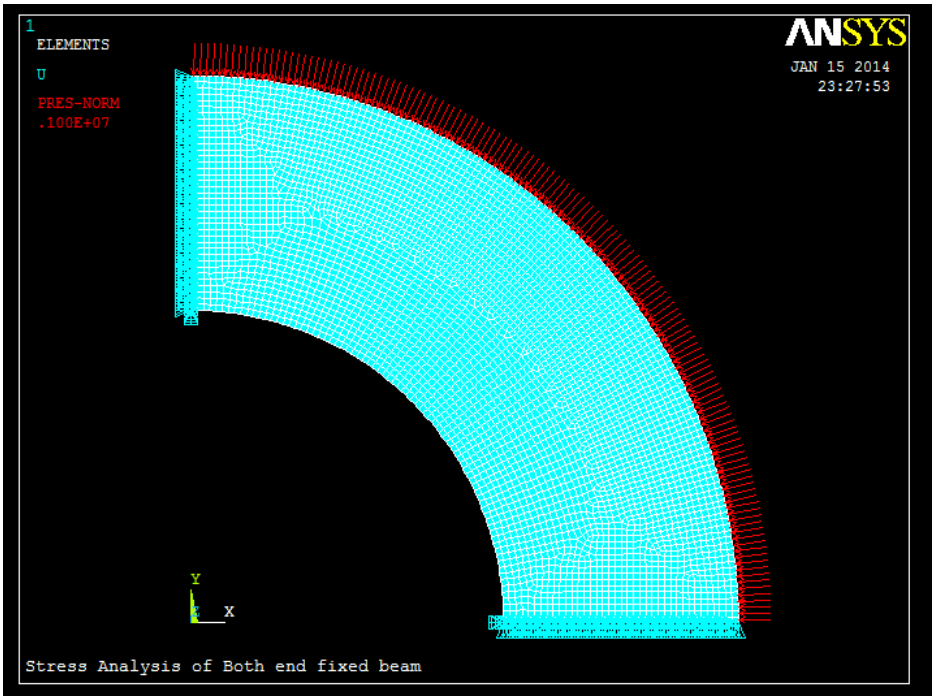


**Figure A.3:** ANSYS model of the both-ends-fixed curved beam under radial pressure at the convex surface of the beam.

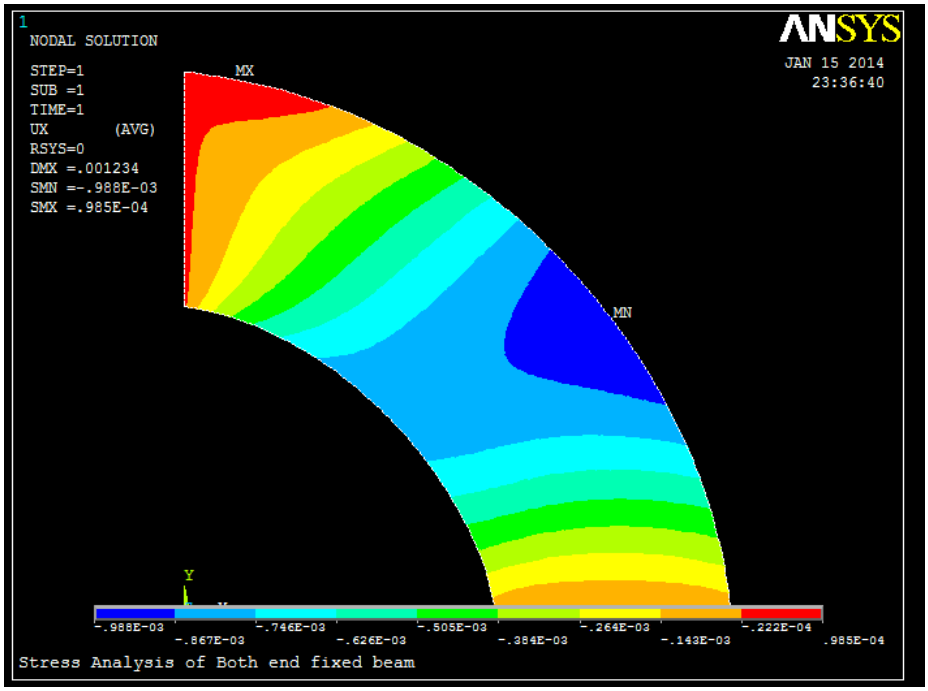


**Figure A.4:** Contour plot for the nodal solution of $u_x$.

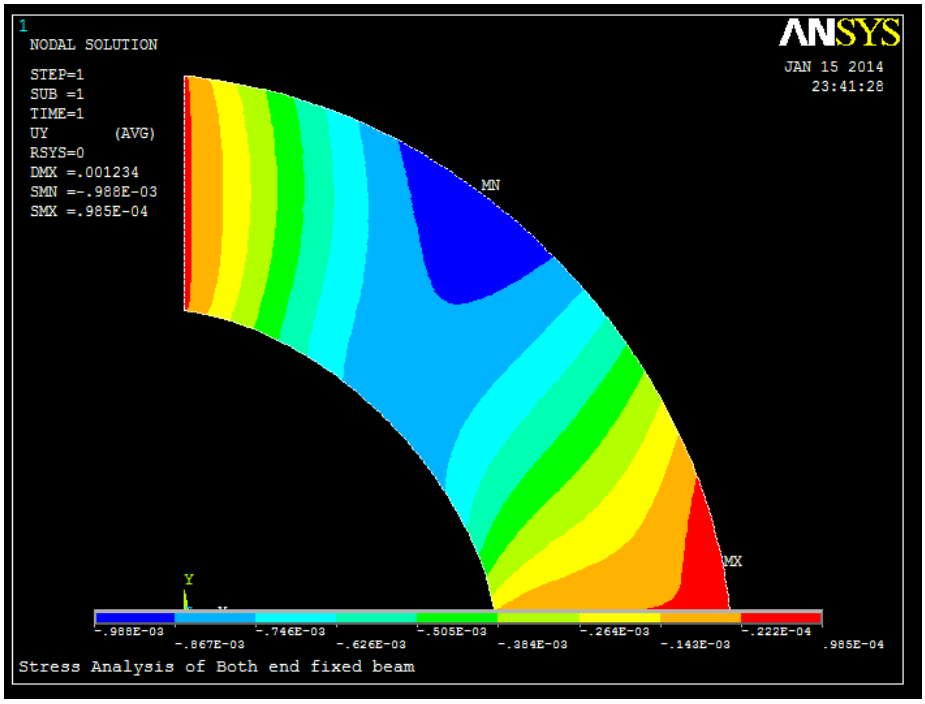


**Figure A.5:** Contour plot for the nodal solution of $u_y$.

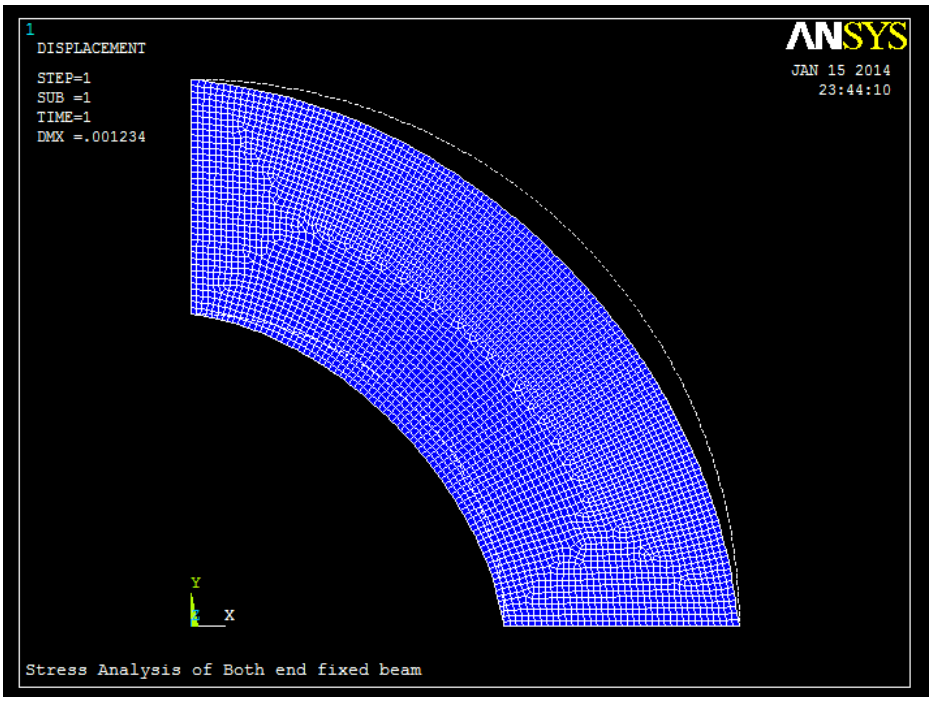


**Figure A.6:** Deformed shape of the both-ends-fixed curved beam with undeformed edges.

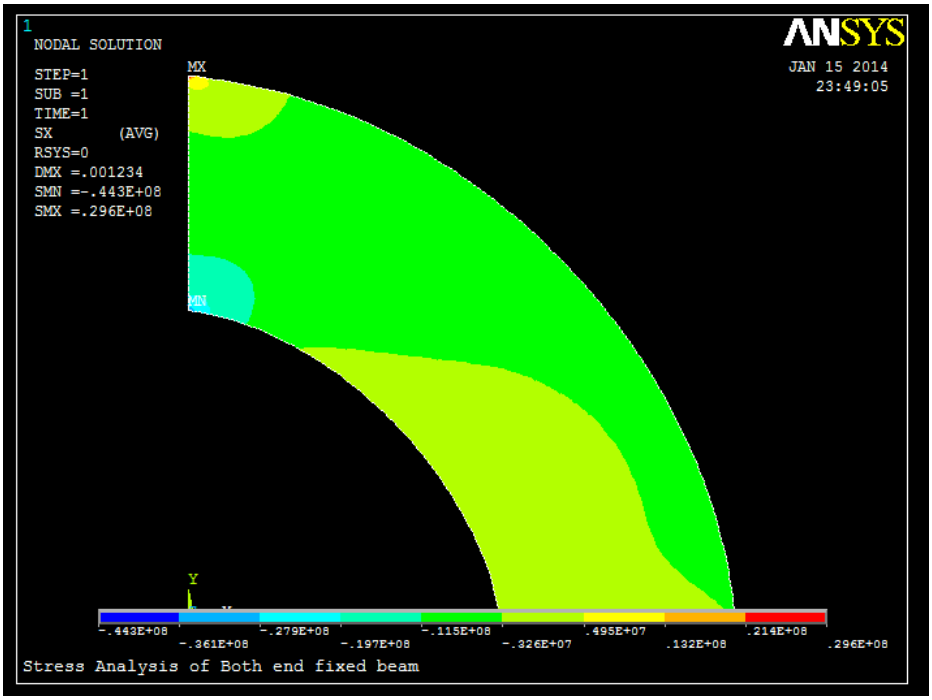


**Figure A.7:** Contour plot for the nodal solution of $\sigma_x$.

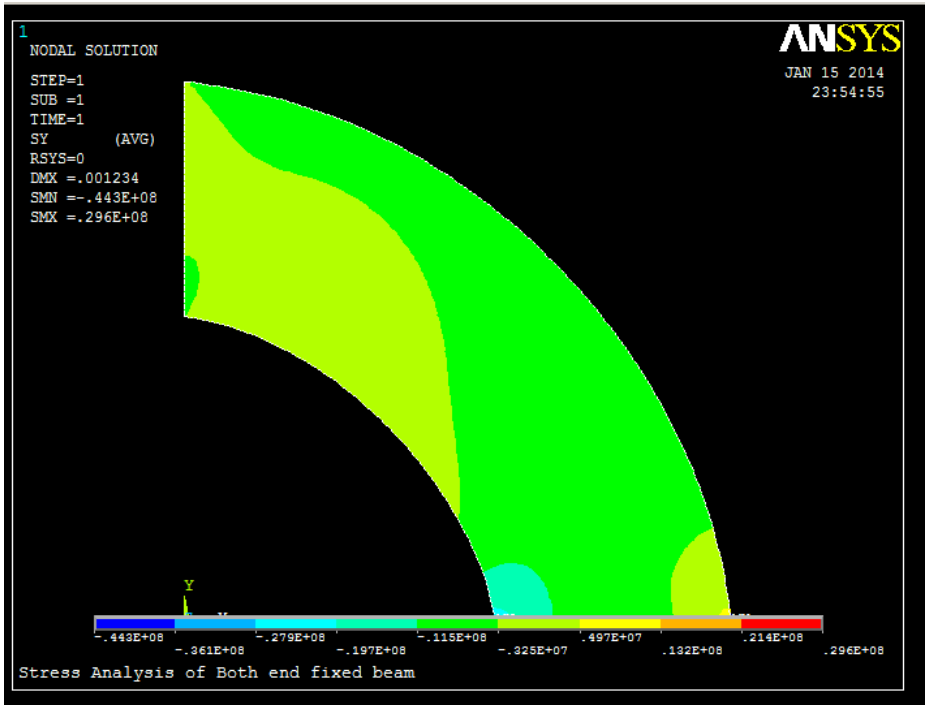


**Figure A.8:** Contour plot for the nodal solution of $\sigma_y$.

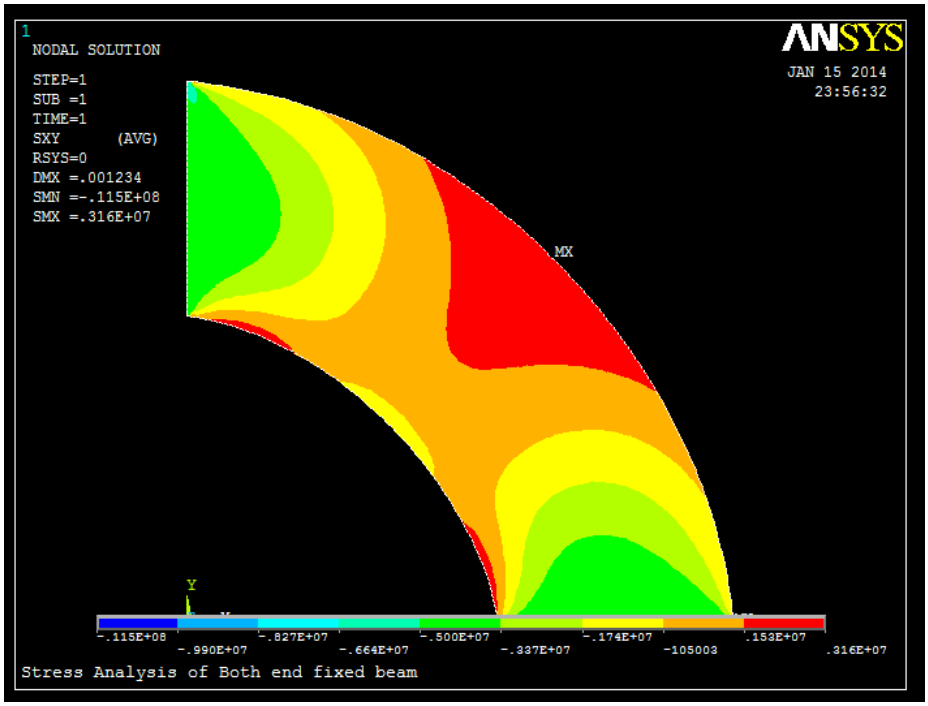


**Figure A.9:** Contour plot for the nodal solution of $\tau_{xy}$.

# APPENDIX
# B

## MATLAB code for the conversion of ANSYS solution of both-ends-fixed beam from Cartesian form to polar form

**B.1.** MATLAB code for the conversion stress and displacement components obtained from ANSYS solution along any radial layer of the curved beam.

```
%%%Program for Cartesian to Polar conversion

close all; clear all; clc;
format long;

%Extraction of material constants from input file
P=xlsread('G:\Study\Academic- postgraduate\Thesis\Cartesian-Polar-
Conversion\convt','A2:E60');
Q=xlsread('G:\Study\Academic- postgraduate\Thesis\Cartesian-Polar-
Conversion\convt','L2:L4');

Ux=P(:,1);
Uy=P(:,2);
Sx=P(:,3);
Sy=P(:,4);
Sxy=P(:,5);

r1=Q(1,1);
r2=Q(2,1);
t=Q(3,1);

n=size(Ux,1);

Ur=zeros(n);
Ut=zeros(n);
Sr=zeros(n);
St=zeros(n);
Srt=zeros(n);

% Conversion Formulas

for i=1:n
    Ur(i)=Ux(i)*cosd(t)+Uy(i)*sind(t);
    Ut(i)=-Ux(i)*sind(t)+Uy(i)*cosd(t);
    Sr(i)=Sx(i)*(cosd(t))^2+Sy(i)*(sind(t))^2+2*Sxy(i)*sind(t)*cosd(t);
    St(i)=Sx(i)*(sind(t))^2+Sy(i)*(cosd(t))^2-2*Sxy(i)*sind(t)*cosd(t);
    Srt(i)=(Sy(i)-Sx(i))*sind(t)*cosd(t)+Sxy(i)*((cosd(t))^2-(sind(t))^2);
end
```

**B.2.** MATLAB code for the conversion stress and displacement components obtained from ANSYS solution along any circumferential layer of the curved beam.

```
%%%Program for Cartesian to Polar conversion

close all; clear all; clc;
format long;

%Extraction of material constants from input file
P=xlsread('G:\Study\Academic- postgraduate\Thesis\Cartesian-Polar-
Conversion\convt','A2:E60');
Q=xlsread('G:\Study\Academic- postgraduate\Thesis\Cartesian-Polar-
Conversion\convt','L2:L5');

Ux=P(:,1);
Uy=P(:,2);
Sx=P(:,3);
Sy=P(:,4);
Sxy=P(:,5);

r1=Q(1,1);
r2=Q(2,1);
t1=Q(3,1);
t2=Q(4,1);

n=size(Ux,1);
k=(t2-t1)/(n-1);

Ur=zeros(n);
Ut=zeros(n);
Sr=zeros(n);
St=zeros(n);
Srt=zeros(n);

% Conversion Formulas
t=t1;

for i=1:n

    Ur(i)=Ux(i)*cosd(t)+Uy(i)*sind(t);
    Ut(i)=-Ux(i)*sind(t)+Uy(i)*cosd(t);
    Sr(i)=Sx(i)*(cosd(t))^2+Sy(i)*(sind(t))^2+2*Sxy(i)*sind(t)*cosd(t);
    St(i)=Sx(i)*(sind(t))^2+Sy(i)*(cosd(t))^2-2*Sxy(i)*sind(t)*cosd(t);
    Srt(i)=(Sy(i)-Sx(i))*sind(t)*cosd(t)+Sxy(i)*((cosd(t))^2-(sind(t))^2);

    t=t+k;
end
```